

ABSTRACT

JOYNER, CATELYN NICHOLE. Lacustrine Megaturbidites and Displacement Waves: The Holocene Earthquake History of the Lake Creek-Boundary Creek Fault at Lake Crescent, Washington, USA. (Under the direction of Dr. Karl Wegmann and Dr. Elana Leithold).

Lake Crescent is a deep, glacially carved lake located on the northern Olympic Peninsula within Olympic National Park. Its location in the forearc of the Cascadia subduction zone and proximity to seismically-active regional crustal faults allow for its high resolution sedimentary record to function as an extension of the local paleoseismic record. This study uses airborne lidar topography, multibeam bathymetry, seismic reflection profiles, and sediment cores to characterize four megaturbidites attributed to Holocene ruptures along the Lake Creek-Boundary Creek fault. The megaturbidites each consist of an erosively based normally graded basaltic sand layer overlain in turn by massive, homogenous silt with plant debris, a clay cap, and interstratified chloritic clay and basaltic sand laminae. The deposits can be traced across the deep basins of the 20 km² lake and exceed 1.3 m in thickness in cores recovered from the deepest part of the lake. The youngest megaturbidite is estimated to have a minimum volume of $\sim 4.8 \times 10^6 \text{ m}^3$. Petrologic analysis of megaturbidite basal sands indicates that they are sourced from the entire lake margin and likely were remobilized from shallow subaqueous environments.

Newly acquired bathymetric data reveal that several large rockslides that surround Lake Crescent deposited debris into the lake. Previous research indicates that subaerial rockslides entering lakes can generate displacement (tsunami) waves and seiches that result in megaturbidite deposits. Radiocarbon analysis of the megaturbidites indicate that four

rockslide-displacement waves occurred at 2,859 (2,785-2,943), 4,015 (3,921-4,088), 5,736 (5,656-5,889), and 7,097 (7,006-7,242) cal yr BP. The most recent event deposited $\sim 7 \times 10^6$ m³ of debris into the lake, which likely generated a displacement wave with an opposite-shore run up height of 86 ± 20 m. Offset of the megaturbidite layers visible in seismic reflection profiles where the Lake Creek-Boundary Creek fault traverses the northern lake basin shows that rupture along the fault and the deposition of megaturbidites are related. The mean inter-event recurrence interval for the four Lake Crescent megaturbidites is 1412 ± 234 years with the mean age of the most recent event 2,859 cal yr BP. As a result, based upon a lognormal probability distribution there is a 28% chance that an earthquake will occur along the Lake Crescent portion of the Lake Creek-Boundary Creek fault zone in the next 50 years. This result highlights the regional seismic hazard to the north Olympic Peninsula posed by this fault.

© Copyright 2016 by Catelyn Nichole Joyner

All Rights Reserved

Lacustrine Megaturbidites and Displacement Waves: The Holocene Earthquake History of
the Lake Creek-Boundary Creek Fault at Lake Crescent, Washington, USA

by
Catelyn Nichole Joyner

A thesis submitted to the Graduate Faculty of
North Carolina State University
in partial fulfillment of the
requirements for the degree of
Master of Science

Marine, Earth, and Atmospheric Sciences

Raleigh, North Carolina

2016

APPROVED BY:

Dr. Karl Wegmann
Co-Chair of Advisory Committee

Dr. Elana Leithold
Co-Chair of Advisory Committee

Dr. DelWayne Bohnenstiehl

DEDICATION

For Mom and Dad- You always told me I could achieve my dreams. Thank you for the eternal support that allowed me to chase them. Dad, I hope this gets me a job. Mom, thanks for being my best friend through it all. For Vanessa- I am ever grateful for the patience and support you have provided over the years. You never once complained all the time I talked about rocks. This wouldn't have been possible without you. For Granny- I miss you and I hope you are proud of me. For Alex (Alchy) and Wesley (Bubs)- Alchy, you are my rock. For Aunt Rhonda, Uncle Tom, and Jordan- Aunt Rhonda, you always have had my back and encouraged my rock collecting at a young age. You are such a bright part of my life; much like your favorite mineral, mica. I would not have made it without football chili Sundays and complaining about the Washington Redskins with you Uncle Tom. For Nanny and Papa- You are the best grandparents anyone could ask for. The great talks and even better food (thanks Nanny) I enjoyed while visiting home were a much appreciated break from school. For Aunt Linda, Uncle Eddie, and Slim- Aunt Linda, no matter the situation, you always make me laugh- something that I truly valued on the hard days. Uncle Eddie and Slim, our fishing days on the river provided much relief from school and I will always remember them. Also, thank you to my dogs Portia and Ellen for your endless love and attention on the good and bad days. Thank you to everyone who stepped up and helped Mom when she was sick when I couldn't while I was in Raleigh working on this thesis. I love you all!

BIOGRAPHY

I was born on November 6, 1991, to Chip and Janine Joyner of Suffolk, Virginia. During high school, I pursued an Associate degree in science where I was the youngest student to attend Paul D. Camp Community College at age 15. It was during this time that I discovered my love for math and science related courses which landed me at North Carolina State University in 2010 as a freshman with a degree already in hand. Initially, I had an incredibly hard time figuring out what major I wanted to pursue but my love of math, science, and the outdoors pushed me into the world of geology.

In 2011, I became the research assistant in the geology labs at the North Carolina State Museum of Natural Science. This opportunity provided research and professional development opportunities that allowed me to excel as a student leading to my graduation in 2013. My amazing experience as an undergraduate in the Marine, Earth, and Atmospheric Science Department as well as undying love for the Wolfpack brought me back to NCSU for my graduate studies in 2014.

ACKNOWLEDGMENTS

First and foremost, thank you to all of my committee members. Dr. Karl Wegmann, thank you for the support and encouragement as well as letting me work on such an exciting project. Dr. Elana Leithold, thank you for infectious enthusiasm about sedimentology and inspiring me to want to work with sediments when I was an undergraduate. Dr. DelWayne Bohnenstiehl, thank you for your patience and support while I learned about data analysis and the complex language of Matlab. Thank you all for trusting me to work with you. My relationships with you all have encouraged me become a better student, collaborator, and geologist.

Thank you to the Earth Surface Processes Research Group: Rachel Atkins, Gantulga Bayasgalan, Adam Lee, Audrianna Pollen, John Wall, Steve Smith, and Julian (Nuttman) Chesnutt for their academic feedback and great friendship. Thank you to undergraduates Austin Jacobs, Nicholas Lavoie, and Hallie Nunamaker for their diligence and help with the Lake Crescent sand petrology project. Thank you to Nicholas Lavoie, Bryce Finch, and Alex Ruley for their help with the particle size analysis. Thanks also go to Dr. Ronald Fodor for helping me understand the world of petrology again after a 5-year hiatus.

A very special thank you goes to Dr. Christopher Tacker, who took a chance and hired me while I was an undergraduate. Thank you for letting me work in your lab for my thesis research- what a great mentor and friend you have been.

Thank you so much to the team from LacCore- Kristina Brady, Anders Noren, Mark Shapley, and Ryan O’Grady. Learning from you all in the field and lab was an amazing experience!

Last but not least, thank you to all other friends in the MEAS Department for all the good times and memories!

This research was made possible by a U.S. Geological Survey – National Earthquake Hazards Reduction Program Grant (Award #G15AP00091). Research within Olympic National Park was conducted under Special Use Permit #OLYM-366.

TABLE OF CONTENTS

LIST OF TABLES	ix
LIST OF FIGURES	x
LIST OF APPENDICES	xi
1.0 INTRODUCTION	1
1.1 Geologic Setting.....	4
1.2 Tectonic Setting and Earthquake History	5
1.3 Lake Crescent Catchment	10
2.0 METHODS	12
2.1 Seismic Reflection Survey	12
2.2 Sediment Coring	12
2.3 Multibeam Bathymetric Survey	13
2.4 Core Sampling	13
2.5 Radiocarbon Dating	14
2.6 Fourier Transform Infrared Spectroscopy	16
2.7 Sediment Analysis	17
2.7.1 Particle Size Analysis	17
2.7.2 Boundary Shear Stresses.....	17
2.7.3 Sand Petrology	18
2.8 ArcGIS Modeling.....	19
2.9 Displacement Wave Heights.....	22

3.0 RESULTS	25
3.1 Seismic Stratigraphy	25
3.1.1 North Basin Stratigraphy	26
3.1.2 South Basin Stratigraphy	26
3.1.3 Subaqueous Rockslide Deposits	27
3.2 Sedimentology	27
3.3 Geochronology and Stratigraphy	29
3.4 Sand Petrology	31
3.4.1 Stream Sand	32
3.4.2 Event Layer 1 Sand	33
3.4.3 Event Layer 2 Sand	33
3.5 Event Layer 1-A Sediment Transport Dynamics	33
3.6 Event Layer 1-A Distribution and Volume	34
3.7 Sledgehammer Point Rockslide	35
3.8 Displacement Wave Heights	35
4.0 DISCUSSION	36
4.1 Megaturbidites	36
4.2 Lake Crescent Megaturbidites	41
4.3 Earthquake Origins	50
4.4 Seismic Hazards	53

5.0 SUMMARY AND CONCLUSIONS	56
6.0 FUTURE WORK	57
REFERENCES	135
APPENDIX	145

LIST OF TABLES

Table 1. Lake Crescent core data	58
Table 2. Closed depression charcoal sample data	59
Table 3. Parameters for the boundary shear stress calculations	60
Table 4. Original and recalculated parameters for the petrologic study	61
Table 5. Dependent parameters of the displacement wave height equation	62
Table 6. Independent parameters of the displacement wave height equation	63
Table 7. FTIR results of green clay	64
Table 8. Radiocarbon age results	65
Table 9. Petrologic sand count results of original parameters	66
Table 10. Petrologic sand count results of recalculated parameters	68
Table 11. Boundary shear stress results	69
Table 12. Megaturbidite EL1-A volume results.....	70
Table 13. Displacement wave height results	71
Table 14. Historical landslide and displacement wave data.....	72

LIST OF FIGURES

Figure 1. Location of Lake Crescent with surrounding features.....	73
Figure 2. Simplified geologic map of the Olympic Peninsula.....	74
Figure 3. Rockslides and faults within the Lake Crescent region.....	75
Figure 4. Lidar imagery of the Sadie Creek fault scarp.....	78
Figure 5. Photograph of the Lake Sutherland rockslide complex and Mt. Storm King rockslide.....	79
Figure 6. Main tributaries of Lake Crescent.....	80
Figure 7. Simplified geologic map of the Lake Crescent region.....	81
Figure 8. Chirp seismic survey lines and Kullenburg core locations.....	84
Figure 9. Cross section and top view of displacement wave height parameters.....	85
Figure 10. Seismic line from the central north basin displaying stratigraphy and deformation related to the Lake Creek-Boundary Creek fault.....	86
Figure 11. Seismic line from the central north basin displaying stratigraphy and deformation related to the Lake Creek- Boundary Creek and Sadie Creek faults.....	88
Figure 12. Seismic line from the central south basin displaying stratigraphy and no fault-related deformation.....	90
Figure 13. Seismic line from the western portion of the south basin displaying stratigraphy and no fault-related deformation.....	92
Figure 14. Seismic line from the central channel between the north and south basin displaying subaqueous rockslide deposits with intra-deposit depressions.....	94
Figure 15. Seismic line from the eastern portion of the north basin displaying subaqueous rockslide deposits with no intra-deposit depressions.....	96
Figure 16. Down-core median particle size and normalized magnetic susceptibility profiles of the most recent EL1 layer in cores 2C-1K and 8A-1K.....	98
Figure 17a. Down-core median particle size and normalized magnetic susceptibility profiles of the most recent EL1 layer in cores 4A, 6A, 7C, and 9A-1K	99
Figure 17b. Locations of cores 4A-1K, 6A-1K, 7C-1K, 2C-1K, 8A-1K, and 9A-1K (supplement to Figure 17a).....	101
Figure 18. FTIR spectrum of chlorite found at the top of the EL1-A clay layer.....	103
Figure 19. Down-core median particle size and normalized magnetic susceptibility profiles of two EL2 layers from intervals 50-77 cm and 200-214 cm in core 6A-1K.....	104
Figure 20. Six core images of the EL1-A layer arranged west to east across the lake and description of the EL1-A layer facies.....	105
Figure 21. Three core images of the EL1-B layer arranged from west to east across the lake.....	107

Figure 22. Five core images of the EL1-C layer arranged from west to east across the lake	109
Figure 23. Two core images of EL1-D layer arranged from west to east across the lake	111
Figure 24. Five core images of EL2 deposits found in cores from the south (cores 5A-1K and 6A-1K) and north (cores 7C-1K and 8A-1K) basins	112
Figure 25. Simplified geologic map of Lake Crescent area combined with petrologic results of stream sands	113
Figure 26. Simplified geologic map of Lake Crescent area combined with petrologic results of EL1 sands	115
Figure 27. Simplified geologic map of Lake Crescent area combined with petrologic results of EL2 sands	117
Figure 28a. Isopach map of the EL1-A sediment thickness	119
Figure 28b. Standard prediction error map associated with interpolated EL1-A sediment thickness	120
Figure 29. 3-dimensional visualization of the EL1-A sediment thickness	121
Figure 30. Interpolated sediment thickness profiles generated from seismic lines in the north basin.....	123
Figure 31. Interpolated sediment thickness profiles generated from seismic lines In the south basin	124
Figure 32. Displacement wave straight line propagation distances with wave heights	125
Figure 33. Chlorite and basaltic sand laminations in the clay cap of core 7C-1K.....	126
Figure 34. Sediment core to seismic line correlation of core 2C-1K in the north basin	127
Figure 35. Sediment core to seismic line correlation of core 6A-1K in the south basin	129
Figure 36. Onshore and subaqueous portions of the Sledgehammer Point rockslide.....	131
Figure 37. Photograph of displacement wave straight line propagation distances with wave heights and faults.....	132
Figure 38. Historical landslide versus maximum wave run up height.....	133
Figure 39. Lognormal probability density distribution of earthquake recurrence on the Lake Creek-Boundary Creek fault	134

LIST OF APPENDICES

APPENDIX A. Photographs of radiocarbon dated organic samples	146
APPENDIX B. MATLAB script for Gaussian peakfitting of FTIR spectra	147
APPENDIX C. Photographs of sand grain types from the petrologic study	148
APPENDIX D. MATLAB script for interpolation of EL1-A layer thickness.....	152
APPENDIX E. Volume and mass calculations of megaturbidite EL1-A.....	153
APPENDIX F. Volume and mass error calculations of megaturbidite EL1-A	154
APPENDIX G. Calculation of the dry volume of annual normal sedimentation	155
APPENDIX H. MATLAB script for the bootstrap sampling of the power law coefficients.....	156
APPENDIX I. MATLAB script for lognormal probability distribution of earthquake recurrence.....	157
APPENDIX J. Magnetic susceptibility and median particle size data for EL1-A in core 2C-1K.....	158
APPENDIX K. Magnetic susceptibility and median particle size data for EL1-A in core 6A-1K.....	163
APPENDIX L. Magnetic susceptibility and median particle size data for EL1-A in core 8A-1K.....	169
APPENDIX M. Magnetic susceptibility data for EL1-A in core 4A-1K	174
APPENDIX N. Magnetic susceptibility data for EL1-A in core 7C-1K	176
APPENDIX O. Magnetic susceptibility data for EL1-A in core 9A-1K.....	180
APPENDIX P. Magnetic susceptibility and median particle size data for EL2 interval 50-77 cm in core 6A-1K.....	182
APPENDIX Q. Magnetic susceptibility and median particle size data for EL2 interval 200-214 in core 6A-1K.....	185

1.0 INTRODUCTION

Washington is one of the most seismically active and hazard prone states in the country due to its tectonic setting and climate. Most notably the state experienced the worst landslide disaster in the contiguous United States, the 2014 Oso landslide that resulted in 43 deaths and tens of million dollars of financial loss (Iverson et al. 2015). Although the external trigger of the Oso landslide was climatic, natural phenomena such as landslides and displacement waves can be generated by earthquake ground shaking. Lake Crescent, located on the Olympic Peninsula, is close to the most densely populated cities and complex infrastructure of Washington (Fig. 1); a region that would be strongly impacted by a high magnitude earthquake. Five earthquakes of magnitude 6.5-7.4 have shocked the Puget Sound region since its settling in the late 1880s (Rogers et al. 1996; Highland, 2003; U.S. Geological Survey, 2016). The earthquakes have resulted in several billions of dollars in public and private financial losses, 21 deaths, and hundreds of injuries (Rogers et al. 1996; Highland, 2003; U.S. Geological Survey, 2016). Furthermore, examinations of the oral traditions of Pacific Northwest Native American tribes provide additional context for the seismic history of the area during the Holocene prior to European settlement (Clark, 1953; Ludwin et al. 2005; 2007). Unfortunately, precision cannot be applied to any event recorded through oral traditions; therefore the historical record of earthquakes in this region is limited to less than 200 years.

Seismic events on the Olympic Peninsula are attributed to the Cascadia subduction zone (CSZ) and to faults embedded in the upper crust of the North America plate. Recent coastal and marine studies of the CSZ uncovered the potential for the 1100 km long

megathrust to produce great subduction earthquakes of $M_w > 8.0$ (Atwater, 1987; Goldfinger et al. 2003; Kelsey, 2005; Goldfinger et al. 2012; Fig. 1). The CSZ has been extensively studied; however there is little information available about the earthquake potential of the crustal faults identified along the northern Olympic Peninsula that in part accommodates stress produced by the convergence between the oceanic Juan de Fuca and continental North American tectonic plates. The majority of the upper-crustal faults that have been investigated in detail are close to the greater Seattle metropolitan region. On the Olympic Peninsula, three crustal faults run directly beneath Lake Crescent, one of which has been mapped by lidar, fault trenched, and confidently identified as active in the late Pleistocene to Holocene (Schasse, 2003; Polenz et al. 2004; Nelson et al. 2007; Fig. 1). Distinct landslide scars on the steep terrain that encloses the lake indicate the distinct possibility of secondary seismic hazards in addition to ground shaking from regional earthquakes.

Lacustrine sediment records have been used to reconstruct paleoseismicity in regions such as Lake Geneva, France-Switzerland (Kremer et al. 2015), Lake Le Bourget, France (Chapron et al. 1999), Lake Lucerne, Switzerland (Hilbe and Anselmetti, 2014), and several lakes in central Chile (Moernaut et al. 2014). The smaller-scale setting, relatively high sedimentation rates (~ 1 mm/yr), and potential for annual laminations in lake sediments provide a high resolution paleoseismic record that can be accessed and interpreted more easily than that of the marine realm (Chapron et al. 1999; Strasser et al. 2013; Moernaut et al. 2014; Hilbe and Anselmetti, 2014; Kremer et al. 2015), or from terrestrial fault trench studies (McCalpin, 1996). Subaqueous sediment density flows, such as turbidity currents, can generate a visible lithological change from normal sedimentation in both lacustrine and

marine sedimentary records (Talling, 2014; Chapron et al. 1999). Turbidity currents can be triggered by landslides, floods, and earthquakes; therefore a complete investigation into the basins geologic processes is needed to appropriately assign a source to a turbidite.

Seismically induced turbidites are distinguished by volume and basin-wide correlation (Talling, 2014). Turbidites, soft-sediment deformation features, and subaqueous mass wasting deposits are often used in conjunction to investigate ancient earthquakes and their subsequent impacts such as landslides and lake displacement waves (tsunamis) that may be recorded in lacustrine sediments (Strasser, 2003; Moernaut et al. 2014; Hilbe and Anselmetti, 2014; Kremer et al. 2015).

Lake Crescent is an exceptional recorder of seismic events for several reasons: 1) It is located in the minimally-anthropogenically disturbed Olympic National Park; 2) The two sub-basins of the lake have water depths of 140 to 190 m; 3) Its ultra-oligotrophic status allows for little to no productivity and minimal bio-disturbance of bottom sediments (Moran et al. 2013) and; 4) Fluvial input from perennial tributaries is minimal (Moran et al. 2013), thus turbidites caused by flooding are considered unlikely. This study uses high resolution seismic reflection and multibeam bathymetric surveys as well as sediment cores with radiocarbon dated material to provide a high resolution data set indicative of ancient earthquakes in an effort to improve our knowledge and develop hazard assessments for the north Olympic Peninsula, a tectonically and seismically active region where the historical record is less than 200 years long.

1.1 Geologic Setting

Lake Crescent is located within the northern foothills of the Olympic Peninsula along the Cascadia plate boundary. The peninsula is bordered by the Strait of Juan de Fuca to the north and the Pacific Ocean to the west. The CSZ, located offshore in the Pacific Ocean, tectonically dominates the geology of the Pacific Northwest from northern California to Vancouver Island. The Olympic Mountains make up the subaerial portion of the Cascadia accretionary wedge that is created by the oblique subduction of the Juan de Fuca plate beneath the North American plate (Engbretson et al. 1985; Wells et al. 1998; Parsons et al. 1998). The estimated 36 mm/yr rate of convergence has resulted in a large, east-plunging anticline composed of deformed Tertiary marine volcanic and sedimentary units beneath the Olympic Peninsula (Tabor and Cady, 1978a,b; Engbretson et al. 1985; Brandon and Calderwood, 1990; Clowes et al. 1996; Fig. 2). Fine and coarse sedimentary units known as the Olympic Subduction Complex (OSC) compose the core of the Olympic Mountains. The OSC is bounded by the Hurricane Ridge Fault and flanked by Paleocene-to-Eocene marine basalt and sedimentary rocks of the Crescent Formation (Tabor & Cady, 1978a, b; Engbretson et al. 1985; Brandon and Calderwood, 1990; Clowes et al. 1996; Brandon et al. 1998; Fig. 2). Mt. Olympus, the tallest peak of the Olympic Mountains, is located in the central OSC at a height of 2,432 m (National Park Service, 2016; Fig. 2). The Olympic Mountains are considered to be in a flux steady state, meaning that the rate of the material accreted into the subduction complex is balanced by the volume of material eroded from the surface (Brandon et al. 1998; Willet and Brandon, 2002).

The northern Olympic Peninsula was at times extensively glaciated during the Quaternary. The foothills and lowlands flanking the saltwater were buried beneath the ~1 km thick Juan de Fuca lobe of the Cordilleran ice sheet as recently as ~14 ka (Dethier et al. 1995; Schasse, 2003). The valley occupied by Lake Crescent was almost certainly over-deepened by erosion of the Juan de Fuca lobe as it advanced and retreated across the study area (Tabor, 1975). In the vicinity of Lake Crescent, the late Quaternary glacial advances and retreats deposited till, outwash, and glaciolacustrine terrace deposits along adjacent valley floors and walls (Heuser, 1973; Schasse, 2003; Fig. 2).

1.2 Tectonic Setting and Earthquake History

Western Washington is subject to frequent earthquakes of varying magnitudes due to its location above the CSZ. Previous paleoseismic investigations reveal that great subduction zone earthquakes ($M_w \geq 8.0$) occur every 300-500 years (Atwater and Hemphill-Haley, 1997; Goldfinger et al. 2012; Fig. 1). These paleoseismic investigations are evidenced by turbidites and subaqueous landslide deposits in lacustrine and marine environments (Karlin and Abella, 1992; Goldfinger et al. 2003; Goldfinger et al. 2012), sand deposits found in marshes and low-elevation coastal lakes from the landward migration of tsunamis (Atwater and Moore, 1992; Kelsey et al. 2005), and coseismic subsidence allowing for estuarine environments to form stratigraphically above marsh environments (Atwater, 1987; Atwater and Yamaguchi, 1991, Shennan et al. 1996). Full rupture of the CSZ has occurred 13 times in the past 7,500 years with the last megathrust event occurring on January 26, 1700 CE (Satake et al. 1996; Yamaguchi et al. 1997; Atwater and Hemphill-Haley, 1997; Goldfinger et al. 2012). Small to moderate magnitude ($M_w < 7.1$) earthquakes that occur at depths > 40 km in the Puget Sound

lowland are correlated with the well-defined, shallowly dipping Benioff zone of the CSZ (Rogers et al. 1996). Two of the largest historical earthquakes were intraslab Benioff zone events that occurred in 1949 ($M_w = 7.1$) and 2001 ($M_w = 6.8$) at depths of 50 and 59 km (Rogers et al. 1996; Highland, 2003). Low to moderate magnitude earthquakes that occur at depths < 10 km are caused by the rupture of upper-crustal faults within the North American plate (Rogers et al. 1996). The largest historical upper-crustal fault earthquake occurred in 1996 at a depth of 8 km ($M_w = 5.6$) (U.S. Geological Survey, 2016).

Subduction zones that exhibit oblique convergence create a supplementary seismic hazard as the forearc blocks break apart and shift parallel to the tectonic margin (McCaffrey, 1994; Wells et al. 1998; Wells and McCaffrey, 2013). Models based on paleomagnetism and GPS geodesy show that at the latitude of the north Olympic Peninsula, the Pacific Northwest is rotating clockwise at 2.0 degrees/Ma, while the Puget Sound region experiences north-south shortening of ~ 4.4 mm/yr that decreases to a negligible rate near southern British Columbia (Wells et al. 1998; Mazzotti et al. 2002; McCaffrey et al. 2007; Wells and McCaffrey, 2013). Several active east-west trending faults in the Olympic Mountains and Puget Sound region appear to distribute stress caused by the crustal contraction, three of which run beneath both of Lake Crescent's basins (Johnson et al. 1994; Wells et al. 1998; Mazzotti et al. 2002; McCaffrey et al. 2007; Wells and McCaffrey, 2013; Fig. 3). Wells et al. (1998) provides an analog of the upper-crustal faults that accommodate stress produced by the oblique subduction of the CSZ to the Median Tectonic Line of southwest Japan where a catastrophic magnitude 6.9 earthquake occurred on a crustal strike-slip fault that was possibly accommodating the oblique component of the subduction zone. The inland, shallow

earthquake devastated the town of Kobe and resulted in approximately 5,000 deaths, the second worst Japanese earthquake of the 20th century (Kanamori, 1995). The recent seismicity and geologic similarity of the two regions provide a plausible postulation that risk emphasis should be placed on crustal faults in addition to the CSZ.

The Lake Creek-Boundary Creek fault, herein named Sadie Creek fault, and Barnes Creek fault are vertical to north-dipping, oblique thrust faults that control the valleys around Lake Crescent (Fig. 3). The Barnes Creek fault was first mapped by Tabor and Cady (1978a, b) from the east shore of Lake Crescent's southern basin 15 km to the Elwha River. Dragovich et al. (2002) extended the fault another 14 km west to run beneath the lake's south basin and glacial deposits. No unequivocal evidence for Quaternary activity has been reported (Tabor and Cady, 1978a, b; Dragovich et al. 2002; Lidke, 2003).

The Lake Creek-Boundary Creek fault exhibits oblique right-lateral dip slip motion, as is supported by LiDAR mapping, fault trenching, and field mapping (Brown et al. 1960; Tabor and Cady, 1978a,b; Schasse, 2003; Polenz et al. 2004; Schasse et al. 2004, Nelson et al. 2007; Fig. 3). Fault scarps preserved in the landscape east of the Elwha River were used to estimate that the Lake Creek-Boundary Creek fault post-dated regional glaciation (< c. 13 ka) (Haugerud, 2002; Polenz et al. 2004; Schasse, 2004). Polenz et al. (2004) observed fault scarps on outwash terraces deposited c. 13 ka but not in late Pleistocene alluvium that was deposited just after the outwash terraces. Fault scarps west of the Elwha River associated with the Lake Creek-Boundary Creek fault could not be accurately distinguished from widespread valley-margin landslide scarps, but surface faulting, visible in lidar imagery east of the Elwha River extends for 22 km (Polenz et al. 2004; Nelson et al. 2007). Fault

trenching east of the Elwha River produced radiocarbon evidence that suggests two surface-rupturing earthquakes have occurred between 2,000 and 600 yr BP (Nelson et al. 2007). In addition, a possible earlier surface faulting event c. 5,000 years ago was evidenced in a second trench 1 km west of the primary site (Nelson et al. 2007). The existence of surface faulting associated with the Lake Creek-Boundary Creek fault west of the Elwha River was not confidently identified until 2015 lidar imagery revealed topographic lineaments (inferred scarps) west of Lake Crescent's northern basin along the Sadie Creek fault (Fig. 4). The right-lateral motion shown by the offset drainage pattern of small stream valleys indicates the western half of the Lake Creek-Boundary Creek fault and the Sadie Creek fault zone is active and has generated surface-rupturing earthquakes around and most likely beneath the northern portion of Lake Crescent since regional deglaciation c. 14 ka.

Multiple mapped rockslides exist along the trace of the Lake Creek-Boundary Creek fault between Lake Crescent and the Elwha River (Logan and Schuster, 1991; Schasse, 2003; Fig. 3). Mapped rockslide deposits within the Lake Crescent catchment total 11.3 km², roughly 10% of the lake's catchment area. Bathymetric surveys of the lake as part of this project revealed large subaqueous rockslide deposits in addition to the previously-identified subaerial portions. The largest landslide, herein named the Lake Sutherland rockslide complex, split ancestral Lake Crescent into two lakes, Crescent and Sutherland (Tabor, 1975; Logan and Schuster, 1991; Fig. 3; Fig. 5).

Logan and Schuster (1991) determined that the Lake Sutherland Rockslide complex is a result of several rockslides originating from the north and south valley walls (Fig. 3; Fig. 5). The blockage resulted in a change to the ancestral outlet from the eastward flowing Indian

Creek to the north flowing Lyre River. In addition, the rockslide dam caused the surface water elevation of Lake Crescent to increase by 24 m (elevation difference between the heads of Indian Creek and the Lyre River) as well as the genetic isolation of rainbow and cutthroat trout in Lake Crescent (Pierce, 1984; Logan and Schuster 1991; Brenkman et al. 2014). The Lake Sutherland rockslide complex was previously estimated by Pringle et al. (2010) to have occurred around $4,340 \pm 50$ years ago by radiocarbon dated growth rings in a preserved, submerged, and drowned tree at the west end of the lake's south basin. An older mass wasting event, known as the Mount Storm King rockslide (Fig. 3; Fig. 5), was sourced off the north flank of this mountain. Preliminary radiocarbon dating of sediments accumulated in a closed depression formed on the top of this rockslide indicates that it occurred prior to 5,180 cal yr BP (see results section).

Oral traditions of Pacific Northwest Native American tribes reveal an interesting backstory to the Mount Storm King rockslide. Clark (1953) describes a battle between the Klallam and Quillayute peoples near the shores of the Strait of Juan de Fuca. After two days of fighting and countless deaths, infuriated Mount Storm King broke off a great piece of rock from his head and threw it down into the valley killing all of the warriors and splitting the lake in two (Clark, 1953). Although the story is but a legend, its existence does strengthen the evidence that landslides around Lake Crescent have occurred in the late Holocene and likely were witnessed by local inhabitants.

1.3 Lake Crescent Catchment

Lake Crescent occupies an area of 20.3 km² at the northern boundary of Olympic National Park (average latitude 48° 3' N; longitude: 123°48' W). It is composed of two deep, elongated basins connected by a bathymetric sill. The basins trend east-west and have a surface elevation of 177 m. The basins are characterized by steep slopes that lead to flat bottoms whose depths are 140 m in the north and 190 m in the south. The west portion of the south basin is a recessional glacial moraine that formed during the regional retreat of the Juan de Fuca lobe of the Cordilleran ice sheet, approximately 14 to 13 ka (Logan and Schuster, 1991; Polenz et al. 2004).

The lake is enclosed by mountainous terrain that reaches elevations of over 1,300 m (1,477 m above sea level) from the surface of the lake. The surrounding 110 km² catchment is dominated by conifer trees although the abundance of deciduous species changes with elevation (Moran et al. 2013). Anthropogenic influence on the watershed is relatively sparse; however recent development that increased nitrogen and phosphorus runoff to the lake has threatened the water quality and its ultra-oligotrophic status (Moran et al. 2013). Visitor centers, boat ramps, camping facilities, hotels, and about 150 private homes are found around the 37.9 km of shoreline (National Park Service, 2016).

Climate is highly variable over the extent of the Olympic Peninsula; however Lake Crescent's catchment lies within a temperate, maritime region (Henderson et al. 1989). Precipitation fluctuates along the length of the lake's catchment but averages 150 cm annually (PRISM Climate Group 2012; Moran et al. 2013). Moran and others (2013) define six of the 32 tributaries in the watershed as substantial (discharge > 0.03 m³s⁻¹): Barnes

Creek, Smith Creek, Lapoel Creek, Fairholm Creek, and Piedmont Creek (Fig. 6). The largest tributary, Barnes Creek, sources a delta that progrades from the southeastern corner of the lake. The Lyre River, located at the western side of the north basin, is the only egress channel. It has a mean discharge of $6.06 \text{ m}^3\text{s}^{-1}$ and flows northward to the Strait of Juan de Fuca (Moran et al. 2013). Waterfalls along the Lyre River serve as physical barriers to upstream migrating anadromous fish.

Lake Crescent's northern basin is rimmed by three sedimentary units: the Hoko River, Lyre, and Aldwell Formations (Fig. 7). These middle to upper Eocene marine formations consist of thin to medium bedded siltstone, sandstone, and conglomerate (Babcock et al. 1994; Schasse, 2003). The middle to lower Eocene Crescent Formation traverses the middle of the lake flanking shores of both lake basins (Fig. 7). It is composed of marine basaltic rocks with locally interbedded siltstone, sandstone, conglomerate, limestone, and chert (Babcock et al. 1994; Schasse, 2003). Abundant chlorite and zeolites are found in the pillow-dominated basalt (Babcock et al. 1994; Schasse, 2003). The lower Eocene Blue Mountain Unit of Tabor and Cady (1978a, b) borders the south basin of the lake (Fig. 7). This marine sedimentary unit is composed of sandstone, siltstone, and argillite (Babcock et al. 1994; Schasse, 2003). Repeated Pleistocene advance and retreat of Cordilleran ice sheets resulted in local outwash and till deposits along the west ends of both basins (Schasse, 2003; Fig. 7), and almost certainly the erosional carving of the Lake Crescent basin along fault-weakened structural trends (Tabor, 1975).

2.0 METHODS

2.1 Seismic Reflection Survey

In 2013 approximately 75 km of high resolution Chirp seismic imagery was collected in Lake Crescent (Fig. 7). The seismic data were collected using an Edgetech SB-512i system placed 1.25 m below the surface using a catamaran towed 10 m behind a boat that was run at a speed of 2.5-3.0 knots. The Edgetech SB-512i system operated at a 2-12 kHz sweep-frequency pulse with 20 ms duration. Tracklines were georeferenced with an accuracy of 1-3 m using a WAAS-enable GPS. Seismic reflection profiles were generated using a two-way travel time of 1500 m/s (Jensen et al. 2011).

2.2 Sediment Coring

During early September 2015, approximately 63 m of piston and gravity sediment cores were retrieved using the R/V KRKII, a platform equipped with a Kullenburg coring system (Kelts et al., 1986) supplied and operated by personnel of the National Lacustrine Core Facility (LacCore) at the University of Minnesota (Fig. 8). All cores were lined with 7 cm polycarbonate tubes housed in metal casings. The piston cores were extracted from the metal casings and divided into ≤ 1.50 m sections on the shore of the lake. The piston cores ranged in total length from 0.41-7.90 m (Table 1) and the gravity cores ranged from 0.09-0.55 m long. The gravity cores were recovered to retrieve intact shallow sediments that otherwise could be disturbed in the piston cores. A gravity core was not extracted from each piston core site. In addition, some of the gravity cores were not recovered simultaneously with the piston cores due to mechanical malfunction and sediment consistency of the lake bottom. It is important to note that an undetermined amount of core 2A-1K may have been

lost due to the lack of a core catcher at the end of the barrel. The upper 2/3 of core 7A-1K was disturbed upon on-shore extraction from the metal casing. All cores were capped, labeled, sealed, and transported to LacCore where they were placed in refrigerated storage.

During the same week, a soil pit was dug into a closed depression (CD 1) on the Mt. Storm King rockslide to attempt to provide a limiting age constraint. Charcoal was recovered from the side wall of the pit at 90 cm depth (Table 2).

2.3 Multibeam Bathymetric Survey

A high resolution bathymetric survey of Lake Crescent was conducted in February 2016 by the crew of the U.S. Geological Survey's *R/V Snavely* operating a 100 kHz Reson 7111 multibeam system that returns both bathymetry and back-scatter intensity with individual beam arcs of 1.9° along-track and 1.5° across-track (Fig. 8). Data (pixel resolution ~2.5 m) were collected over swath widths three times the water depth at speeds of <5 nm/hr and the survey tracks were positioned to give at least 25% overlap. Differentially corrected GPS navigation data was passed through an inertial measurement unit to the system hardware and data collection software. The multibeam data was post-processed into a georeferenced raster file (2.5 m grid-spacing).

2.4 Core Sampling

Core analysis was completed at LacCore during early October 2015. First, whole cores were placed on a Geotek Multisensor Core Logger track to measure sediment density, acoustic wave velocity, electrical resistivity, and loop-sensor magnetic susceptibility at 5 mm resolution. Cores were split in half using vibrating cast saws and smoothed with glass slides to prepare the core for imaging. Archival core halves were placed in cold storage. The

working core halves were placed on a track and imaged using a Geotek Geoscan-IV at 5 mm resolution. Next, the core halves were moved to a new track to be scanned by a Geotek XYZ multisensor core logger for high resolution point-sensor magnetic susceptibility and color spectrophotometric reflectance at 5 mm resolution. Sediment samples were taken next using a high resolution (usually 1 cm) sampling rate through the core halves. All sediment samples were placed in labeled plastic containers. Descriptions of sediment were made simultaneously with sediment sampling using the high resolution images generated during this process. Observed macroscopic organic material was removed and placed in glass vials as found throughout the cores. Sediment and organic samples were sent to North Carolina State University (NCSU) and placed in a freezer.

2.5 Radiocarbon Dating

Nitrile gloves were worn at all times in the NCSU laboratory to minimize potential contamination of the organic samples with modern carbon. Organic samples were stored in a freezer until sample preparation. All metal and glass ware were combusted at 550°C prior to use except for sieves. The sieve washing procedure is as follows: deionized water (DI), methanol, acetone, methanol, DI water. The Acid/Base/Acid sample pre-treatment method was used to prepare all carbon samples for dating (Olsson, 1986). The samples were thawed and cleaned in a Fisher Scientific FS30H ultrasonic cleaner for 45 minutes to remove surface contamination. The samples were washed with DI water in a sieve multiple times to remove any excess surface contamination. The samples were then photographed, described, and placed into individual labeled beakers. The organic samples consisted of woody stick

fragments, fibrous roots, twigs, needles, and leafy matter (Appendix A). The methods described below for one sample was applied to all of the samples.

A water bath was heated to a maximum of 70°C using a Corning stirrer/hot plate. 1N hydrochloric acid (HCl) was added to the beaker to cover the sample. This acid rinse is used to dissolve any soil carbonate left after the sample preparation (Olsson, 1986). The sample was covered in foil and left in the heated bath for 30 minutes. An individual, labeled syringe was used to pipette the HCl from each sample beaker. The sample was then submerged completely in 1N sodium hydroxide (NaOH). The sample was covered in foil and left in the heated bath for 1 hour. The rinse turns the NaOH brown as it removes alkaline soluble humics from the surface of the sample (Olsson, 1986). A syringe was used to pipette the brown NaOH from the beaker. These steps were repeated until the NaOH rinse becomes clear. The sample undergoes one last HCl wash to remove any atmospheric carbon it accumulated during the NaOH washes (Olsson, 1986). The sample was covered in foil and submerged in HCl for 30 minutes in the heated bath. The sample was brought back to a neutral pH by submerging it in DI water in the heated bath for 5 minute intervals. Fisherbrand pH test paper was used to measure the solvent pH. The DI water rinses were repeated until the pH was 7. Lastly, the sample was dried by lowering the hot plate temperature to 30°C and covering it with foil. After the sample had dried, a clean spatula was used to place it in a previously cleaned, tightly covered and labeled glass vial. Organic samples were then sent to Direct AMS in Seattle, Washington for Accelerator Mass Spectrometer (AMS) analysis. AMS results are reported as the fraction modern carbon for each sample, where modern represents the year 1950 CE and as uncalibrated radiocarbon

ages with 1-sigma uncertainties. CALIB 7.1 software (Stuiver and Reimer, 1986) was used to calibrate the results (cal yr BP) utilizing the IntCal13 calibration curve (Reimer et al. 2013).

2.6 Fourier Transform Infrared Spectroscopy

Portions of the clay from the sediment samples obtained at LacCore that exhibited distinct fine-scale green layers were dried overnight using a Labconco Freeze Dry System. The samples were labeled, placed in vials, and transported to the North Carolina State Museum of Natural Sciences. All research executed at the museum was under the direction of the Curator of Geology, Dr. Christopher Tacker. A suite of chlorite minerals was provided from the museum collection to use as a reference in the identification of the unknown green clay samples. The chlorite reference minerals and clay samples were hand-ground with a mortar and pestle. All samples were placed into labeled glass vials. The mortar and pestles were cleaned thoroughly between samples with soap and warm water. After the wash, a sand mixture was ground in the mortar and pestle to remove deep scratches left from the samples after the first wash.

Attenuated transform reflectance - Fourier transform infrared spectroscopy (ATR-FTIR) was performed on the samples using a Thermo Scientific 6780 FTIR spectrometer, with an attached Continuum IR microscope and Smart iTR attachment for the bench spectrometer. Each ground sample was placed on the diamond plate of the iTR attachment where the machine discharges an infrared beam at the sample. The total reflectance of the beam off the sample generates a spectrum distinct to its chemical composition. The spectra were generated by Thermo Scientific OMNIC Spectra Software with a 4 cm^{-1} resolution.

Gaussian peak fitting of the spectra was performed in MATLAB R2014a software to determine peak height. An in-house Matlab script from previous research (C. Tacker, 2015, personal communication) served as the baseline procedure in the deconvolutions of the peaks. It runs by allowing the operator to isolate a region of interest in the spectrum, pick the endpoints for a linear background correction, subtract the linear background, then use the curve fitting toolbox to generate the following parameters: a = peak amplitude, b = peak centroid (wavenumber), and c = peak width. The reported b parameter serves as the diagnostic factor in determining the chemical composition of the sample. The Matlab script used for Gaussian peak fitting is presented in Appendix B.

2.7 Sediment Analysis

2.7.1 Particle Size Analysis

Size distributions for core sediments were determined with a Beckman Coulter LS13-320 Laser Diffraction Particle Size Analyzer outfitted with a Universal Liquid Module that measures particle sizes between 0.04 and 2000 microns.

2.7.2 Boundary Shear Stresses

The boundary shear stresses of flows required to move various particles of the EL1 layer were calculated assuming they moved as suspended load. The minimum boundary shear stress required to move the silt and sand-size particles were calculated based upon the settling velocity of different sized particles using the Rouse Parameter (P) (Rouse, 1946). The ratio between settling velocity and turbulent diffusion of sediment away from the bed states that if $P < 0.8$ then the sediment moves as suspended load. Boundary shear stresses were calculated using parameters that are temperature dependent. A near bottom temperature

of 10°C was obtained in 2007 from water temperature profiles collected by Dr. Steven Fradkin, limnologist at Olympic National Park's Lake Crescent Laboratory, and was used in the following calculations (see Table 3 for list of parameters).

For silt-sized particles:

$$W_s = \frac{(\rho - \rho_w)gD^2}{18\mu}$$

$$p = \frac{w_s}{ku_*}, \text{ where } p = 0.8 \text{ (suspended sediment load)}$$

$$\tau_b = \rho u_*^2$$

For sand-sized particles:

$$D_* = \frac{(\rho_s - \rho)gD^3}{\rho v^2}$$

$$W_s = \left[\frac{w_*(\rho_s - \rho)gv}{\rho} \right]^{1/3}$$

$$p = \frac{w_s}{ku_*}, \text{ where } p = 0.8 \text{ (suspended sediment load)}$$

$$\tau_b = \rho u_*^2$$

2.7.3 Sand Petrology

The sand used in the petrology study was sieved and cleaned at NCSU before being sent to National Petrographic Services, Inc. for thin section mounting. Thin sections were examined with an Olympus CH-2 system microscope. The Gazzi-Dickinson point counting method was implemented for this study (Dickinson, 1970). The grains were examined and sorted into 16 mineral and rock fragment types then into four recalculated parameters by an operator (Table 4). The operator moved through the thin section in a rough grid pattern using

a sliding mount while counting and identifying all the grains in view. Each thin section was examined for a total of 300 grains and totals for each parameter were recorded. Pictures of grain types are included in Appendix C.

2.8 ArcGIS Modeling

Volume estimation of the entire here-named “Sledgehammer Point rockslide” was executed in ArcGIS ArcMap 10.3.1 using spatial data projected into the UTM Zone 10, WGS 1984 coordinate system. First, the area (m^2) of the mapped rockslide polygon was calculated. Next, the predicted volume of a given rockslide area was estimated by a bedrock rockslide geometry scaling relationship derived from Larsen et al. (2010) dependent upon a given scaling exponent $\gamma = 1.35$ and intercept $\alpha = 0.186$ such that $V = \alpha A^\gamma$. These scaling values were chosen because the area of the rockslide is $> 5,000 \text{ m}^2$ (Larsen et al. 2010) and the assumed failure plane is tens of meters beneath the pre-failure hillslope surface.

The volume of the subaqueous portion of the Sledgehammer Point rockslide was completed by first establishing points that surround the rockslide debris using the 3 m resolution bathymetric raster as a reference. Bathymetric raster values were assigned to the points using the *Extract Values to Points* tool. The points were interpolated using the ordinary kriging method with a K-bessel model type within the ArcGIS Geostatistical Wizard in order to produce a raster of the pre-rockslide lake bathymetry. The kriging prediction map was converted to a raster using the *Layer to Grid* tool in Geospatial Analyst.

Next, the points were used to make a polygon shapefile enclosing the rockslide debris. The 2.5 m resolution bathymetric and kriging rasters were extracted by mask to the shape of the polygon. The kriging raster was subtracted from the 2.5 m resolution

bathymetric raster using the raster calculator tool and then multiplied by its cell resolution. The multiplied raster and rockslide debris polygon was input into the *Zonal Statistics as Table* tool, producing a data table in which the “sum” category is the volume of the multiplied raster in cubic meters.

The volume of the first distinctive, acoustically transparent layer observed beneath the lake bed in the Chirp seismic reflection data was estimated by a series of steps using various software packages. High resolution seismic reflection surveys of the sub-bottom lake stratigraphy were generated using the default JSF files generated by the Edgetech Discover SB 3200-XS program. The seismic reflection surveys were converted to standard SEG-Y IBM Floats (1) ASCII format. The SEG-Y files were imported to HYPACK 2016 for digitization of the layers seen in the sub-bottom stratigraphy. The elevation of the lake bed was calculated by manually picking out the sediment-water interface in the seismic reflection surveys with the assumption that the freshwater seismic velocity is 1500 m/s. The acoustically transparent layer was digitized by tracing a reflector above and below the seismically transparent portion of the layer. Each reflector was traced by georeferenced points and exported as individual reflector ASCII X,Y,Z text files containing values of easting, northing, depth, and thickness for each digitized point.

MATLAB R2014a was utilized to produce a script that interpolated the thickness of the layer between the manually picked points (Appendix D). First, the ASCII X,Y,Z text files were imported into MATLAB and easting and northing was converted to latitude and longitude. The latitude and longitude of the top and bottom reflectors were interpolated with the new line lengths dependent upon the bottom reflector length. The thickness was predicted

for both reflectors given their individual latitude and longitude distances, depth of points, and interpolated distance points. Finally, the predicted thickness of the top reflector was subtracted from the predicted thickness of the bottom reflector to give a final interpolated data set of latitude, longitude, and thickness (X,Y,Z) for each Chirp line.

The Chirp X,Y,Z data was imported into ArcGIS ArcMap 10.3.1 to create isopach maps of the megaturbidites and estimate their volumes. The projected coordinate system used was WGS 1984 UTM Zone 10. The Chirp data were separated into three sections: north basin, south basin, and small south basin. The following procedure was executed for the three basins. First, zero points were made outlining the basin shape where X,Y,Z data existed. The points were georeferenced and then converted to a polygon shapefile. A new .csv file of georeferenced zero and Z points was interpolated using the ordinary kriging method with a K-bessel model type available in the Geostatistical Wizard to produce a prediction surface map. The prediction map was then converted to raster format with the Geospatial Analyst *Layer to Grid* tool. Next, the raster images were extracted by mask to the shape of the basin polygon. The Raster Calculator was used to multiply the extracted, interpolated raster by its cell resolution. The output raster of the calculator and polygon of the basin was input into the *Zonal Statistics as Table* tool, outputting the volume of the multiplied raster in cubic meters. The conversions to wet sediment mass, dry sediment mass and dry sediment volume are reported in Appendix E.

A prediction standard error surface map was also generated in the Geostatistical Wizard to measure the statistical accuracy of the prediction surface map. It is important to note that the standard error only reflects data locations, not data values. The prediction

standard error surface map was used to produce an error estimate for the megaturbidite volume based upon the number of pixels in each interval of the prediction standard error surface range. First, the prediction standard error surface map was input as the conditional raster in the *Con* tool using an expression statement where $VALUE \leq 0.1$. The input true constant value is 1 and the input false constant value is 0 such that the output raster has values of 1 where the pixels are ≤ 0.1 . This was completed for each of the following ranges: 0-0.1, 0.1-0.2, 0.2-0.3, and 0.3-0.4. The number of pixels for each range is identified in the symbology heading of the *Con* output raster properties. The number of pixels for each range is multiplied by the prediction standard error raster cell resolution and the midpoint of the range to produce an overall volume estimate error (Appendix F).

2.9 Displacement Wave Heights

The displacement wave height estimates were derived following Evers and Hager (2016) whose empirical equation predicts displacement wave heights generated by rapid subaerial landslides with 30% error. The empirical equation was derived by comparing wave heights generated by the scaled-down model of subaerial landslides to measurements predicted from the equation. The Evers and Hager (2016) equation was derived by combining parts of the empirical equations of displacement wave propagation by Heller et al. (2009) and Heller and Spinneken (2015).

Heller et al. (2009) equations:

$$F = \frac{V_s}{(gh)^{\frac{1}{2}}}$$

$$S = \frac{s}{h}$$

$$M = \frac{m_s}{p_w b h^2}$$

$$P = F^{\frac{1}{2}} M^{\frac{1}{4}} \{\cos([6/7]\alpha)\}^{\frac{1}{2}}$$

Heller and Spinneken (2015) equation:

$$f_\gamma = \cos^{2\{1+\exp[-0.2(r/h)]\}}(2\gamma/3)$$

Evers and Hager (2016) equation:

$$\frac{H}{h} = 2P\left(\frac{r}{h}\right)^{-1} f_\gamma$$

The equations are dependent upon many fixed parameters (Fig. 9; Table 5); most of which were calculated in ArcGIS. The slide velocity is assumed to be 45 m/s. This estimate is based upon the 60 m/s velocity of a similar slide in Chehalis Lake, British Columbia whose vertical fall was steeper than the Sledgehammer Point rockslide (Roberts et al. 2013). The propagation distance, propagation angle, and still water depth of each scenario was calculated in ArcGIS (Fig. 9; Table 6). The wave propagation distance (r) traveled by the wave is assumed to be in the shape of a straight line from the point the rockslide enters the water to the scenario location. The propagation distance is the point just before the flat basin bottom starts to transition to the steep-sided lake margin. Due to the variability and uniqueness of lakes, wave heights on the slope cannot be calculated without numerical

models; therefore the empirically derived equation can only be estimated for wave heights in the deep basin prior to breaking against the shoreline. The still water depths of the “opposite shore” and “Nature Bridge” scenarios are assumed to be 100 m. This “midpoint” depth was picked because the present day depths are 60-70 m where the subaqueous portion of the Sledgehammer Point rockslide is deposited and the pre-rockslide surface was most likely not deeper than 140 m (maximum depth of the north basin).

3.0 RESULTS

3.1 Seismic Stratigraphy

The maximum depth of seismic penetration into sediments beneath the lake floor from the 2013 Lake Crescent Chirp survey was approximately 20 m in the deeper basins, decreasing along the steep lake margins. Acoustic penetration in areas that contain subaqueous portions of rock slide deposits is limited to a maximum of 5 m. Three discrete subsurface seismic facies are differentiable across both of the deep basins of the lake.

Seismic Facies A is characterized by laterally continuous and parallel, alternating-high-to-low amplitude reflectors that suggest uniform lake-wide sediment emplacement on top of the pre-existing lake floor topography (Fig. 10; Fig. 11; Fig. 12; Fig. 13). The laminated *Seismic Facies A* sequences are typically 2-4 m thick and are visible across the entirety of the lake.

Seismic Facies B is characterized by a thick (usually 1-2 m), extensive, and onlapping chaotic to seismically-transparent unit (Fig. 10; Fig. 11; Fig. 12; Fig. 13). Below the chaotic to transparent unit is a basal, high-amplitude reflector that exhibits hummocky morphology. The hummocky morphology of the basal, high-amplitude reflector is smoothed out by the thick overlying chaotic to seismically-transparent unit. The meter-scale thickness of *Seismic Facies B* extends over the entire floor of both the north and south basins, but thins in shallower depths. Resolution of *Seismic Facies B* thickness on steeper side slopes at < 95 m water depth is unattainable from the 2013 Chirp seismic survey data.

Seismic Facies C is characterized by wedge shaped layers that interfinger with sequences of *Seismic Facies A* and *B* (Fig. 13). These < 1 m thick wedge-shaped layers are thickest in a shoreward direction and taper to non-existence towards the basin centers.

3.1.1 North Basin Stratigraphy

The uppermost 2 m of seismic stratigraphy from the north lake basin is undeformed seismic facies A that overlays a 1.5-2 m thick *Seismic Facies B* sequence. The hummocky morphology of the basal unit of *Seismic Facies B* is a pronounced scour surface that has eroded a portion of underlying *Seismic Facies A* (Fig. 11). In some parts of the basin, *Seismic Facies B* is consecutively amalgamated against underlying (older) *Seismic Facies B* deposits (Fig. 11). Other portions of the basin show *Seismic Facies B* separated by several meters of *Seismic Facies A* (Fig. 10). A maximum of five *Seismic Facies B* sequences are observable in the 2013 Chirp data from the north basin. Offset and folded layers of *Seismic Facies A* and *B* are observed where the seismic track lines cross the presumed trace of the Lake Creek-Boundary Creek fault and Sadie Creek faults at high angles. Structural (fault) offset across the Sadie Creek fault progressively increases ~1 m with depth beneath the lake floor each time a *Seismic Facies A-B* pair is passed (Fig. 11).

3.1.2 South Basin Stratigraphy

In the center of the south basin, *Seismic Facies A* extends to 4 m below the sediment-water interface and it thins toward the Barnes Creek delta (Fig. 12). It is underlain by a 1.5 m thick *Seismic Facies B* layer that truncates up to 1 m of the underlying *Seismic Facies A* sediments that in turn overlie another ~ 1.5 m thick *Seismic Facies B* unit (Fig. 12). The basal surface of the upper *Seismic Facies B* deposit is less irregularly shaped than what is observed

in the north basin. The thickness of *Seismic Facies A* and *B* decreases to the west making it difficult to distinguish the two past 123°52'W longitude. *Seismic Facies C* sporadically interfingers with the thinner *Seismic Facies A* and *B* deposits along the margins in the western portion of the basin (Fig. 13). The strata of the south basin retain no obvious record of fault-related deformation.

3.1.3 Subaqueous Rockslide Deposits

Several subaqueous rockslide deposits were identified in the channel between the north and south basins. The seismic profiles of the deposits reveal tens of meters of topographic relief, with supra-slide depressions filled with up to 2 m of *Seismic Facies A* sediments (Fig. 14). *Seismic Facies B* deposits are not observed on the rockslide. There is a smaller subaqueous rockslide deposit in the eastern portion of the north basin that contains no intra-deposit depressions (Fig. 15).

3.2 Sedimentology

Sediments extracted from our Lake Crescent cores show slowly accumulated, “background” deposits intercalated with distinct event layers. Normal or “background” sedimentation records the slow accumulation of fine-grained particles by settling from the water column. The background sediment is composed of laminated, light gray to brown diatomaceous silt. Event layers are distinguished from background sediment by a change in thickness, particle size, lithology, and sedimentary structures. Particle size and magnetic susceptibility analysis of core sediments indicate the presence of four types of event layers (Pollen, 2016), but only two will be described in this study. Down-core magnetic susceptibility profiles of cores are used as a proxy for grain size, as a high correlation was

found between the two parameters (Fig. 16). Magnetic susceptibility values were normalized by applying the equation $x_{new} = \frac{x-x_{min}}{x_{max}-x_{min}}$ so that the broad range of values would have a common scale.

The first type of event layer (EL1) is observable in all cores recovered from the deep portions of the north and south deep basins and range in thickness from 22 cm (core 4A-1K) to 230 cm (core 7C-1K). Four distinct EL1 deposits are found in the suite of piston cores. EL1 deposits in deep basin cores are characterized by an irregular, scoured base overlain by 40 cm thick medium-grained basaltic sand and interspersed organic material that fines upward into graded fine-grained basaltic sand (Fig. 20). The sandy base layer is characterized by both large grain size (100-2000 μm) and high magnetic susceptibility values (1000-3000 SI) (Fig. 16; Fig. 17a,b). A homogenous dark brown silt layer lies above the sandy basal layer. The silt layer ranges in thickness from 100 to 130 cm in deep basin cores and is characterized by relatively constant magnetic susceptibility values (500-700 SI) that slightly decrease upward (Fig. 16; Fig. 17a,b). The homogenous silt layer is 17 cm thick in core 4A-1K and 16 cm thick in core 9A-1K. Light brown clay overlies the silt layer with an average thickness of 2.5 cm in the south basin and 9 cm in the north basin. Magnetic susceptibility values sharply decrease for this clay-rich layer to near zero (Fig. 16; Fig. 17a,b). A ≤ 5 cm sequence of thin green clay, basaltic sand, and fine-grained brown to light gray silty clay laminae tops the clay layer. FTIR analysis of the green clay indicates that it is dominated by chlorite (Fig. 18; Table 7). This sequence is ≤ 2 cm thick in the core 4A-1K EL1 layers and is nonexistent in the EL1 layers from core 9A-1K. EL1 deposits located closer to the lake

margin and in shallow depths (cores 4A-1K and 9A-1K) are much thinner than their basin counterparts (Fig. 20).

The second type of event layers, EL2, are similarly characterized by erosively based, ≤ 4 cm thick layers of medium-grained basaltic sand and interspersed organic material that fine upward into homogenous dark brown to dark gray silt. Most of the preserved EL2 layers are only composed of the sandy base and silt layers, however a small portion of EL2 layers are overlain by ≤ 4 cm thick light brown silty clay (Fig. 24). Grain size (15-55 μm) and magnetic susceptibility profiles (100-400 SI) of EL2 layers show a gradual decrease upward; however the decrease in magnetic susceptibility values is not as pronounced as observed from the EL1 deposits (Fig. 19). The EL2 layers range in thickness from 4 to 33 cm (Pollen, 2016). EL2 deposit thicknesses follow a pattern similar to EL1 deposits in that they are thicker in the deep-water basins and thinner in cores recovered from shallow depths.

3.3 Geochronology and Stratigraphy

The oldest recovered sedimentary record reaches back to $\sim 8,500$ cal years BP in core 4A-1K. This core contains the 7,478-7,620 cal yr BP Mazama tephra, a regional chronostratigraphic marker layer (Hallet et al. 1997). Bacon age models based on radiocarbon dated organic material indicate that the event-free sedimentation rate is 0.79 mm/yr (core 4A-1K) in the shallow portion of the south basin whereas the rates in the deep portions of the south basin are between 0.66 mm/yr (core 5A-1K) and 0.84 mm/yr (core 6A-1K) (Pollen, 2016). The event-free sedimentation rate of the north basin is 0.79 mm/yr (core 7C-1K) (Pollen, 2016). Correlation of all layers is based upon stratigraphically consistent radiocarbon dated material extracted from cores (Table 8; see Pollen, 2016 for full table).

There are four EL1 layers present in Lake Crescent's sedimentary record. The first EL1-A layer, has an estimated median age of 2,859 (2,785-2,943) cal yr BP (Table 8). This age was obtained from wood and bark fragments present in the base of the deposit in core 9A-1K. The calibrated age of EL1-A is widely correlated by radiocarbon dated organic material throughout both basins in cores 7C-1K, 2C-1K, 9A-1K, and 6A-1K. The thickness of the EL1-A layer ranges from 22 cm (core 4A-1K) to 230 cm (core 7C-1K) (Fig. 20). The entire layer is recovered in cores 4A-1K, 6A-1K, 7C-1K, 2C-1K, 2A-1K, 8A-1K, and 9A-1K. Core 5A-1K retrieved most of EL1-A due to the presence of basaltic sand at the end of the core but it did not capture the transition to underlying background sediments. The basal unit of EL1-A shows a highly irregular scour surface into the underlying sediment. The estimates of volume, spatial distribution, sand source petrology, and sediment transport calculations herein reported are for EL1-A, the most data rich event layer from the Lake Crescent record.

Woody sticks at the base of EL1-B in core 9A-1K gave an age of 4,015 (3,921-4,088) cal yr BP. This layer is present in cores 4A-1K, 8A-1K, and 9A-1K; however it is not as prominent in comparison to the other EL1 layers (Fig. 21). The thickness of EL1-B ranges from 11 cm (core 4A-1K) to 20 cm (9A-1K). The EL1-B layer in core 4A-1K is separated from the EL1-A layer by 32 cm of background sediment whereas in core 8A-1K, the two are separated by 20 cm. The EL1-B layer in core 9A-1K unconformably underlies the EL1-A layer.

EL1-C is dated at 5,753 (5,619-5,902) cal yr BP in core 3C-1K and 5,736 (5,656-5,889) cal yr BP in core 8A-1K (Fig. 22). EL1-C can be traced through all of the north basin

cores with an average thickness of 174 cm and is present in core 4A-1K, at the far western end of the lake with a thickness of 3 cm. The basal unit of EL1-C contains prominent erosional scour surfaces into the underlying sediment.

Plant fragments from the top of EL1-D in core 2C-1K returned an age of 7,097 (7,006-7,242) cal yr BP. EL1-D is partly present in core 2C-1K and is recovered entirely in core 4A-1K with a thickness of 12 cm (Fig. 23).

EL2 deposits are found in all cores interspersed between background sediments and other event deposits (Fig. 24). EL2 deposits are concentrated in quantity and thickness in the south basin. Core 4A-1K contains 16 EL2 deposits with an average thickness of ~4 cm (Pollen, 2016). South basin cores (5A-1K and 6A-1K) contain 10 and 11 EL2 deposits, respectively, with a maximum thickness of 33 cm thick, while in the north basin between 3 and 10 EL2 deposits were recovered from individual cores and these have a maximum thickness of 12 cm (Pollen, 2016). Cores 1A-1K, 1B-1K, and 10A-1K, all located atop subaqueous rock slide deposits, contain three EL2 deposits that are between 2 and 6 cm thick.

3.4 Sand Petrology

The petrology of turbidite sand layers recovered from the piston cores were investigated in order to determine if these sediments were derived from a single source (e.g., Barnes Creek delta) or multiple sources. Petrologic counting of the sands retrieved from eight streams feeding into the lake and from the piston cores were categorized into 16 parameters, which were subsequently reduced to four parameters: quartz, feldspar, sedimentary fragments, and volcanic fragments and minerals (Table 9; Table 10). Twenty-four thin

sections prepared from core-extracted sands had sufficient grains to count. Sand from the four EL1 layers and sand from multiple EL2 layers was used for the petrologic study.

For the volcanic parameter, igneous fragments (mostly basalt) were the dominant lithology, followed by mica, pyroxene, opaque minerals, volcanic glass, and amphibole. The igneous fragments were characterized by a porphyritic texture and phenocrysts of pyroxene and plagioclase. The sedimentary fragments commonly consist of siltstone which was characterized by sub-rounded to angular quartz grains supported by a fine-grained matrix. The quartz generally occurs as polycrystalline grains although minor amounts of monocrystalline quartz were observed. Potassium feldspar is the dominant feldspar mineral type, with a few twinned plagioclase feldspars interspersed.

3.4.1 Stream Sand

In a clockwise direction around the lake, sand was collected from near the mouths of Barnes, West Barnes, Smith, Aurora, Lapoel, Eagle, Fairholm, and Piedmont Creeks (Fig 25; Table 10). These eight perennial streams function as end member compositions for the sands of EL1 and EL2 layers. Streams that drain through the Blue Mountain Unit (Aurora, Eagle, Fairholm, Lapoel, Smith, and West Barnes) contain sand that is dominated by sedimentary fragments (average = 78%). Barnes Creek sands are dominated (96%) by volcanic fragments and minerals derived from rocks of the Crescent Formation. The sand of Piedmont Creek is dominated by quartz (52%) and sedimentary fragments (28%).

3.4.2 Event Layer 1 Sand

Sand recovered from EL1 is composed primarily of volcanic fragments and minerals (76%) and lesser amounts of sedimentary fragments (15%), quartz (5%), and feldspar (4%) (Fig. 26; Table 10). Although the EL1-A sand is dominated by volcanic components, the thin section from core 6A-1K contains 25% sedimentary fragments.

3.4.3 Event Layer 2 Sand

Sand from EL2 layers separate into two groups: volcanically dominated, or a mixture of sedimentary and volcanic lithics (Fig. 27; Table 10). Thin sections from core segments 4A-1K-2, 6A-1K-3, and 9A-1K-1 contain mostly volcanic fragments (85%). Thin sections from cores 6A-1K-1 and 6A-1K-2 contain relatively equal proportions of sedimentary (46%) and volcanic (38%) grains.

3.5 Event Layer 1-A Sediment Transport Dynamics

The grain size (median and 90th percentile) of the silt particles in the homogenous silt layer and coarsest particles from the EL1-A basal sand in cores 2C-1K, 6A-1K, 7C-1K, and 8A-1K were used to calculate boundary shear stress (τ_b) of the emplacing flows (Table 11). The boundary shear stress calculated for the particles represents the shear stress required to move the particles as suspended load.

The boundary shear stress estimated from the particles from the homogenous silt layer are $D_{50} = 1.1 \times 10^{-3} \text{ g/cm}^3 \cdot \text{s}^2$ and $D_{90} = 0.2 \text{ g/cm}^3 \cdot \text{s}^2$. The boundary shear stresses estimated from the coarsest particles of the EL1-A basal sand are greatest from cores in the north basin where values of ($D_{50} = 551 \text{ g/cm}^3 \cdot \text{s}^2$ and $D_{90} = 2969 \text{ g/cm}^3 \cdot \text{s}^2$) were calculated from core 7C-1K sediments. The values ($D_{50} = 137 \text{ g/cm}^3 \cdot \text{s}^2$ and $D_{90} = 946 \text{ g/cm}^3 \cdot \text{s}^2$) decrease

at core 8A-1K. Core 2C-1K has the lowest estimated boundary shear stress values ($D_{50} = 58$ g/cm*s² and $D_{90} = 273$ g/cm*s²) of the north basin. The two lowest estimated boundary shear stress values are from sediments recovered from the south basin at core 6A-1K ($D_{50} = 33$ g/cm*s² and $D_{90} = 445$ g/cm*s²) and core 4A-1K ($D_{50} = 2.1 \times 10^{-3}$ g/cm*s² and $D_{90} = 0.6$ g/cm*s²).

3.6 Event Layer 1-A Distribution and Volume

The sediment thickness and geographical distribution of EL1-A can be traced on the seismic reflection profiles. Some seismic profiles had resolution that were too low to allow for accurate tracing of the layer thicknesses along all tracklines; therefore the spatial extent of the interpolated Chirp data only covers 9.84×10^6 m², roughly half of the lake. It is important to note that the seismically transparent portion of the layer (silty homogenous layer) was the part that was traced, (e.g., the volume estimate excludes the sand and clay portion of the EL1-A deposit). For the reasons listed above, the volume and mass is a minimum estimate. The total wet volume of the EL1-A deposit is $4.79 \pm 1.58 \times 10^6$ m³ (Fig. 28a,b; Fig 29; Table 12). The total dry volume is $2.87 \times 10^6 \pm 0.94 \times 10^6$ m³, and its equivalent dry sediment mass is $5.75 \times 10^6 \pm 1.89 \times 10^6$ T.

Interpolated sediment thickness values range from 0 to 2 m. The main sediment depocenters are in the middle of the north and south basins with maximum thickness values of 2 m and 1.6 m, respectively. A small, isolated depocenter with a maximum thickness value of 0.7 m is located in the west portion of the south basin (core 4A-1K). EL1-A is not present between the two basins where the subaqueous rock slide deposits are located (Fig. 28a,b; Fig. 29). Interpolated thickness profiles from the Chirp imagery show the general concave upward

shape where the sediment accumulation is thickest in the middle of the basins, thinning toward the margins (Fig. 30; Fig. 31). The deposit thickness generally decreases to the east in the north basin and to the west in the south basin. The EL1-A deposit covers the entire “abyssal” plains of both the north and south basins between the steep lake margins in the north-south direction.

3.7 Sledgehammer Point Rockslide

The entire Sledgehammer Point rockslide is estimated to be $11.93 \times 10^6 \text{ m}^3$ using the landslide area-to-volume scaling relationship of Larsen et al. (2010). The subaqueous portion of the Sledgehammer Point rockslide is estimated to be $7.19 \times 10^6 \text{ m}^3$ (Fig. 36).

3.8 Displacement Wave Heights

Displacement wave heights are estimated at four locations herein named the “Log Cabin Resort Scenario”, “Opposite Shore Scenario”, “Nature Bridge Scenario”, and the “U.S. Highway 101 Scenario” (Table 13). The wave at the Log Cabin Resort is estimated to be $5 \pm 1.5 \text{ m}$ about 243 m offshore. The wave at the opposite shore is estimated to be $20 \pm 6 \text{ m}$ about 139 m offshore. The wave at Nature Bridge is estimated to be $11.5 \pm 3.5 \text{ m}$ about 201 m offshore. The wave at U.S. Highway 101 is estimated to be $3 \pm 1 \text{ m}$ about 333 m offshore (Fig. 32).

4.0 DISCUSSION

4.1 Megaturbidites

Despite ambiguity amongst mass movement terminology in lacustrine paleoseismic studies of the last few decades, deposits such as the EL1 layers found in Lake Crescent are best considered megaturbidites based upon the definition set forth by Bouma (1987). Earlier lacustrine paleoseismic studies have termed similar deposits as “seismoturbidite” (Nakajima and Kanai, 2000), “seiche deposits” (Siegenthaler et al. 1987), and “homogenite” (Siegenthaler et al. 1987; Chapron et al. 1999); however, recent studies have adapted the widely accepted and more general term “megaturbidite” (Bouma, 1987; Schnellmann et al. 2005; Fanetti et al. 2008; Hilbe and Anselmetti, 2014; Moernaut et al. 2014). Bouma (1987) defines megaturbidites by six key characteristics: 1) exceptional thickness compared to other event layers in a particular sedimentary sequence, 2) lateral extensiveness, 3) compositional difference from the background sediment or host rock, 4) depositional geometry not typical of submarine (sublacustrine) fans, 5) internal properties that suggest they are the deposit of one single transport event, and 6) containing features that make them good markers for stratigraphic and seismic correlations. The term “mega” refers to the thickness difference as compared to other turbidites generated in the same setting. Consequently, megaturbidites do not have a specific thickness threshold to exceed for classification as such, rather the determination as to whether an event layer is a turbidite or megaturbidite is dependent upon relative differences within a sedimentary sequence from a particular setting or location (e.g., Lake Crescent).

Megaturbidites from Lake Crescent are characterized by their seismic reflection profile signature and correspondence to specific lithologies present in the sediment cores. The acoustically chaotic-to-transparent units with highly reflective bases (*Seismic Facies B*) is directly correlative to the massive silt layer, or “homogenite” (Siegenthaler et al. 1987), with the normally graded sandy base and overlying clay cap. These unique turbidites have a special geometry across the depositional basin that follows a ponded, concave upward 2-dimensional shape in cross section across the deep basins in which they are present. The thickness and seismic visibility of the megaturbidites increases as a function of water depth such that they are almost impossible to differentiate from other layers in the seismic reflection profiles towards the lake margins and in shallow basins. The presence of megaturbidites at shallow depths is only accurately evidenced by sediment cores. Seismic images of the basin subsurface demonstrate the exceptional volume and extensiveness of the megaturbidites. The correlation of *Seismic Facies B* units via seismic reflection profiles and by radiocarbon dating within the basins of Lake Crescent suggests that the megaturbidites do not have localized origins but instead owe their existence to a single event that affected the entire lake. Though they share a common name and general lithological sequence, the turbidites (EL2 deposits) found in Lake Crescent are quite different from the megaturbidites. The non-mega turbidites are only at most several tens of cm thick, and occupy significantly less depositional area and volume of sediment. Most of the EL2 deposits lack a clay cap and interstratified basalt and chlorite laminations at the top. The turbidites are interpreted to represent less severe earthquake ground shaking events that occurred within the Lake

Crescent catchment in comparison to the events that sourced the megaturbidites (Pollen, 2016).

Megaturbidites are formed from the remobilization of large amounts of material during a subaerial or subaqueous mass wasting event. The transport of material is due to subaqueous sediment density flows termed turbidity currents that occur adjacent to the lake floor (Schnellman, 2002; Hilbe and Anselmetti, 2014; Talling, 2014; Van Daele et al. 2015). Turbidity currents put particles from the lake floor into suspension, possibly from a process that separates suspended particles transported as concentrated density flows from a plastically deforming mass (Mulder and Alexander, 2001; Haughton et al. 2009; Hilbe and Anselmetti, 2014). The thick homogenous layer of the megaturbidite is interpreted to be reworked sediment that was diffused upward into the water column and kept in suspension by periodic oscillations (seiches) that result in the symmetrical thickness distribution, ponded geometry, and repeated (multiple) grading observed at the base of such deposits (Schnellmann et al. 2002; Beck, 2009; Howarth et al 2012; Hilbe and Anselmetti, 2014). The seiche effect increases segregation of the fine-grained sediment fraction and sustains suspension that creates the observable separation of the lithological units (Schnellman et al. 2006; Beck, 2009; Howarth et al. 2012). The duration of fine-sediment suspension can extend for days or even weeks before deposition (e.g., Cita and Aloisi, 2000; Mulder et al. 2009; McHugh et al. 2011).

Van Daele et al. (2015) describe megaturbidites from Chilean lakes attributed to the 1960 M_w 9.5 Valdivia great subduction zone earthquake similar in thickness, extent, and lithology to those observed in Lake Crescent. The Chilean megaturbidites consist of coarse-

grained bases overlain by massive homogenous mud and a fine-grained clay cap. The meter-scale deposits were found in the depositional areas of four lake basins where onshore landslides entered the water, creating a displacement wave and subsequent seiche as reported by eyewitnesses (Van Daele et al. 2015). Additional Chilean lakes experienced large displacement waves but no seiches. In such instances megaturbidites were not present in the sedimentary record (Van Daele et al. 2015). It is also important to note that a megaturbidite was generated in a lake where no onshore landslides occurred (Van Daele et al. 2015). Seismic profiles of this lake suggest that its megaturbidite was generated by a subaqueous mass wasting event. Consequently, it appears that megaturbidites will not be formed unless an oscillatory movement in the water column occurs (Chapron et al. 1999; Cita and Aloisi, 2000; Beck, 2009; Schnellman et al. 2006; Hilbe and Anselmetti, 2014; Van Daele et al. 2015).

Lacustrine megaturbidites have been used to extend the historical record of earthquakes back in time several thousands of years in lakes of seismically active regions, including at Lake Paringa, New Zealand (Howarth et al. 2012), Lake Le Bourget, France (Chapron et al. 1999), Lake Lucerne, Switzerland (Schnellmann et al. 2005; Hilbe and Anselmetti, 2014), Lake Como, Italy (Fanetti et al. 2008), Lake Biwa, Japan (Inouchi et al. 1996), and lakes in south-central Chile (Moernaut et al. 2014; Van Daele et al. 2015). Simultaneous sediment remobilizations that can be correlated in sub-basins of a single lake, or between nearby lakes is a critical paleoseismic tool used to infer earthquake origin (Schnellmann, 2002; Hilbe and Anselmetti, 2014; Talling, 2014; Van Daele et al. 2015). Precise age control on megaturbidites in sub-basins is necessary to deduce synchronous

emplacement (Talling, 2014). The subaqueous remobilization of large sediment volumes can occur from multiple casual mechanisms including the dissociation of gas and delta slope failure from normal sediment accumulation; therefore the existence of a megaturbidite in and of itself is not solely an indicator of paleoseismic activity (Girardclos et al. 2007; Talling, 2014). In the event that an earthquake origin is established for a megaturbidite, its spatial extent and thickness may be useful as a proxy of local seismic intensity (e.g., Moernaut et al. 2014; Van Daele et al. 2015). The large volume, broad extent, and synchronous emplacement of the megaturbidites in both of the deep basins of Lake Crescent is corroborated by radiocarbon analysis from multiple cores and indicates that the deposits are most likely of seismic origin.

Moernaut et al. (2014) and Van Daele et al. (2015) developed an earthquake-recording threshold (EQRT) from extensive studies of Holocene sediments from a suite of Chilean lakes. The EQRT is dependent upon the regional geology, climate, slope gradient, lacustrine sediment properties, and geomorphology and vegetation of the catchment. The EQRT of a lake can be quite equivocal, often varying between sub-basins, depositional areas, and coring sites. In the Chilean lake studies from which the EQRT was developed, megaturbidites were found to occur when regional seismic intensity was \geq VII 1/2 , while smaller seismically-induced turbidites in the same lakes had an EQRT of seismic intensity \geq V 3/4 (Van Daele et al. 2015).

4.2 Lake Crescent Megaturbidites

The four meter-scale megaturbidites recovered from the c. 8,000 year sedimentary record from Lake Crescent are characterized by sharply based, normally graded basaltic sand layers overlain by a thick, homogenous brown silt layer that in turn is capped by light brown clay and chloritic and basaltic laminations (Fig. 20). The Lake Crescent megaturbidites are correlated to an acoustically transparent and ponded seismic facies (Fig. 34; Fig. 35). The layers can be traced across the north and south basins from seismic and core stratigraphic records, suggesting that they are not localized features. The median depositional age of the Lake Crescent megaturbidites are 2,859 (2,785-2,943), 4,015 (3,921-4,088), 5,736 (5,656-5,889), and 7,097 (7,006-7,242) cal yr BP for EL1-A through EL1-D, respectively (Table 6; Pollen, 2016). The erosive bases of the megaturbidites indicates that the dated organic material was likely remobilized during emplacement; therefore the dated material may be decades to centuries older than the actual event (Gavin, 2001; Pollen, 2016). The youngest reported date for a given megaturbidite layer is used as the maximum event age (Pollen, 2016).

Petrologic analysis of basal sands from Lake Crescent megaturbidites indicates that the sediment was derived from sources along the lake margin rather than a single point source. Sands from each megaturbidite layer generally returned the same volcanically-dominated signature that did not reflect the end-member sand composition of any one stream sand. The presence of the chloritic and basaltic laminations at the tops of megaturbidites makes the sedimentological feature explicitly linked to the event that generated the megaturbidites (Fig. 33). The consistent deposition of the interstratified laminations at the top

of the megaturbidites is interpreted as recording patterns of post-seismic geomorphic landscape response following a rockslide-displacement wave event. They are interpreted to be the mobilization of sediment from the subaerial portion of the exposed rockslide scarp or from exposed rock and soils below the displacement wave trim line during subsequent precipitation events in the years after the initial mass wasting event (Dadson et al. 2004; Howarth et al. 2012).

EL1-A is the most recent megaturbidite present in the sedimentary record of Lake Crescent, and therefore it preserves the greatest amount of information concerning its origin and effects. Radiocarbon dated organic material extracted from cores brackets the maximum median age of megaturbidite EL1-A as 2,859 (2,785-2,943) cal yr BP (Table 6; Pollen, 2016). It is present in cores 4A-1K, 5A-1K, 6A-1K, 2C-1K, 2A-1K, 7C-1K, 8A-1K, and 9A-1K. The average thickness of the megaturbidite layer found in deep basin cores is ~173 cm; however, it thins to 22 cm (4A-1K) and 28 cm (9A-1K) towards the margins of the lake. It is thickest in core 7C-1K at 230 cm. This typical megaturbidite lithological sequence is seen in every core with the exception of 9A-1K, which lacks the chloritic and basaltic laminations in the clay cap (Fig. 20).

EL1-A has the largest aerial distribution and volume in the south basin and it is thickest in the north basin. It is thickest in the deepest portions of both basins and thins towards the margins. The extensiveness of the deposit is controlled by the size of the basin; however the thickness is interpreted to be controlled by proximity to the source area. The isopach map and 3D sediment thickness distribution map of EL1-A (Fig. 28a; Fig. 29) both highlight the influence that the glacial sill in the west portion of the south basin has had on

the megaturbidites distribution, across which the thickness decreases dramatically. The maximum interpolated thickness of the EL1-A deposit is 2 m in the north basin and 1.6 m in the south basin. The wet volume of EL1-A is minimally estimated to be $4.79 \times 10^6 \text{ m}^3$.

The seismic profiles of the lake subsurface demonstrate that the emplacement of the thick, extensive megaturbidites controls the stratigraphy of the lake. This observation is further evidenced by comparing the annual amount of normal sedimentation to the amount of material reworked in the EL1-A event. The dry volume of annual normal sedimentation (4664 m^3) can be calculated using the event-free sedimentation rate to compare to the dry volume of an event layer ($2.87 \times 10^6 \text{ m}^3$) (Appendix G). The amount of sediment reworked in megaturbidite EL1-A is equivalent to c. 615 years of normal, non-event sediment accumulation within Lake Crescent.

Prior to deposition, all of the stratigraphic components of megaturbidite EL1-A moved as suspended load. Differences in the boundary shear stresses estimated to have moved the EL1 sand at each core site as suspended load are attributed to the strength of the turbidity current as it passed each site and thus can serve as a proxy for proximity to the source. The high boundary shear stress values ($D_{50} = 551 \text{ g/cm} \cdot \text{s}^2$ and $D_{90} = 2969 \text{ g/cm} \cdot \text{s}^2$) estimated for the transport of the coarsest basal sand of core 7C-1K indicates the strongest flow in that area. The boundary shear stress values ($D_{50} = 137 \text{ g/cm} \cdot \text{s}^2$ and $D_{90} = 946 \text{ g/cm} \cdot \text{s}^2$) estimated for the transport of the coarsest basal sand of core 8A-1K indicates that the strength of the flow decreased as it moved eastward in the north basin. The strength of the flow lessened in the northward direction at core 2C-1K from 7C-1K sites, where the boundary shear stress values decreased significantly ($D_{50} = 58 \text{ g/cm} \cdot \text{s}^2$ and $D_{90} = 273$

g/cm*s²). The flow was weakest over the core 6A-1K and 4A-1K sites, located in the central and western portions of the south basin, where boundary shear stress values ($D_{50} = 33$ g/cm*s² and $D_{90} = 445$ g/cm*s²; $D_{50} = 2.1 \times 10^{-3}$ g/cm*s² and $D_{90} = 0.6$ g/cm*s²) were dramatically lower in comparison to the core locations in the north basin.

The smaller particles in the homogenous silt layer of the EL1-A megaturbidite require low boundary shear stress values to move as suspended load ($D_{50} = 1.1 \times 10^{-3}$ g/cm*s² and $D_{90} = 0.2$ g/cm*s²). At core 7C-1K, shear stress would have to increase eight orders of magnitude (500,000 times greater) in order to move the coarsest sand in suspension versus the particles in the homogenous silt layer. In contrast, the shear stress would have to increase only seven orders of magnitude (30,000 times greater) to move the coarsest sand in core 6A-1K versus the particles in the homogenous silt layer.

The absence of EL1-B from cores that recovered EL1-C and EL1-D in addition to prominent scour surfaces visible below EL1-A in cores and seismic reflection profiles indicates that the emplacement of EL1-A was especially erosive (Fig. 34; Fig. 35). The basal reflector of the top-most thick transparent seismic unit from the north basin is observed to truncate the underlying “background” sediment, leaving behind only a very thin existing package of such sediment between the next older megaturbidite deposits (Fig. 34). In contrast, the basal reflector of the transparent unit for EL1-A in the south basin is less irregular and a thicker package of background sediment is present between EL1-A and the underlying EL1-B layer (Fig. 35).

The greater thickness, higher estimated shear stress values, and significant basal scour erosion resulting from down-slope transport and emplacement of the megaturbidite EL1-A

indicates that a stronger turbidity current was present in Lake Crescent's north basin during the c. 3,000 yr BP event than in the south basin. These sedimentologic differences are interpreted to result from the closer proximity of the core sites in the north basin relative to the source of megaturbidite EL1-A, relative to core locations from the south basin (Fig. 8). A scenario similar to the aforementioned Chilean lakes whose megaturbidites were sourced by landslides entering the lake is hypothesized for the EL1-A layer at Lake Crescent. The Sledgehammer Point rockslide initiated 700 m above the lake and descended into water that is estimated to have been 100 ± 40 m deep. The slide occurred within the Crescent Formation on the east margin of the channel and entered the lake along the passage connecting both lake basins (Fig. 36). The subaqueous volume is estimated to be $7.19 \pm 1.79 \times 10^6 \text{ m}^3$.

Upon entering the lake, the Sledgehammer Point rockslide triggered a displacement wave. As the wave train travelled through the lake, it likely remobilized sand from shallow subaqueous environments where it was transported as a concentrated density flow along the bottom and in the process, eroded significant amounts of the existing lake floor and suspended those particles up into water column. After the initial wave, the deep, confined nature of the basins likely induced the seiche effect thus keeping the particles in suspension (Schnellmann et al. 2002; Beck, 2009; Howarth et al 2012; Hilbe and Anselmetti, 2014). The periodic oscillations of a seiche resulted in the massive, homogenous silt layer, symmetrical thickness distribution, ponded geometry, and repeated (multiple) grading observed at the base of the megaturbidite (Schnellmann et al. 2002; Beck, 2009; Howarth et al 2012; Hilbe and Anselmetti, 2014). Days to weeks after the rockslide-displacement wave event, the fine-grained "reworked" sediment would have settled to the lake floor as a function of its density,

thus creating the stratified lithological sequence of megaturbidite EL1-A (Cita and Aloisi, 2000; Schnellman et al. 2006; Beck, 2009; Mulder et al. 2009; McHugh et al. 2011; Howarth et al. 2012).

Although numerical simulations of displacement wave heights and run up are needed to best quantify potential inundation, the application of an empirically derived equation can be implemented to estimate wave heights at specific propagation distances and angles subsequent to entry of the Sledgehammer Point rockslide into Lake Crescent. The wave height at each location scenario is limited to 100 to 300 meters offshore (e.g., just before the steep-sided lake margin begins). The opposite shore wave height is highest (20 m) then it decreases by almost half at Nature Bridge (11.5 m). It decreases by half again at the Log Cabin Resort (5 m) and decreases by roughly half once again at the U.S. Highway 101 location (3 m). Using a run up wave height scaling power law relationship defined as $h = 0.0314v^{0.5}$ derived from landslide volume-to-maximum wave run up of historic events, the Sledgehammer Point rockslide would produce an estimated maximum displacement wave run up height of 86 ± 20 m on the opposite shore (Fig. 37; Fig. 38; Table 14). The wave inundation likely scoured tens of meters of vegetation, soil, and rock from the shorelines at even the furthest points from where the slide entered the lake. Seismic profiles demonstrate the causal relationship of the slide and the megaturbidite where tens of meters of topographic relief are visible with no megaturbidite present within the intra-deposit depressions. There is only approximately 2 m of background sediments in the depressions which correlates to the thickness of sediments present above the megaturbidite layer in the north basin (Fig. 14).

Therefore, it is likely that the most recent megaturbidite was deposited almost simultaneously with the rock slide.

Megaturbidite EL1-B is dated at 4,015 (3,921-4,088) cal yr BP and is only present in cores 4A-1K, 8A-1K, and 9A-1K with partially preserved thicknesses of 8, 10, and 25 cm (Fig. 21). The sediment cores recovered from the lake's south basin did not penetrate deep enough to recover EL1-B. The emplacement of EL1-A eroded most of the deposit from the sedimentary record of the north basin. We correlate megaturbidite EL1-B with the Lake Sutherland rockslide complex which is maximally estimated by Pringle et al. (2010) to have occurred around $4,340 \pm 50$ years ago by radiocarbon dated growth rings in a drowned tree at the west end of Lake Crescent's south basin. EL1-B is found in core 9A-1K atop distinctive landslide debris such as pebbles, gravel, and interspersed organic material attributed to the Lake Sutherland slide complex. The Lake Sutherland rock slide is at least partly responsible for the damming of ancestral Lake Crescent, the subsequent 25 m lake level rise, and drainage outlet alteration to the Lyre River (Fig. 3; Fig. 5).

Megaturbidite EL1-C, the second most prominent deposit, is dated at 5,736 (5,656-5,889) cal yr BP. This megaturbidite ranges in thickness from 3 cm in core 4A-1K to ~174 cm in the north basin deep cores (Fig. 22). The Mount Storm King rockslide, located across from the Lake Sutherland rock slide, is a potential source of megaturbidite EL1-C. The Mount Storm King rockslide is minimally dated at 5,180 (4,976-5,287) cal yr BP and is the other part of the coalescing rockslide pair responsible for damming ancestral Lake Crescent. Charcoal collected from sediments that accumulated within the closed depression on the surface of the rockslide provides a minimum age constraint. It is likely that the rockslide

event predates the charcoal age thus making it eligible as the source that triggered the megaturbidite EL1-C, which is approximately 600 years older.

The oldest megaturbidite recovered from the 2015 Kullenberg coring efforts, EL1-D, is dated at 7,097 (7,006-7,242) cal yr BP. It is partially observed in cores 2C-1K and 2A-1K where the upper portion of its massive silt unit and clay cap interstratified with laminations comprised of chlorite and basalt are present (Fig. 23). The entire deposit is found in core 4A-1K from the west end of the south basin, where it is 12 cm thick. The evidence that previous megaturbidites were sourced by rockslides occurring on the shores of the lake indicates that the same process likely formed megaturbidite EL1-D. Nevertheless the rockslide source of EL1-D is unclear; there are several other rockslides around Lake Crescent that could have sourced the deposit. The absence of minimum age constraints for them makes it challenging to isolate a likely source at this time.

Subaerial mass wasting events are most likely the source of the Lake Crescent megaturbidites; however, it is worthwhile to consider other sources that could have formed the deposits. One mechanism that could create a displacement wave and seiche is vertical lake floor displacement related to fault motion. The displacement could generate a wave that destabilizes sediment along the shorelines and that is transported along the bottom, eroding and suspending sediment into the water column as it travels throughout the lake as a fast moving turbidity current. The seiche effect induced by the propagation of the displacement wave in the enclosed basins would keep the suspended material in suspension, thus resulting in the stratified megaturbidite lithological sequence as the material settles to the lake bottom.

Several studies have documented and modelled lake-floor displacement generating displacement waves. Ichinose and Anderson (2000) investigated the potential displacement and seiche waves generated by $M_w \sim 7.0$ earthquakes in Lake Tahoe, California-Nevada by modelling the 4 m displacement of several normal faults that run beneath the lake. The amplitudes of modeled displacement waves generated by fault offset of the lake-floor ranged from 3 to 10 m and were followed by a seiche. In 1872, a magnitude 7.5-7.7 earthquake occurred along the Owens Valley fault, which runs below Owens Lake, California (Smoot et al. 2000). The ~1 m vertical offset of the lake floor across the fault generated a displacement wave that was witnessed by local inhabitants and was further evidenced by an unusual pebbly sand layer in the sedimentary record (Smoot et al. 2000). Smoot et al. (2000) determined the minimum size of a wave necessary to move the largest grain sizes observed in the pebbly sand layer to be nearly 5 m high in water 6 m deep, which aligned consistently with the eyewitness accounts. The 1 m displacement of the lake floor by the Owens Valley fault did not create a seiche.

Theoretical applications of the abovementioned studies cannot be applied to Lake Crescent due to the limitations of this study. Offset of the megaturbidite layers in the north basin show that displacement along the Lake Creek-Boundary Creek fault beneath the lake floor is about 1 m. It is possible that a small wave could be triggered from the lake floor displacement but it would most likely not be enough displacement to create a wave and seiche. This hypothesis needs to be further tested by numerical modelling of lake-floor displacement waves because each lake will have a unique response to various amounts of displacement. Consequently the fault-lake floor offset source-type model cannot be

confidently ruled out as a megaturbidite trigger until proven otherwise. However, this lake-floor displacement scenario does not account for the chloritic and basaltic laminations that overlie the clay cap, which are interpreted to be the mobilization of sediment from exposed rockslide scarps in Eocene Crescent formation submarine basalts during precipitation events after a rockslide-displacement wave event.

Subaqueous mass wasting events have generated displacement waves and megaturbidites in lakes such as Lake Lucerne, Switzerland (Hilbe and Ansellmetti, 2014) and Lake Geneva, France-Switzerland (Kremer et al. 2015) but they are considered an even less likely source for the Lake Crescent megaturbidites. Small slump layers are visible in some cores (Pollen, 2016); however, the high resolution bathymetry and seismic reflection profiles show no large-scale subaqueous mass wasting features.

4.3 Earthquake Origins

Lake Crescent is situated in the forearc of the Cascadia subduction zone, an area known for potentially damaging earthquakes. Recent studies have provided evidence that the subduction zone is capable of generating magnitude 9 earthquakes every 300-500 years (Atwater, 1987; Atwater and Hemphill-Haley, 1997; Goldfinger et al. 2012). The U.S. Geological Society created a Shakemap scenario that suggests Lake Crescent would experience ground shaking of intensity VI-VII (strong-to-very strong) if a M_w 9.0 earthquake occurred along the Cascadia margin (USGS, 2016). Turbidite records from Saanich Inlet, Effingham Inlet, and the Cascadia Margin were compared to the megaturbidites in Lake Crescent to see if they could be correlated to the prehistoric ruptures of the subduction zone interface (Fig. 1; Pollen, 2016). Megaturbidites EL1-B and EL1-D were the only deposits

correlated with one or more turbidites in those locations that were attributed to ruptures of the Cascadia megathrust; therefore, it is possible that those two megaturbidites were formed by great subduction earthquakes (Pollen, 2016). Conversely, the absence of an event to correlate with EL1-A and EL1-C indicates that the megaturbidites need not be explicitly attributed to great subduction zone earthquakes. Subduction zone events of magnitude > 8.6 have the potential to trigger closely timed magnitude > 6.5 earthquakes on upper crustal faults in the region (Gomberg and Sherrod, 2014). This relationship can possibly explain the overlap of EL1-B and EL1-D with correlated regional turbidite records due to triggering of the Lake Creek-Boundary Creek fault in the months after a great subduction zone earthquake. Other sources of earthquakes include regional upper crustal faults, such as the Seattle Fault, which would produce ground shaking of intensity V (moderate) at the distance of Lake Crescent if it were to generate a M_w 7.2 earthquake (USGS, 2016). It is possible that ground shaking from megathrust events or regional upper crustal faults could surpass Lake Crescent's EQRT and trigger a rock slide into the lake that would result in the deposition of a megaturbidite.

Though the above sources of earthquakes cannot be discounted as events that have resulted in sedimentary imprints in the subsurface of Lake Crescent, it is probable that the megaturbidites are a result of rupture along the Lake Creek-Boundary Creek and Sadie Creek faults that also triggered rockslides from the steep slopes above the lake. As previously mentioned, the Lake Creek-Boundary Creek fault is an east-west trending north-dipping oblique right-lateral thrust fault that runs directly beneath Lake Crescent's north basin (Brown et al. 1960; Tabor and Cady, 1978a,b; Schasse, 2003; Polenz et al. 2004; Schasse et

al. 2004, Nelson et al. 2007; Fig. 3). Rupture of the eastern portion of the Lake Creek-Boundary Creek fault resulting in a M_w 6.8 earthquake would produce ground shaking of intensity VIII to X+ (severe to extreme) surrounding Lake Crescent (USGS, 2016). Polenz et al. (2004) and Schasse et al. (2004) reported the first evidence for post-glacial ground rupture of the Lake Creek Boundary Creek fault south and east of Port Angeles. Trenching studies of the sites identified by Polenz and Schasse by the U.S. Geological Survey found evidence for two or three post-glacial surface rupturing earthquakes along the fault east of the Elwha River (south to southeast of Port Angeles) (Nelson et al. 2007). Evidence for rupture west of the Elwha River was not available until recent lidar mapping by the Washington State Department of Natural Resources and our seismic reflection profiles showed prominent fault scarps and sediment deformation along the trace of the Lake Creek-Boundary Creek and Sadie Creek faults (Fig. 4). The Lake Crescent seismic reflection data clearly demonstrate that the most recent megaturbidite (EL1-A) overlies progressively deformed packages of sediment, indicating that movement along the fault and the emplacement of the megaturbidites are related (Fig. 10; Fig. 11). These seismic data reveal that there are a minimum of four progressively deformed packages of sediment occurring beneath the north basin of Lake Crescent. Thus, the ages of the megaturbidites, which are separated by ~1,100-1,700 year intervals, can provide a recurrence interval of earthquakes on the western segment of the Lake Creek-Boundary Creek fault.

4.4 Seismic Hazards

The presence of at least four megaturbidites in the sedimentary record from Lake Crescent indicates that repeated disastrous events have occurred in the past 8,500 years with the most recent dating to 2,859 (2,785-2,943) cal yr BP; consequently the lake is possibly overdue for another devastating event, if these events are related to the Lake Creek Boundary Creek fault and its slip behavior is at all quasi-periodic. Assuming the quasi-periodic recurrence of an event on the Lake Creek-Boundary Creek fault, the time elapsed since the most recent 2,859 cal yr BP event plays a crucial role in hazard assessment. The median ages of the megaturbidites were used to construct a lognormal distribution model for the probability of an earthquake on the Lake Creek-Boundary Creek fault in the next 50 years

(Fig. 39). The lognormal distribution is defined as $f^{LN}(x) = \frac{1}{\sqrt{2\pi\sigma \ln x}} \exp \frac{-(\ln(x)-\ln(\mu))^2}{2\sigma^2 \ln x}$.

Given the data set of four megaturbidite ages and three inter-event times, the time-dependent earthquake probability of an event occurring in the next 50 years on the western segment of the Lake Creek-Boundary Creek fault is 28%.

The existence of megaturbidites and rockslide deposits in and around Lake Crescent present a substantial seismic hazard for the region. There is significant evidence that the last megaturbidite was sourced by an onshore rockslide entering the lake as a result of an earthquake on the Lake Creek-Boundary Creek fault. The volumetric estimate of the subaqueous portion of the rock slide indicates that the resultant maximum displacement wave run up height on the shore opposite to Sledgehammer Point would be approximately 66 to 106 m. A wave of that size would be devastating to the small community of ~150 houses,

two resorts, National Park facilities (campgrounds, picnic areas, and scenic pull-outs along Highway 101) that are scattered along the perimeter of the lake. In addition, it would almost certainly dismantle significant portions of U.S. Highway 101 which wraps around Lake Crescent's eastern and southern shores. More than 200 people in Norway have died from inundation caused by subaerial slide generated displacement waves (Blikra et al. 2005). If an event similar to the Sledgehammer Point rockslide-displacement wave were to occur during the peak visitation season at Lake Crescent, there could be hundreds of lives lost. Because of the small size of Lake Crescent, warning times would be short after an event was triggered.

Previous megaturbidites are likely formed by subaerial mass wasting processes, although other triggering mechanisms such as lake-floor displacement and subaqueous mass wasting events generating displacement waves cannot be ruled out until further analysis on their source is completed. Nevertheless, waves generated from lake-floor displacement and subaqueous mass wasting events should not be discounted as a significant geologic hazard. For example, the M_w 6.2 1601 A.D. earthquake in Lake Lucerne, Switzerland created a subaqueous slide and subsequent 4 m displacement wave that drowned eight people (Cyat, 1601; Hilbe and Anselmetti, 2014).

This research should be used to help develop hazard mitigation and disaster response plans for citizens and infrastructure in at-risk communities of Lake Crescent and greater Clallam County, Washington. The only seismic risk assessment of the Lake Creek-Boundary Creek fault models a $M6.8$ earthquake scenario based on the rupture of the 30 km long eastern portion of the Lake Creek-Boundary Creek fault. The assessment estimates about \$646 million dollars in capital stock and income losses as well as hundreds of injuries (WA

State DNR, 2012). Earthquake scenario modelling of the western segment and full rupture (c. 65 km-long) of the Lake Creek-Boundary Creek fault is needed to further develop hazard mitigation plans. The western portion of the Lake Creek-Boundary Creek presently has no seismic hazard response plan. Full rupture of the Lake Creek-Boundary Creek fault would approximately double the length of the rupture therefore increasing its magnitude. The increase in magnitude can greatly change the estimated potential structural loss and impacts on life.

The Washington State Department of Natural Resources emphasizes hazard mitigation for tsunamis in coastal areas however no tsunami hazard mitigation plans exist for enclosed bodies of water such as Lake Crescent (WA State DNR, 2016). Although warning times for a displacement wave generated by subaerial rockslide would be very short, the geologic hazard should be brought to the attention of private homeowners, the National Park Service, and their visitors. Preparation for a lake displacement wave should include evacuation plans, education of locals and visitors, and the allocation of equipment and supplies in the case of an event. Early warning systems for rockslides and displacement waves have been installed in Tafjord, Norway after the Norwegian Geological Survey found that repeated rockslide-displacement wave events have occurred in the fjord (Sassa and Canuti, 2009). The overall monitoring system is equipped with various surface monitors, borehole monitoring, and meteorological stations (Sassa and Canuti, 2009). An early warning system could be implemented at Lake Crescent as a part of hazard mitigation efforts to reduce loss to life and property by rock fall and wave inundation.

5.0 SUMMARY AND CONCLUSIONS

The high resolution sedimentary record of Lake Crescent provides a history of regional earthquakes that have occurred in the past ~8,500 years. Lake Crescent megaturbidites are characterized by an erosively based, normally graded basaltic sand layer overlain by massive, homogenous silt with plant debris and a clay cap interstratified with chloritic clay and basaltic sand laminations. The voluminous deposits are sourced from onshore rockslides entering the lake as a result of earthquake ground shaking, but difficulties in determining the rockslide source for some megaturbidite layers still remain. Progressive offset of the megaturbidite deposits imaged in the subsurface of the north basin indicate that movement along the western portion of the Lake Creek-Boundary Creek and Sadie Creek fault zone is the likely source of earthquakes that trigger the rockslides. Assuming no additional megaturbidites were erased by scour from the sedimentary record, the presence of four megaturbidite deposits provides a time-dependent earthquake probability of 28% in the next 50 years for the western segment of the Lake Creek-Boundary Creek fault. The maximum displacement wave run up during the last rockslide-displacement wave event is estimated to be 66 to 106 m at the opposing shore based upon a global landslide volume-to-wave run up scaling relationship; consequently, risk assessment for such future events in the area should be examined more closely to reduce losses to human life and infrastructure.

6.0 FUTURE WORK

Future work to help resolve the paleoseismic record of Lake Crescent should include the coring of closed depressions on landslide deposits. Cores should be made through the sediment fill of the depression to the transition of landslide debris. Intact organic matter found in the transition from sediment fill to debris can be dated to help estimate minimum ages of the deposits and further strengthen the evidence that subaerial rockslides entering the lake are the sources of the megaturbidites. Numerical simulations of lake-floor displacement generated waves would be key to testing the hypothesis that subaerial rockslides are the sources of the megaturbidites. In addition, displacement wave run up modeling that utilizes the recently acquired high resolution bathymetry is needed to help further develop risk assessment of wave inundation for future events.

Recruitment of a coring system capable of retrieving longer sediment cores could provide samples of the older inferred megaturbidite layers observed in the north and south basin seismic reflection profiles. Longer cores are especially needed in the south basin where only one megaturbidite layer was recovered. Additionally, seismic reflection surveying and coring of Lake Sutherland could produce information on at least two megaturbidites that are known to have occurred before the separation of the two lakes. Additional megaturbidites attributed to rock slides around Lake Sutherland (e.g., not affecting Lake Crescent's sedimentary record) could be present; this evidence could provide a higher resolution recurrence interval for earthquakes on the Lake Creek-Boundary Creek fault.

Table 1. Lake Crescent core IDs, length, water depth at core site, and location.

Core ID (SHAKE-CRSC15-)	Core Length (m)	Water Depth (m)	Latitude	Longitude
1A-1K	1.07	83.5	48.073713	-123.785547
1B-1K	2.18	83.4	48.073817	-123.785367
2A-1K	5.31	140.3	48.0875	-123.775433
2C-1K	6.75	140.5	48.087383	-123.77555
3A-1K	0.41	19.7	48.091105	-123.795898
3C-1K	2.635	19.6	48.091083	-123.796233
4A-1K	7.855	83.5	48.06375	-123.892283
5A-1K	4.86	179.7	48.056883	-123.8532
6A-1K	5.36	179.1	48.058	-123.839617
7A-1K	6.745	141.0	48.083917	-123.782217
7C-1K	6.53	141.0	48.083733	-123.7821
8A-1K	7.905	140.6	48.083533	-123.76965
9A-1K	2.05	125.7	48.08205	-123.757583
10A-1K	0.99	66.0	48.068633	-123.782717

Table 2. Closed depression sample ID, soil pit depth, and location.

Sample ID	Depth (cm)	Latitude	Longitude
CD 1	90	48.083477	-123.731082

Table 3. Parameters for the boundary shear stress calculations.

Parameter	Symbol	Value
Water density	ρ_w	0.9997 g/cm ³
Kinematic viscosity of water	ν	1.31 x 10 ⁻² g/(cm*s)
Dynamic viscosity of water	μ	1.31 x 10 ⁻² g/(cm*s)
Grain density	ρ	2.65 g/cm ³
Gravitational acceleration	g	981 cm ² /s
Grain diameter	D	Reported in results
Corey Shape Factor	CSF	0.7
Non-dimensional settling velocity	W_*	Dietrich Diagram (Dietrich, 1982)
Von Karman constant	k	0.41

Table 4. Original counted minerals and rock fragment types (n = 16) and recalculated parameters (n = 4) for the sediment core sand petrologic study.

Counted minerals and rock fragment types		Recalculated Parameters
Qm	Monocrystalline quartz	$Q = Qm + Qp + Lch$
Qp	Polycrystalline quartz	
P	Plagioclase feldspar	$F = P + K$
K	Potassium feldspar	$S = Ls$
Ls	Sedimentary rock fragments	$V = Lvg + Lv + Px + Amp + M + O$
Lch	Chert	
Lvg	Volcanic glass	
Lv	Volcanic rock fragments	
Li	Plutonic rock fragments	
Lm	Metamorphic rock fragments	
Px	Pyroxene	
Amp	Amphibole	
Ol	Olivine	
M	Mica	
O	Opaque minerals	
Olg	Other lithic grains	

Table 5. Dependent parameters of the Evers and Hager (2016) displacement wave height equation.

Parameter	Symbol	Dependent variables
Slide velocity	V_s	45 m/s
Gravitational acceleration	g	9.81 m/s ²
Slide mass	m_s	1.9 x 10 ¹⁰ kg
Water density	ρ_w	1000 kg/m ³
Slide thickness	s	55 m
Slide impact angle	α	45°
Slide width	b	820 m

Table 6. Independent parameters of the Evers and Hager (2016) displacement wave height equation.

Scenario Name	Propagation Distance (r)	Propagation Angle (γ)	Still water depth (h)
Log Cabin Resort	2624 m	+50°	140 m
Opposite Shore	1070 m	0°	100 m
Nature Bridge	950 m	-50°	100 m
U.S. Highway 101	6182 m	-40°	170 m

Table 7. Diagnostic peak wavenumbers (cm^{-1}) reported from the FTIR analysis of the Lake Crescent sample compared to reported values of an infrared spectrum of chlorite from Gopal et al. 2004.

Peak wavenumbers (cm^{-1}) (Lake Crescent)	Peak wavenumbers (cm^{-1}) reported from Gopal et al. 2004	Assignment reported from Gopal et al. 2004
654	653	M-OH libration
749	-----	-----
987	998	Si-O stretching
1633	1627	-OH bending
3283	-----	-----
3448	3438	-OH stretching
3596	3589	-OH stretching

Table 8. Lake Crescent radiocarbon samples with reported calibrated and uncalibrated age determinations.

Core Segment ID	Depth in core segment (cm)	Carbon material dated	^{14}C age \pm 1 σ error (yr BP)	Calibrated 95% age range (cal yr BP)	Median age of 95% range (cal yr BP)
2C-1K-5	44.5-45.5	Plant fragments	6208 \pm 33	7006-7242	7097
3C-1K-1	70-75	Wood and bark fragments	5010 \pm 63	5619-5902	5753
8A-1K-4	92-94	Wood and bark fragments	5007 \pm 28	5656-5889	5736
9A-1K-2	41-50	Plant fragments	2766 \pm 28	2785-2943	2859
9A-1K-2	98-100	Woody sticks	3673 \pm 27	3921-4088	4015
CD 1	90	Charcoal	4471 \pm 29	4976-5287	5173

Table 9. Petrologic sand counts of the 16 parameters from EL1 deposits (orange), EL2 deposits (white), and streams (blue).

Sample ID	Depth in core segment (cm)	Qm	Qp	P	K	Ls	Lch	Lvg	Lv	Li	Lm
4A-1K-2	54.5-55	3	5	2	10	36	0	3	121	0	0
4A-1K-2*	120-121	0	0	1	7	14	0	5	111	0	0
4A-1K-3	12-13	3	2	2	11	16	1	4	129	0	0
4A-1K-4	123-124	2	1	0	22	3	0	15	139	0	0
6A-1K-1	81-82	1	4	4	21	141	3	1	58	0	0
6A-1K-2	131-132	7	29	1	15	140	5	1	52	0	0
6A-1K-3	33-34	3	4	2	10	13	1	22	143	0	0
6A-1K-4	143-144	3	11	0	11	77	3	4	113	0	0
7C-1K-4	34-35	1	3	2	14	10	1	4	133	0	0
8A-1K-5	83-84	6	21	5	17	20	14	10	138	0	0
9A-1K-1	40-41	0	0	2	9	32	1	14	143	0	0
Aurora	-	3	17	0	0	261	8	0	0	0	0
Barnes	-	0	3	1	2	6	1	1	244	0	0
Eagle	-	23	32	0	0	240	3	0	0	0	0
Fairholm	-	4	9	0	2	240	1	0	8	0	0
Lapoel	-	12	45	0	0	204	5	0	9	0	0
Piedmont	-	74	65	9	4	84	18	3	28	0	0
Smith	-	4	19	0	1	225	17	0	7	0	0
West Barnes	-	20	10	3	0	242	2	0	9	0	0

Table 9 continued.

Sample ID	Depth in core segment (cm)	Px	Amp	Ol	M	O	Olg
4A-1K-2	54.5-55	24	0	0	86	10	0
4A-1K-2*	120-121	5	0	0	150	7	0
4A-1K-3	12-13	17	0	0	104	11	0
4A-1K-4	123-124	23	5	0	80	10	0
6A-1K-1	81-82	9	0	0	19	39	0
6A-1K-2	131-132	4	0	0	16	30	0
6A-1K-3	33-34	4	0	0	71	27	0
6A-1K-4	143-144	22	1	0	26	29	0
7C-1K-4	34-35	28	1	0	67	36	0
8A-1K-5	83-84	13	0	0	36	20	0
9A-1K-1	40-41	14	0	0	63	22	0
Aurora	-	2	0	0	3	6	0
Barnes	-	9	5	0	8	20	0
Eagle	-	0	0	0	1	1	0
Fairholm	-	1	0	0	24	11	0
Lapoel	-	2	0	0	17	6	0
Piedmont	-	4	0	0	8	3	0
Smith	-	4	0	0	6	17	0
West Barnes	-	4	0	0	3	7	0

Table 10. Petrologic sand counts of the recalculated parameters from EL1 deposits (orange), EL2 deposits (white), and streams (blue). The relative amounts of each recalculated parameter are reported as percentages (%Q, %F, %S, %V).

Sample ID	Depth in core segment (cm)	Q	F	S	V	%Q	%F	%S	%V
4A-1K-2	54.5-55	8	12	36	244	2.7	4	12	81.3
4A-1K-2	120-121	0	8	14	278	0	2.7	4.7	92.7
4A-1K-3	12-13	6	13	16	265	2	4.3	5.3	88.3
4A-1K-4	123-124	3	22	3	272	1	7.3	1	90.7
6A-1K-1	81-82	8	25	141	126	2.7	8.3	47	42
6A-1K-2	131-132	41	16	140	103	13.7	5.3	46.7	34.3
6A-1K-3	33-34	8	12	13	267	2.7	4	4.3	89
6A-1K-4	143-144	17	11	77	195	5.7	3.7	25.7	65
7C-1K-4	34-35	5	16	10	269	1.7	5.3	3.3	89.7
8A-1K-5	83-84	41	22	20	217	13.7	7.3	6.7	72.3
9A-1K-1	40-41	1	11	32	256	0.3	3.7	10.7	85.3
Aurora	-	28	0	261	11	9.3	0	87	3.7
Barnes	-	4	3	6	287	1.3	1	2	95.7
Eagle	-	58	0	240	2	19.3	0	80	0.7
Fairholm	-	14	2	240	44	4.7	0.7	80	14.7
Lapoel	-	62	0	204	34	20.7	0	68	11.3
Piedmont	-	157	13	84	46	52.3	4.3	28	15.3
Smith	-	40	1	225	34	13.3	0.3	75	11.3
West Barnes	-	32	3	242	23	10.7	1	80.7	7.7

Table 11. Boundary shear stress (τ_b) values required to move the median and 90th percentile grain size of silt particles as suspended load in core 6A-1K (highlighted in grey) and coarsest particles as suspended load from the bases of cores 4A-1K, 6A-1K, 2C-1K, 8A-1K, and 7C-1K.

Core ID	Depth in core segment (cm)	D₅₀ grain size (μm)	τ_b D₅₀ (g/cm*s²)	D₉₀ grain size (μm)	τ_b D₉₀ (g/cm*s²)
6A-1K-4	45	13	1.1×10^{-3}	49	0.2
4A-1K-2	120.5	15	2.1×10^{-3}	60	0.6
6A-1K-4	142	227	33	616	445
2C-1K-2	112	258	58	485	273
8A-1K-4	42	353	137	807	946
7C-1K-4	44	475	551	1105	2969

Table 12. Wet sediment mass, wet sediment volume, dry sediment volume, and dry sediment mass of the EL1-A deposit. Calculations were made assuming 40% sediment porosity.

	North Basin	South Basin	Total
Wet volume (* 10⁶ m³)	1.88	2.91	4.79
Wet sediment mass (* 10⁶ T)	3.76	5.82	9.58
Dry volume (* 10⁶ m³)	1.13	1.75	2.87
Dry sediment mass (* 10⁶ T)	2.26	3.49	5.75

Table 13. Dependent parameters of the Evens and Hager (2016) displacement wave height equation and reported displacement wave heights at specified distances offshore.

Scenario Name	Propagation Distance (m)	Propagation Angle (°)	Still water depth (m)	Distance offshore (m)	Wave height (m)
Log Cabin Resort	2624	+50	140	243	5
Opposite Shore	1070	0	100	139	20
Nature Bridge	950	-50	100	201	11.5
U.S. Highway 101	6182	-40	170	333	3

Table 14. Volume and maximum wave run up of historical landslides that generated displacement waves in lakes or fjords around the world.

Slide Name	Volume (Mm³)	Maximum wave run up (m)	References
Lituya Bay, Alaska	30	524	Miller 1960
Loenulykke 3, Norway	1.1	74	NVE 2016
Tafjord, Norway	3	62	Jorstad 1968
Mt. Colonel Foster, British Columbia	1.5	51	Evans 1989
Tjelle, Norway	12	50	NVE 2016
Loenulykke 1, Norway	0.35	40	NVE 2016
Chehalis Lake, British Columbia	2.5	38	Roberts et al. 2013
Skafjellet, Norway	6	30	NVE 2016
Loen 2, Norway	0.045	5	NVE 2016
Gold Arm, New Zealand	0.2	4.5	Hancox et al. 2003
Skrenakken, Norway	0.01	5	NVE 2016

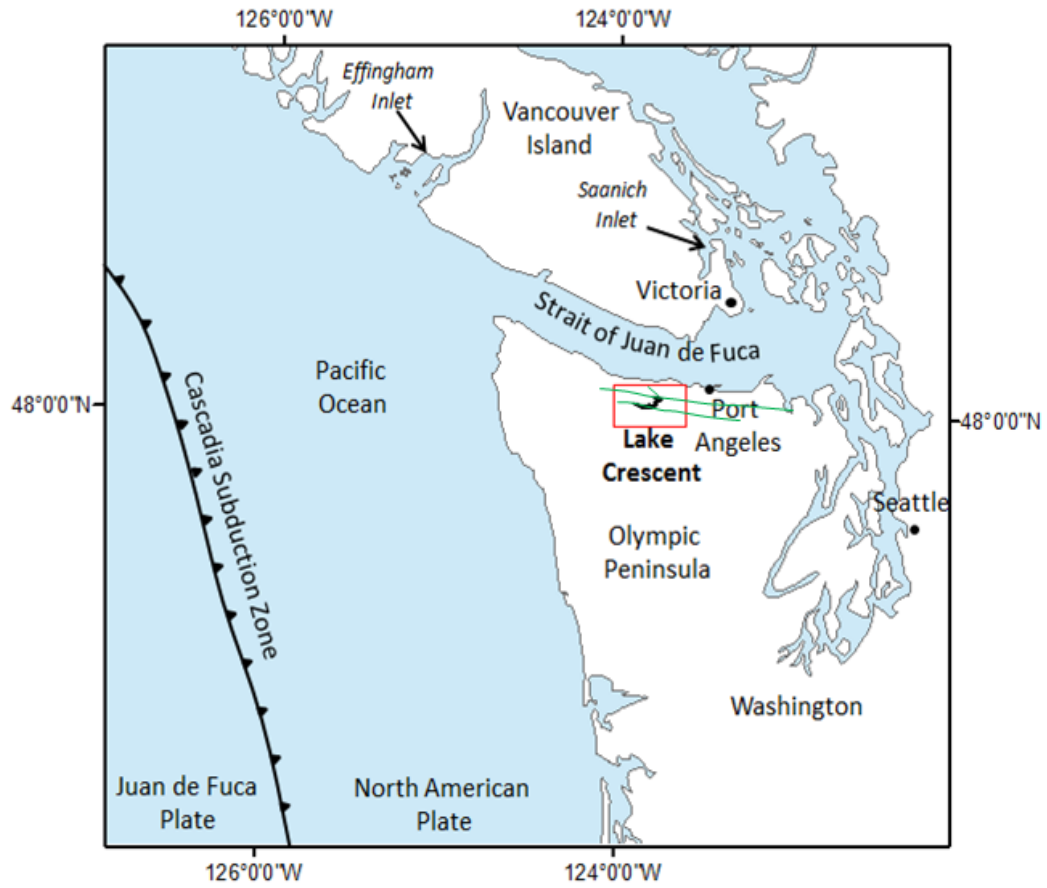


Figure 1. Generalized tectonic map of western Washington with surrounding features. Lake Crescent is enclosed in the red box. Three crustal faults that run directly beneath Lake Crescent are outlined in green.

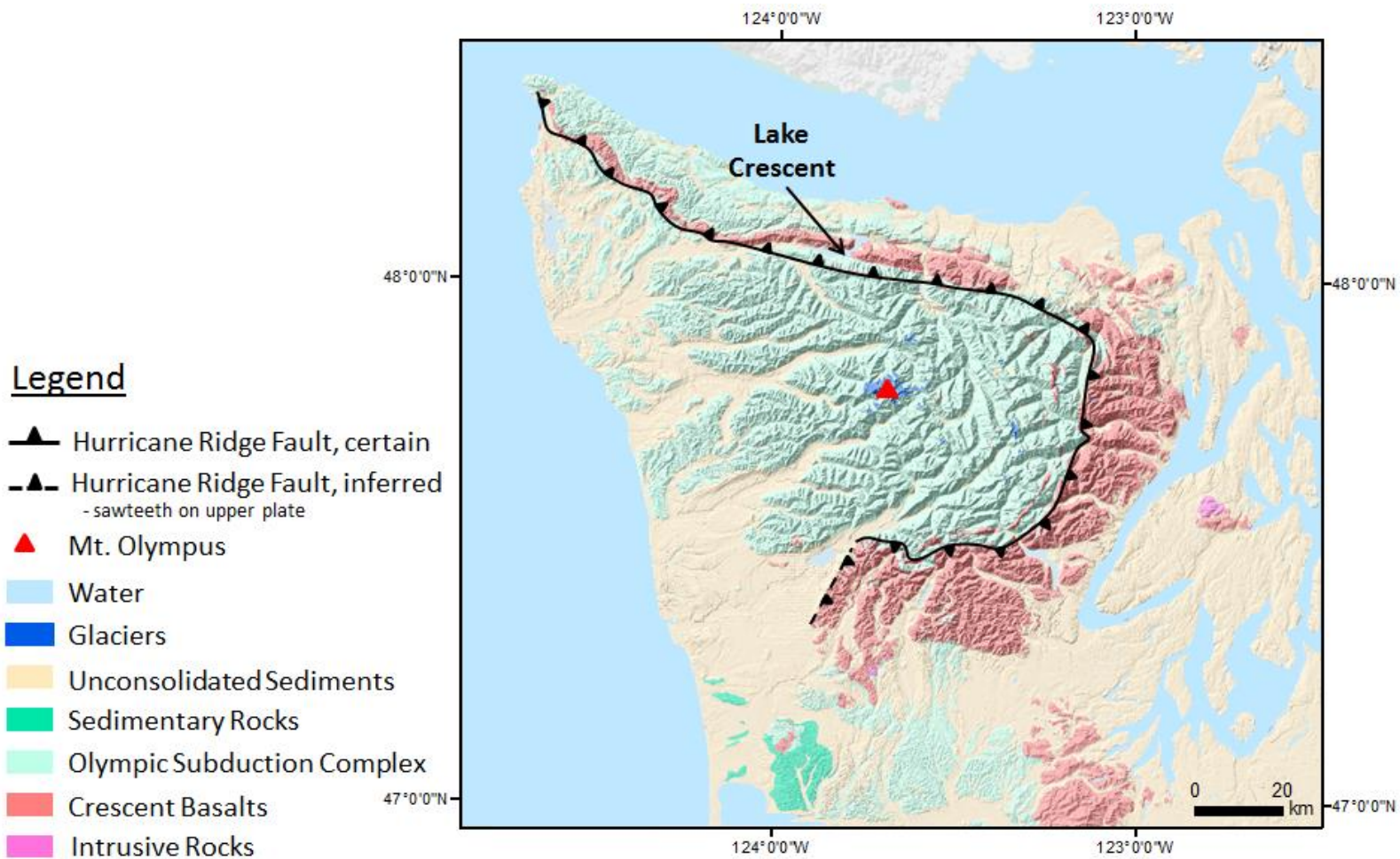
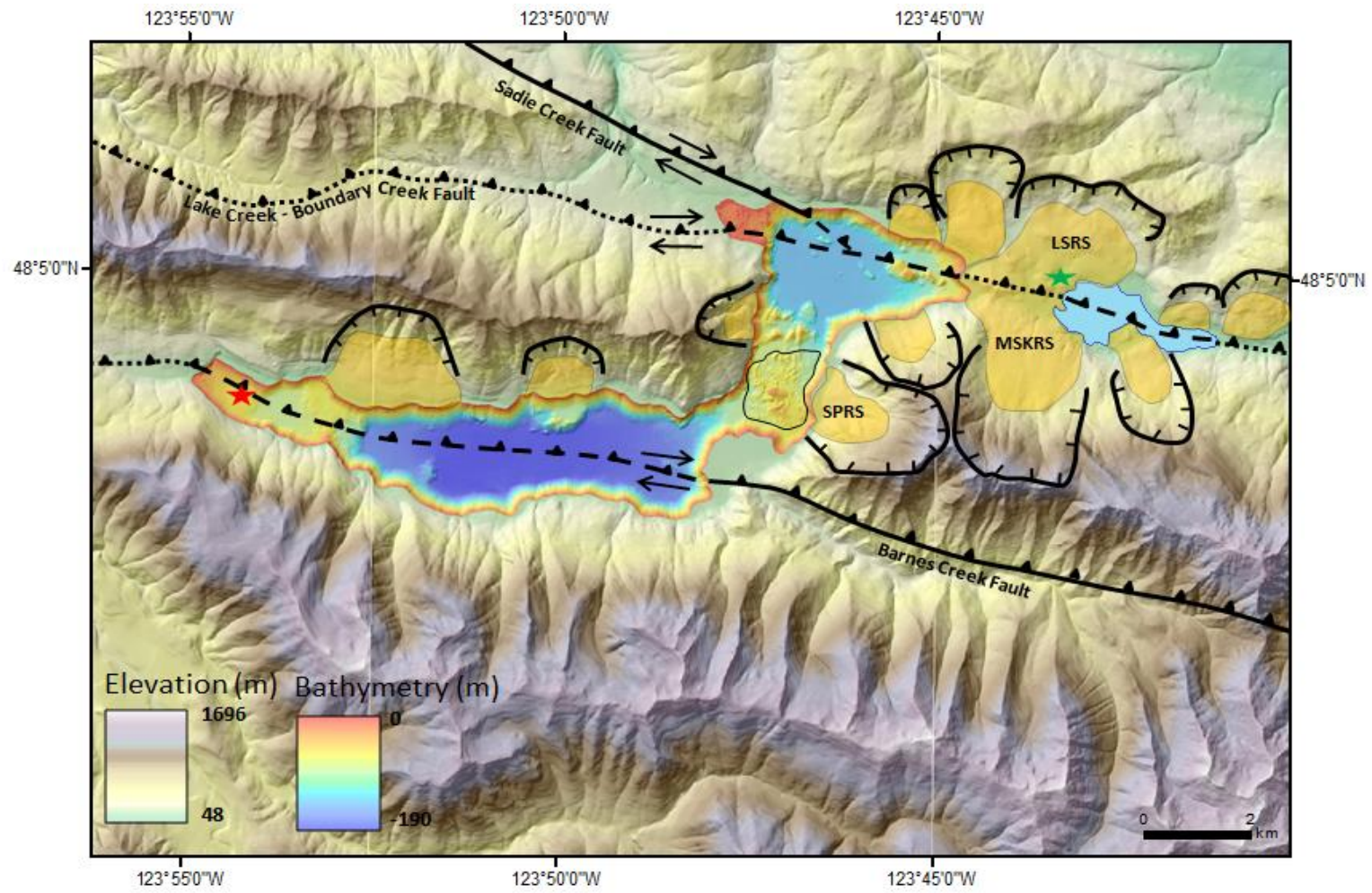





Figure 2. Simplified geologic map of the Olympic Peninsula (WA State DNR, 2010).


Figure 3. Surrounding rockslides and faults in the Lake Crescent region. Right lateral fault motion indicated by arrows. Vertical motion indicated by U (up) and D (down). Bathymetric map of Lake Crescent and smaller Lake Sutherland is surrounded by 10 m DEM topography (USGS, 2001). The subaqueous portion of the Sledgehammer Point rockslide is outlined in black on a 2.5 m resolution bathymetric map.





-  Landslide debris
- LSRS** – Lake Sutherland Rockslide Complex
- MSKRS** – Mount Storm King Rockslide
- SPRS** – Sledgehammer Point Rockslide


-  **Landslide scarp**, certain – hachures point down scarp

-  **Thrust fault**, certain – sawteeth on upper plate

-  **Thrust fault**, inferred

-  **Thrust fault**, approximate

-  Landslide closed depression ¹⁴C date

-  Drowned tree ¹⁴C date

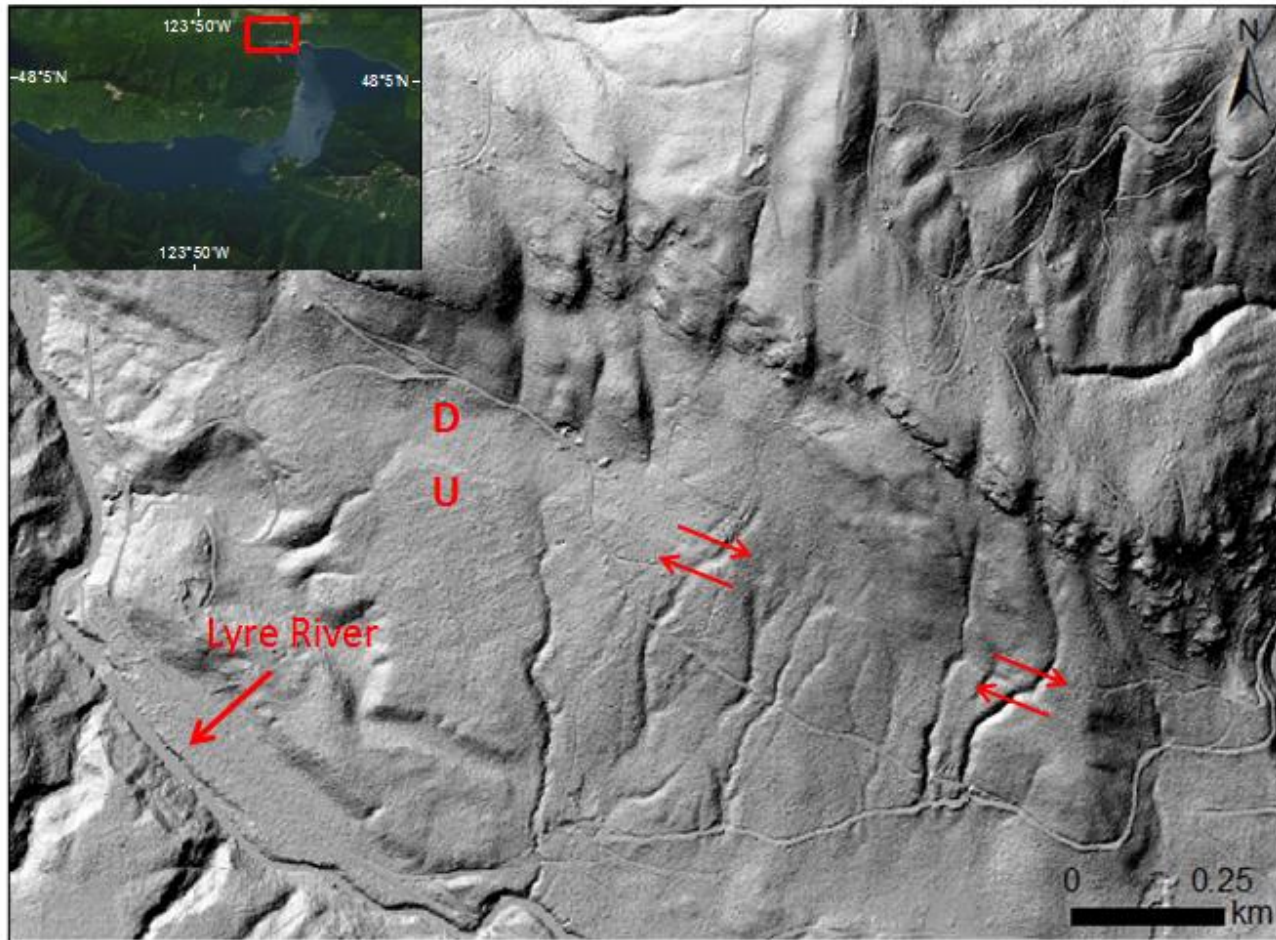


Figure 4. Lidar imagery of the Sadie Creek fault scarp (Puget Sound LiDAR Consortium, 2015). Right lateral fault motion indicated by offset drainages and arrows. Vertical motion indicated by U (up) and D (down).

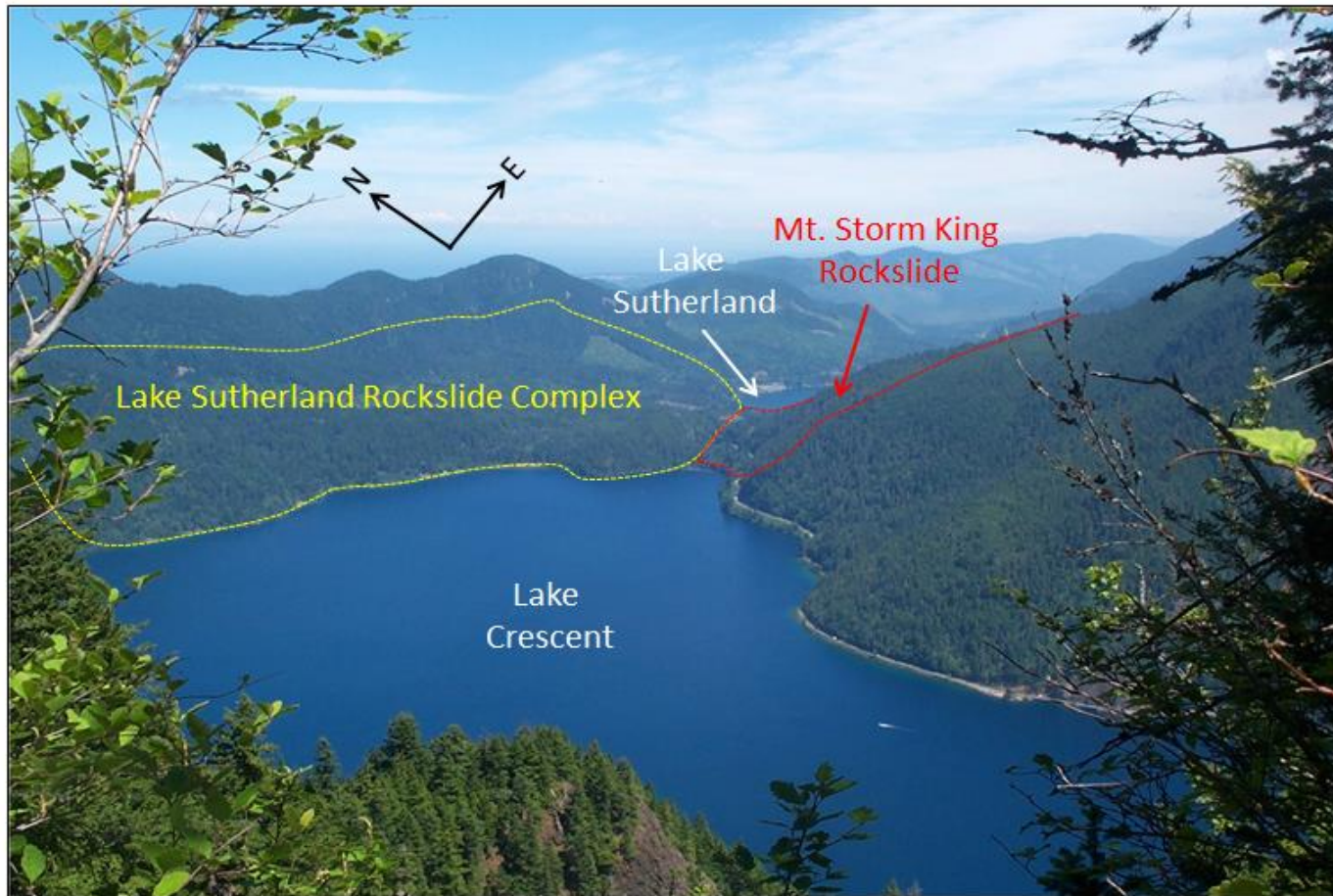


Figure 5. Photograph (Taylor, 2008) taken from Pyramid Peak (opposite shore to Mt. Storm King) showing the coalescing rockslides that separated Lake Crescent from Lake Sutherland c. 4,000 cal yr BP (Pollen, 2016).

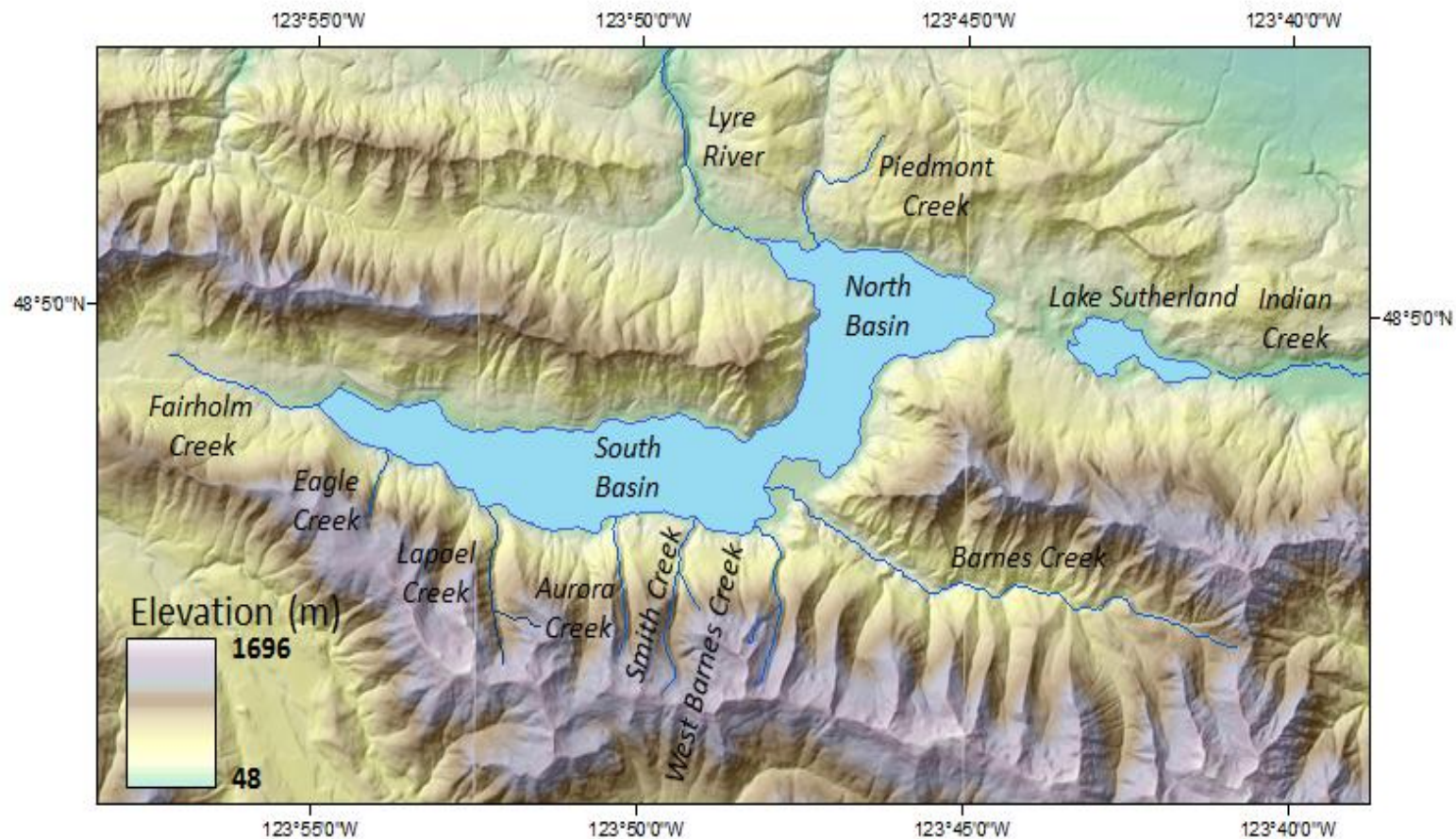
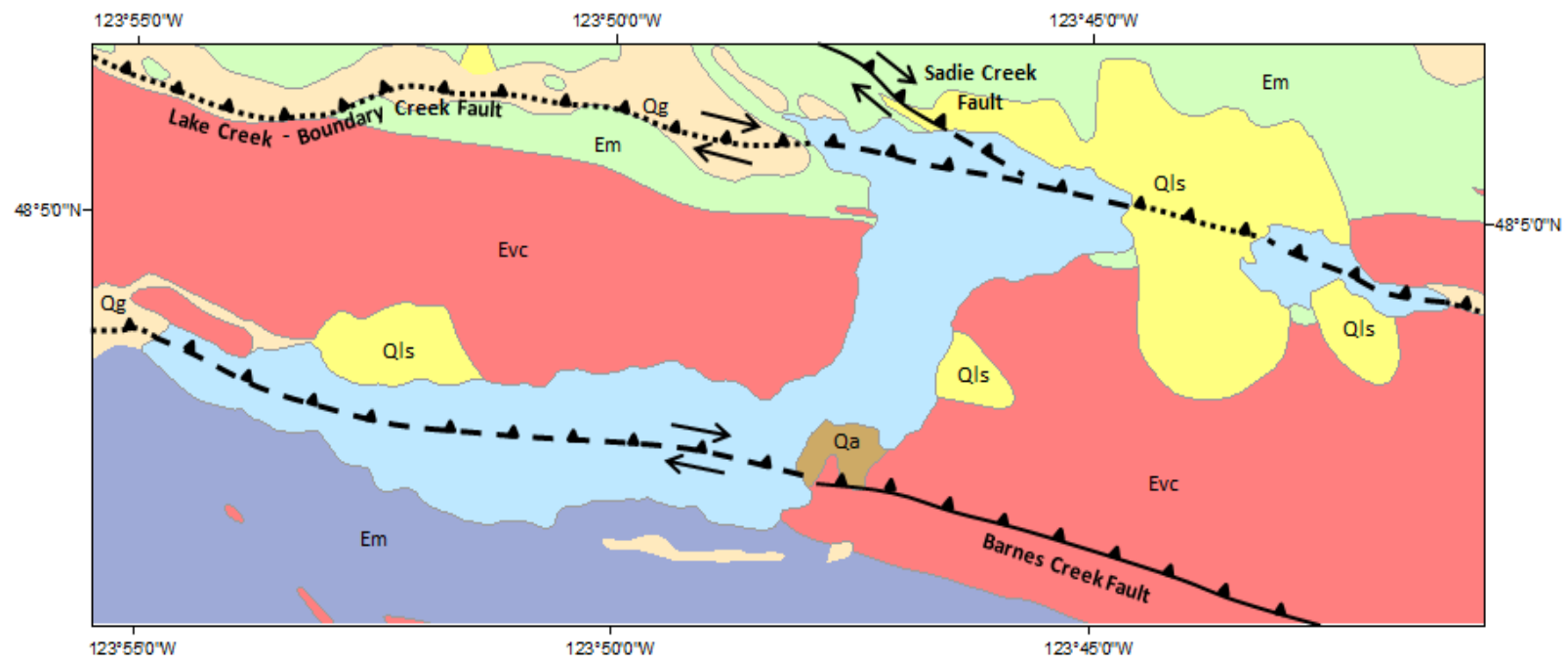


Figure 6. The main tributaries, basin names, and drainage outlet of Lake Crescent. The eastward flowing Indian Creek was the drainage outlet of ancestral Lake Crescent. The northward flowing Lyre River is the current drainage outlet. Surrounding topography is a 10 m DEM (USGS, 2001).


Figure 7. Simplified geologic map of the Lake Crescent region and adjacent Lake Sutherland adapted from Schasse, 2003 (WA State DNR, 2010). Right lateral fault motion indicated by arrows. Vertical motion indicated by U (up) and D (down) with the teeth on the upthrown side.





Qa **Alluvium (Holocene)**- stratified stream deposits of well rounded and sorted cobbles, gravels, sand, silt, and clay

Qls **Landslide deposits (Pleistocene?/Holocene)**- mass wasting deposits consisting of chaotic to intact failure material such as large boulders, cobbles, gravel, sand, silt and clay

Qg **Glacial outwash and till (Pleistocene)**- undifferentiated glacial deposits; outwash deposits consist of stratified, moderate to well-rounded sand and gravel; till deposits consist of unstratified, compacted mixture of poorly sorted clay, silt, gravel, and boulders

 **Thrust fault, certain** - sawteeth on upper plate

 **Thrust fault, inferred**

 **Thrust fault, approximate**

Em **Hoko River, Lyre, and Aldwell Formations (Upper Eocene-Middle Eocene)**- marine sedimentary formations consisting of thin to medium bedded sandstone, siltstone, and conglomerate

Evc **Crescent Formation (Middle-Lower Eocene)**- marine pillow and flow dominated basalts interbedded with siltstone, sandstone, conglomerate, chert, and limestone; some local breccia, tuffaceous sedimentary rock, and rhyolite; abundant chlorite and zeolites

Em **Blue Mountain Unit (Eocene-Paleocene?)**- marine sedimentary rocks consisting of laminated and rhythmically bedded sandstone, siltstone, argillite, and conglomerate; thick beds of massive sandstone and conglomerate

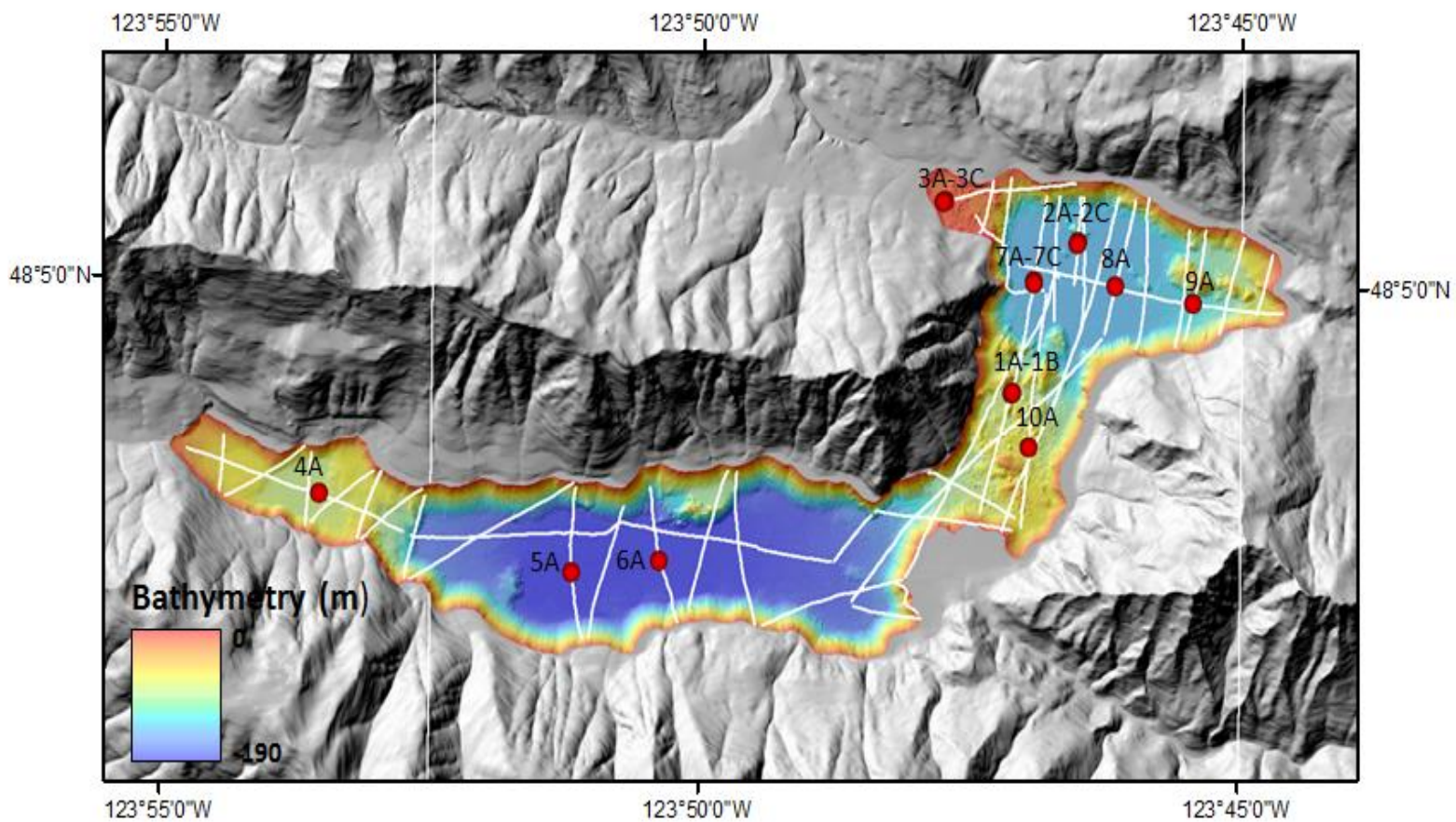


Figure 8. 2013 Chirp seismic survey (white lines) and 2015 core locations and names (red). The 2.5 m resolution bathymetric map is surrounded by 10 m DEM topography (USGS, 2001).

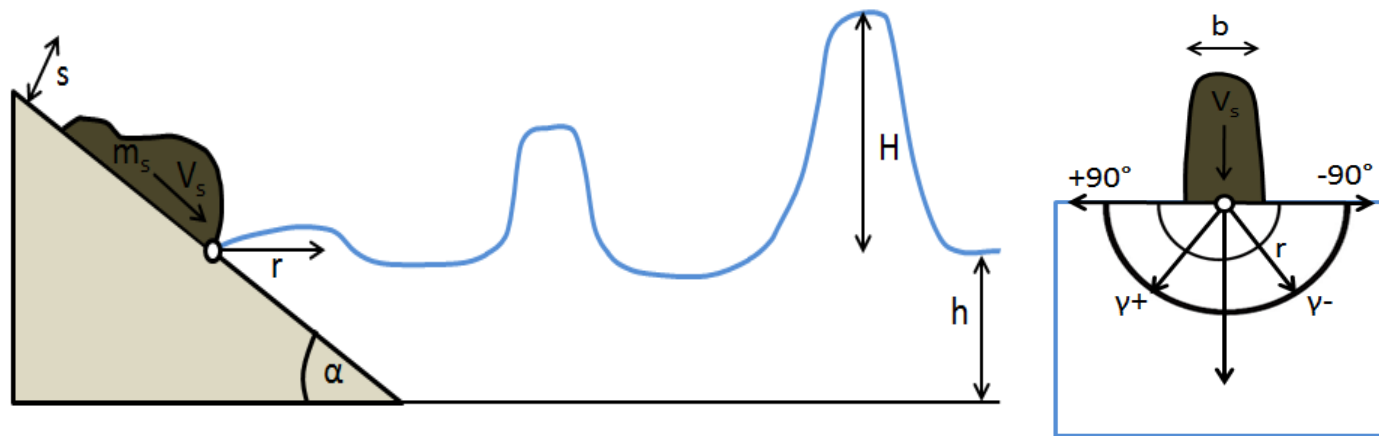


Figure 9. Cross section for $\gamma = 0^\circ$ (left) and top view (right) of independent and dependent parameters of leading displacement wave height adapted from Evers and Hager (2016).

Figure 10. Seismic line from the central portion of the north basin (see map inset). The 2 m thickness of *Seismic Facies A* is denoted by the green arrow. Five packages of *Seismic Facies B* are observable and outlined in orange. The irregular scour surface of the first *Seismic Facies B* layer is indicated by the purple arrows. Offset and folded *Seismic Facies B* layers are apparent along the trace of the Lake Creek-Boundary Creek fault. The vertical exaggeration is 14x.

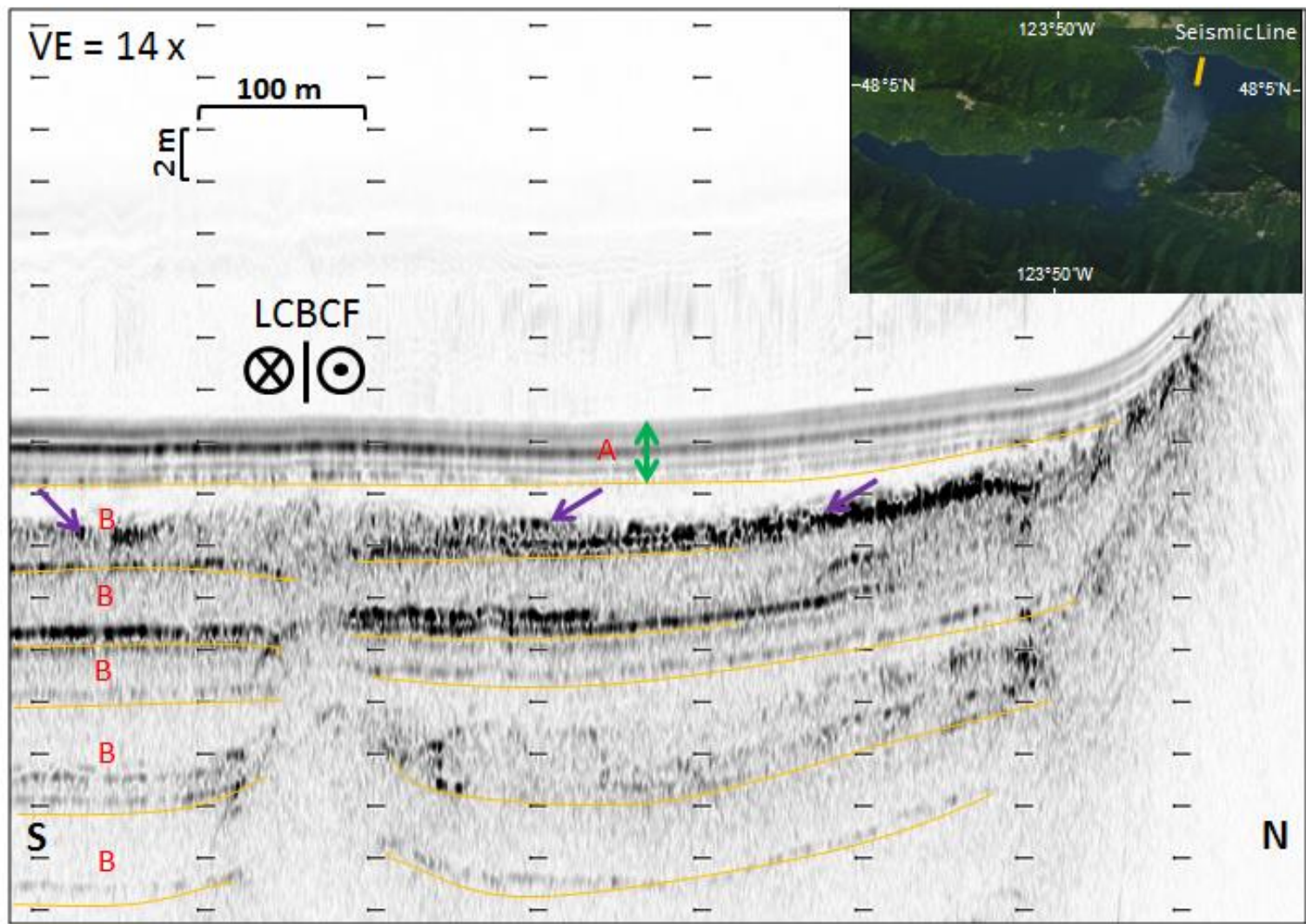


Figure 11. Seismic line from the central portion of the north basin (see map inset). The 2 m thickness of *Seismic Facies A* is annotated by the green arrow. Four packages of *Seismic Facies B* are outlined by the orange lines. Offset and folded sequences of *Seismic Facies B* are visible along the trace of the Lake Creek-Boundary Creek fault. The red arrows point to the trace of the Sadie Creek fault (SCF). The undeformed *Seismic Facies A* unit at the top of the sequence overlies four *Seismic Facies B* units that appear to be consecutively offset by ~1 m in four separate faulting events. The vertical exaggeration is 22x. The exaggerated dip of 45° is equal to the apparent dip of 2.6° .

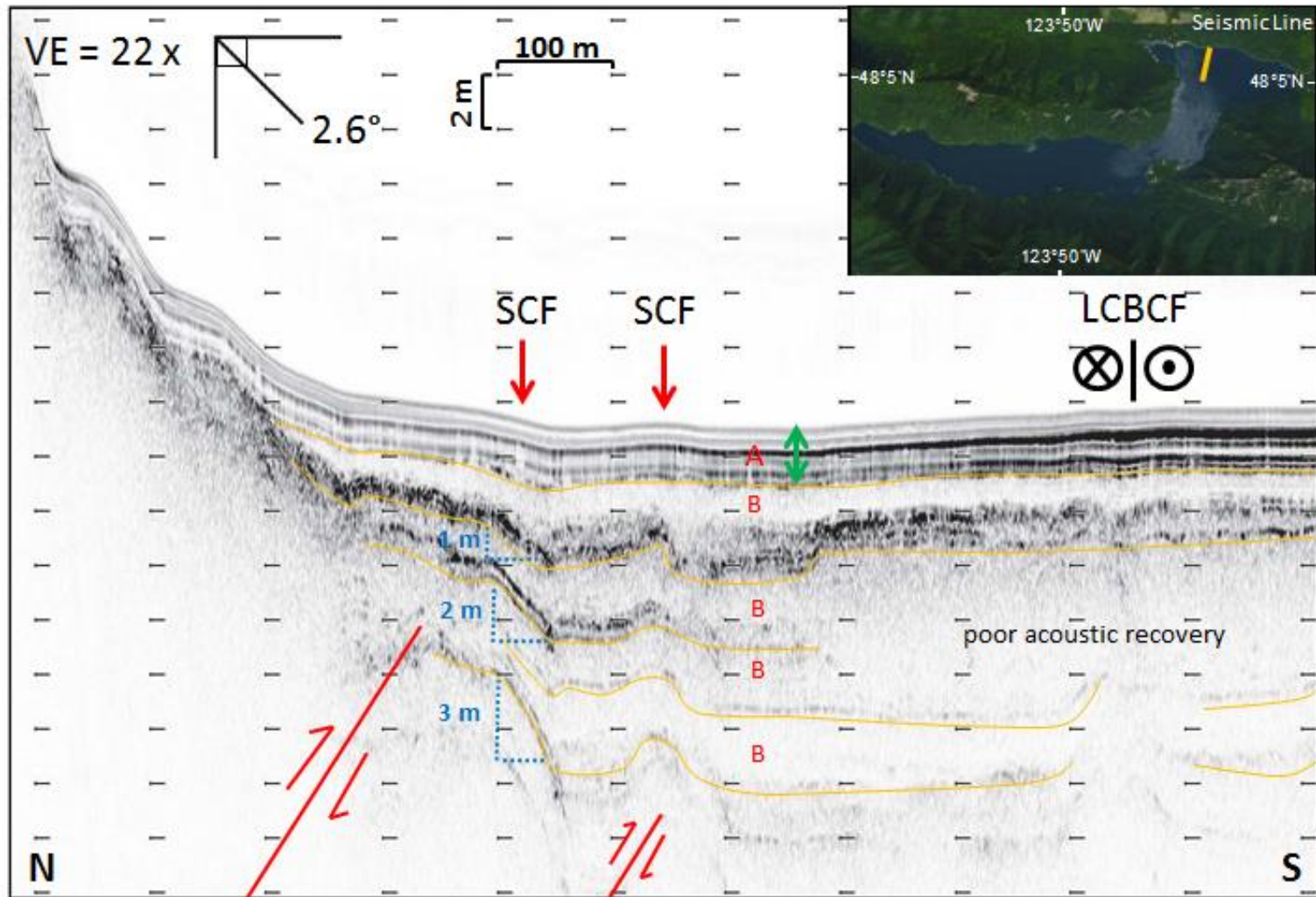


Figure 12. Seismic line from the central portion of the south basin (see map inset). The top 4 m thick and middle 1 m thick packages of *Seismic Facies A* units are annotated by the green arrow. Two *Seismic Facies B* layers are outlined by the orange lines. The less irregular scour surface of the first *Seismic Facies B* layer is indicated by the purple arrows. No fault-related deformation is visible in the strata, in contrast to what is observed from the lake's north basin. The vertical exaggeration is 23x.

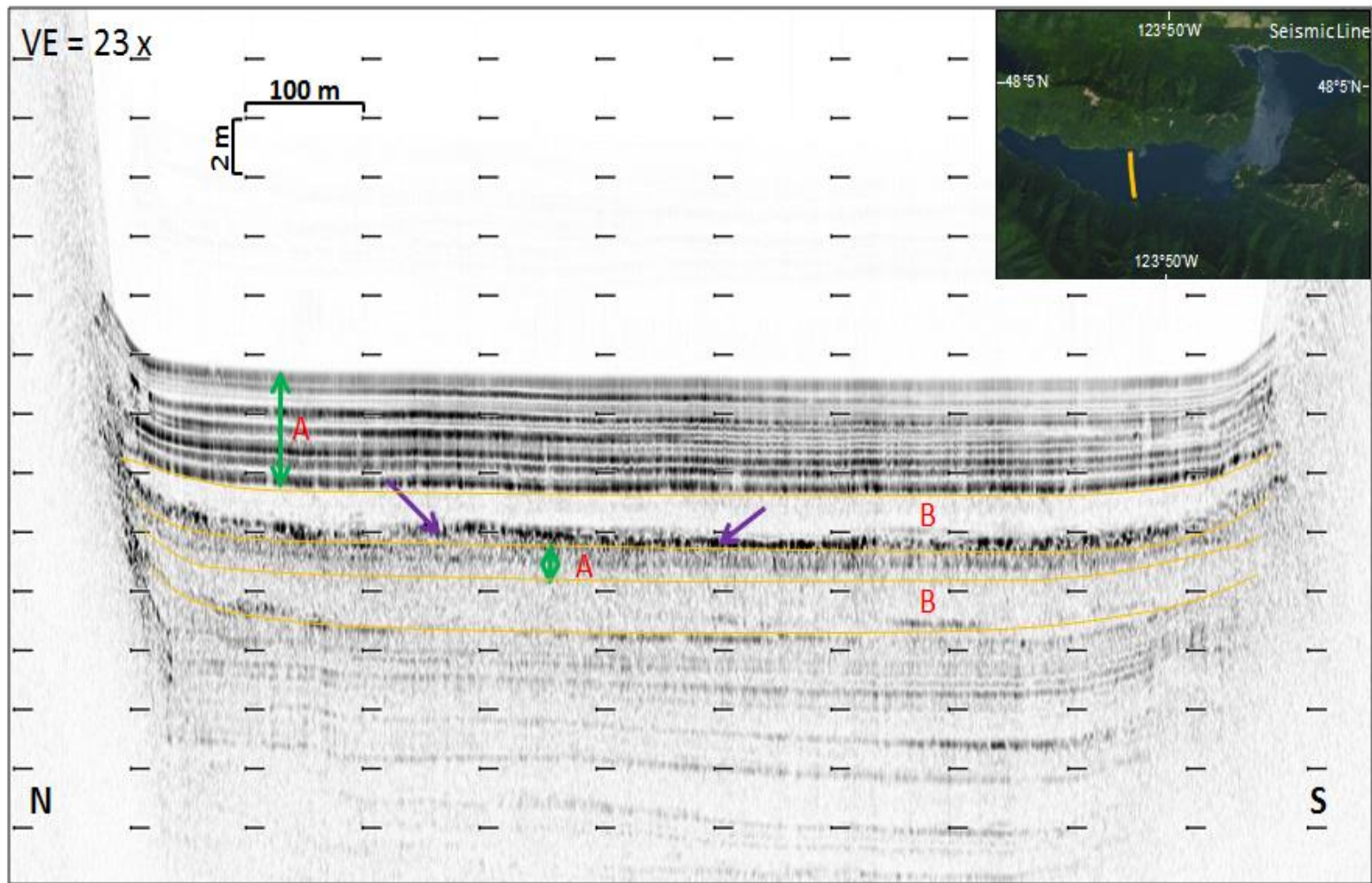


Figure 13. Seismic line from the western portion of the south basin (see map inset). The 2 m thick *Seismic Facies A* is annotated by the green arrow. One thin layer of *Seismic Facies B* is visible in this shallow sub-basin. The wedge-shaped *Seismic Facies C* is outlined in purple. The vertical exaggeration is 36x.

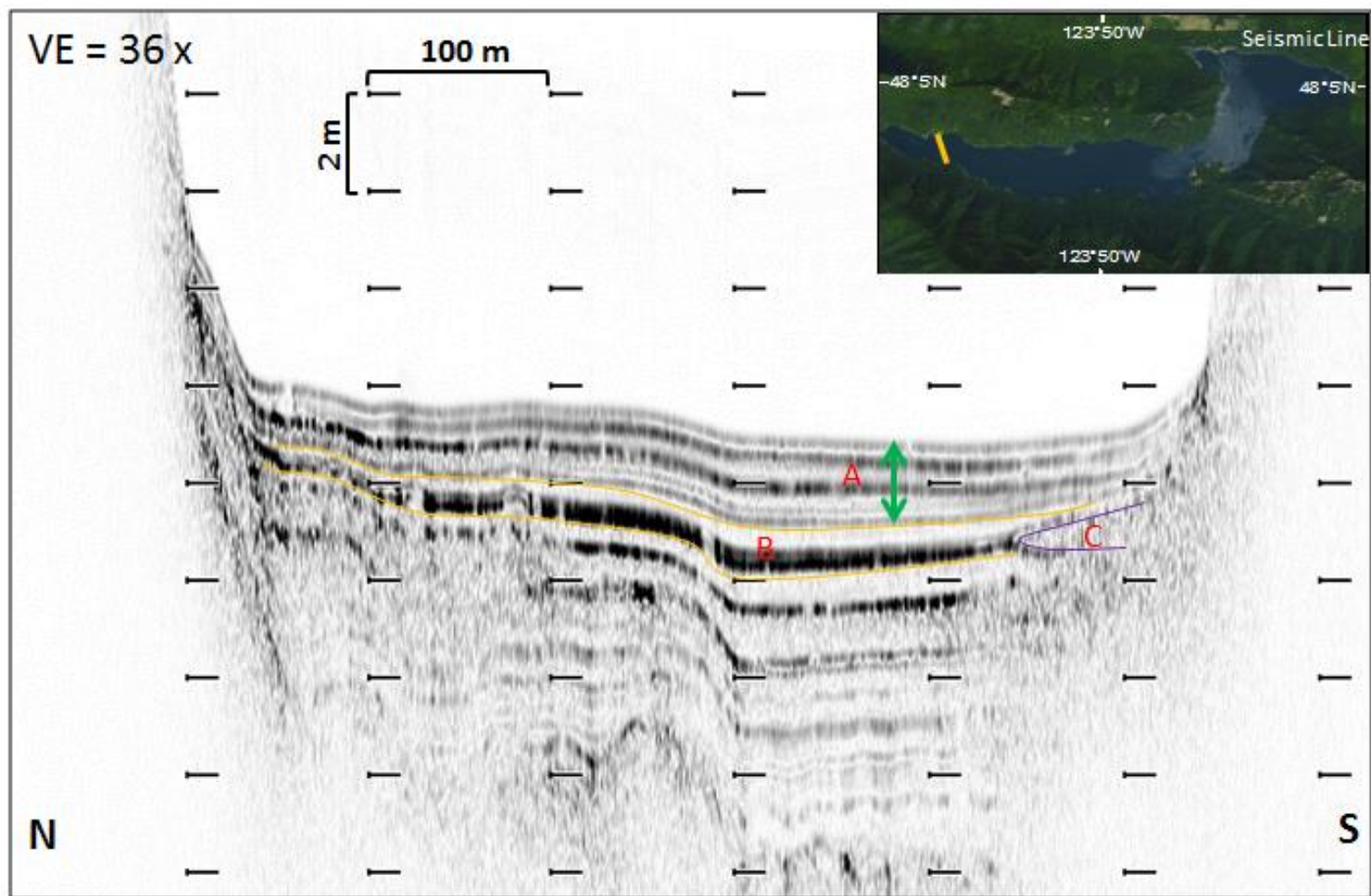


Figure 14. Seismic line from the central channel between the north and south basins (see map inset). The red arrows point to the parts of the tallest subaqueous rockslide deposits. The inset image of the small intra-deposit depressions (see map inset) shows the presence of 2 m of *Seismic Facies A*, but no *Seismic Facies B* deposits. The vertical exaggeration is 16x.

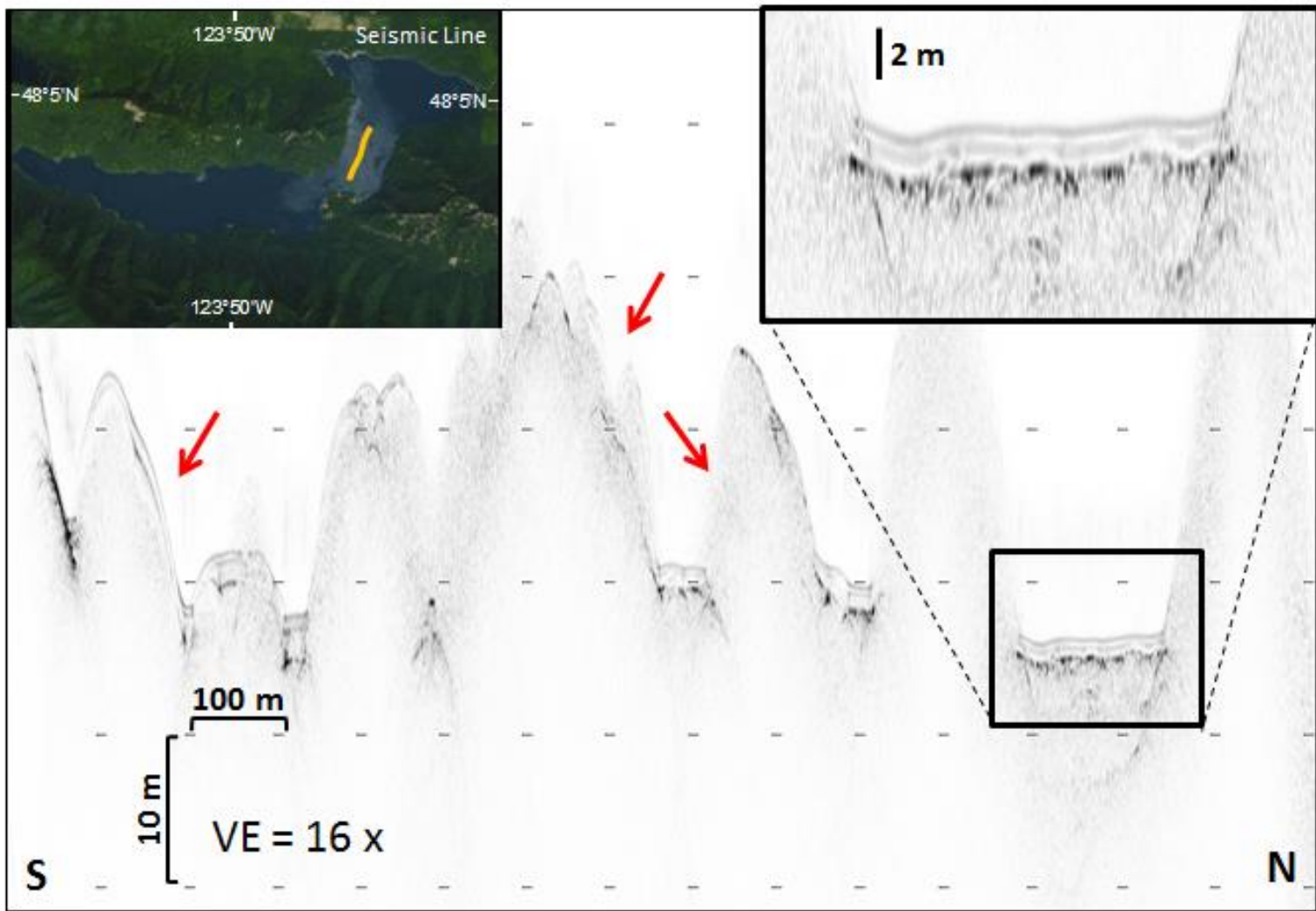
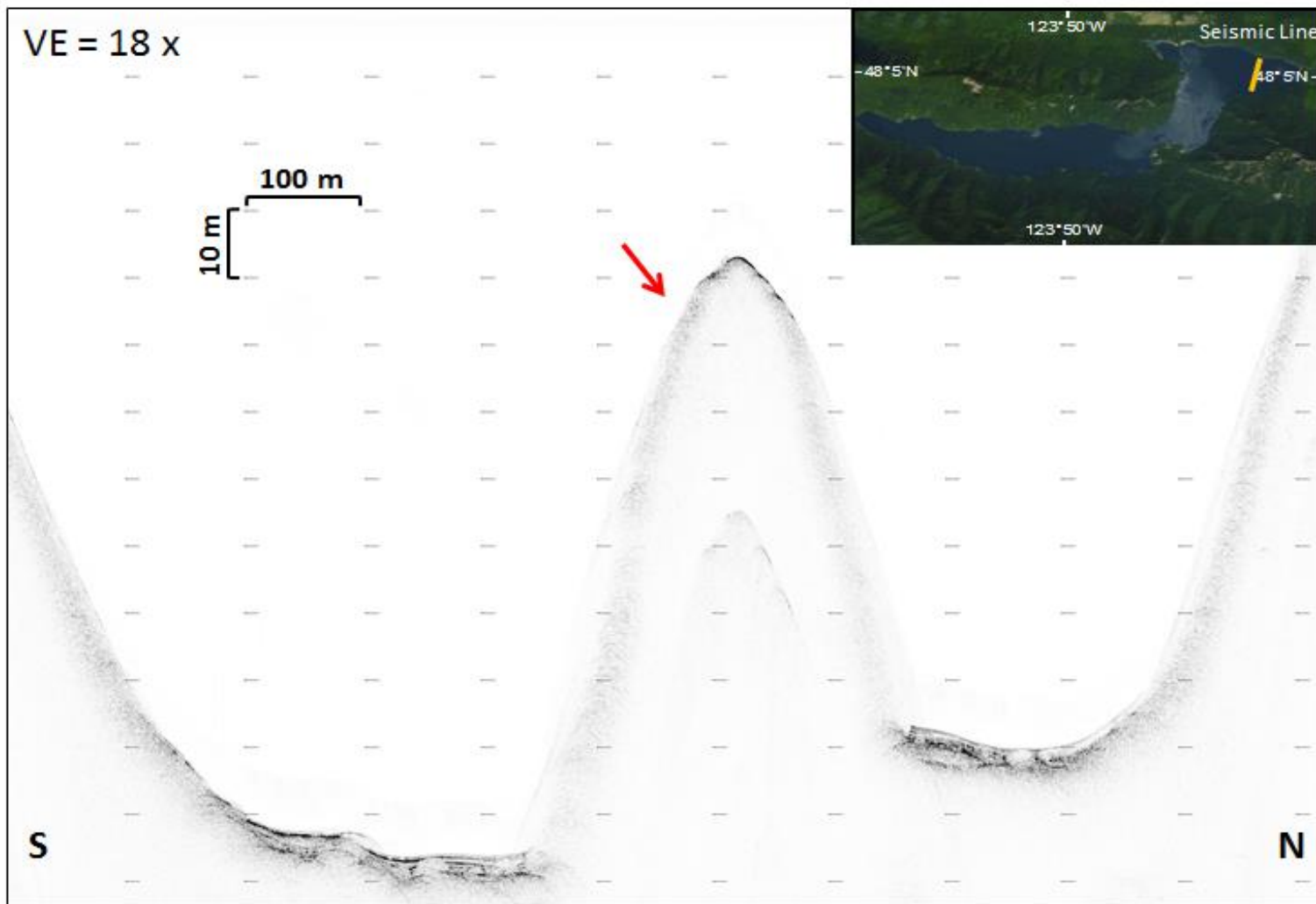


Figure 15. Seismic line from the eastern north basin (see map inset). The red arrow points to the large subaqueous rockslide deposit that has no intra-deposit depressions. The vertical exaggeration is 18x.



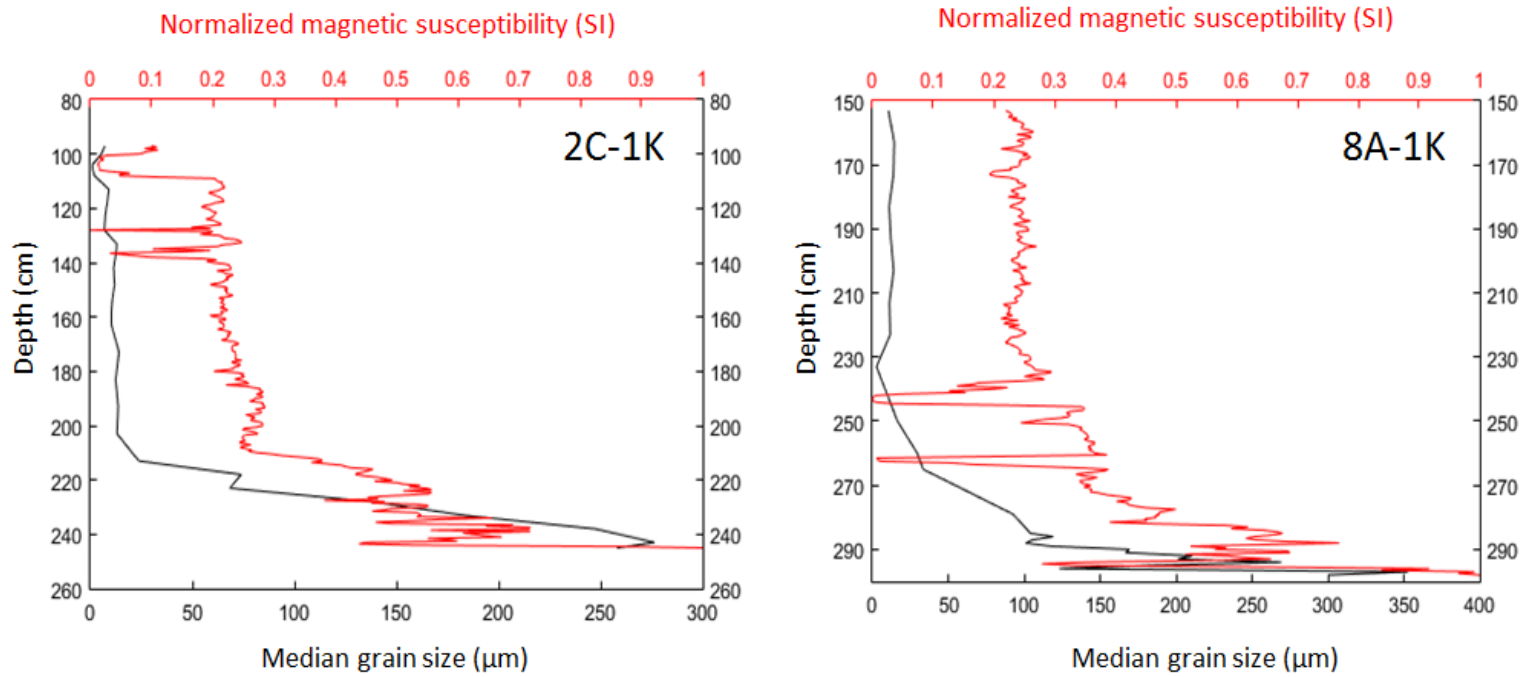


Figure 16. Down-core median particle size (μm) and normalized magnetic susceptibility (SI) profiles for the most recent EL1 layer in cores 2C-1K and 8A-1K. Magnetic susceptibility can be used as a proxy for median grain size due to the highly correlative relationship ($R=0.84$ for 2C-1K and $R=0.87$ for 8A-1K) of the two data sets.

Figure 17a. Down-core median grain size (μm) and normalized magnetic susceptibility (SI) profiles of the most recent EL1 layer in cores 4A-1K, 6A-1K, 7C-1K, and 9A-1K.

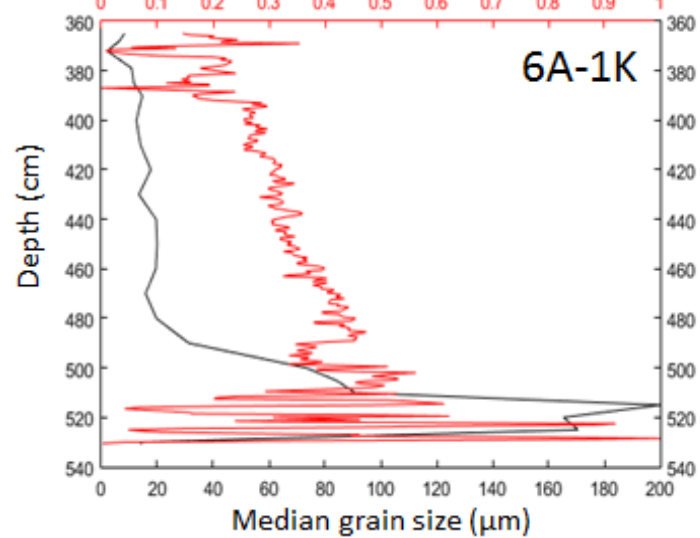
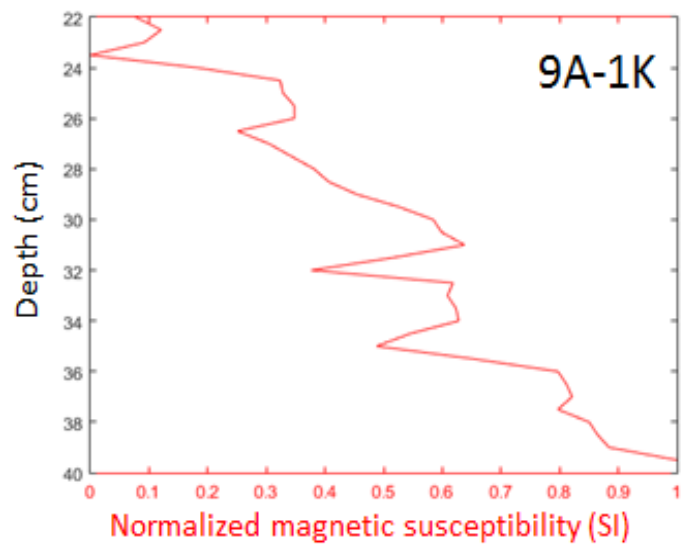
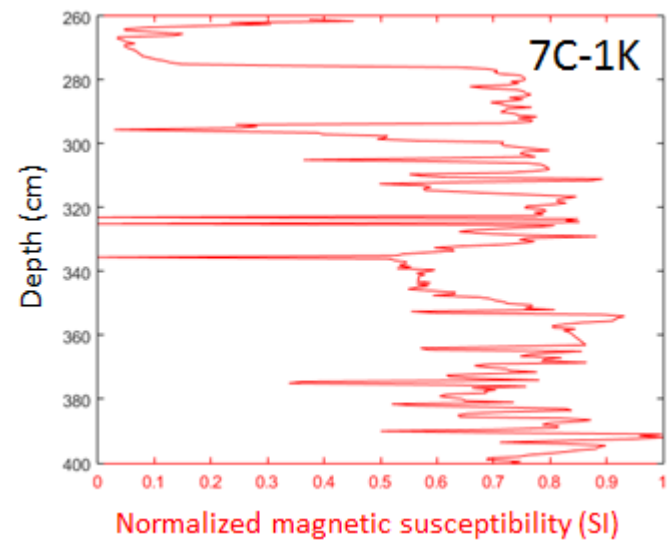
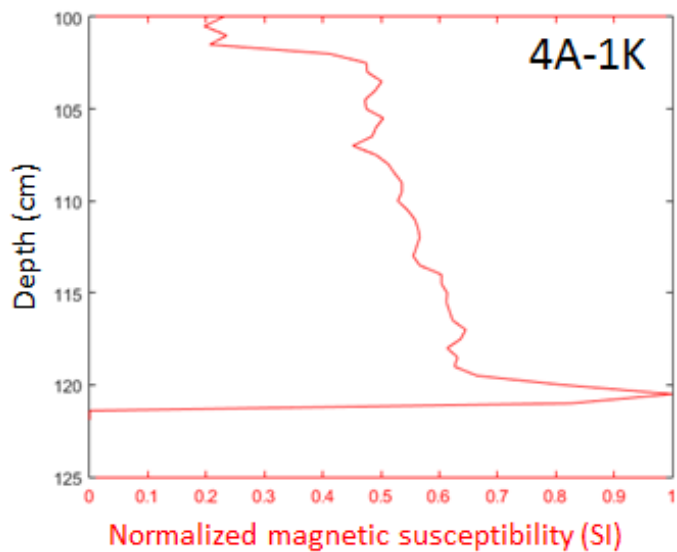
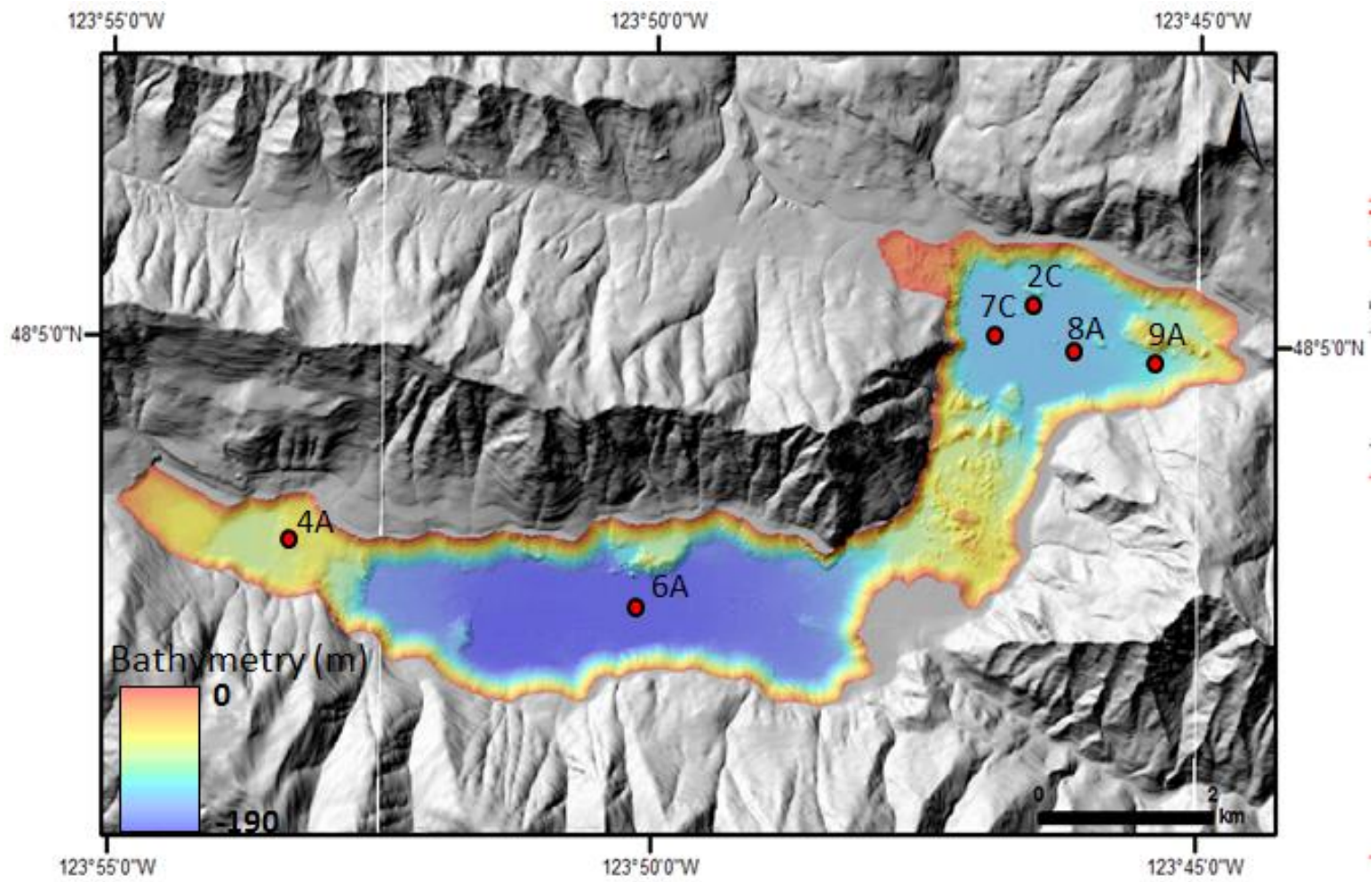


Figure 17b. Supplement to Figure 17a. Locations of cores 4A-1K, 6A-1K, 7C-1K, 2C-1K, 8A-1K, and 9A-1K on the 2.5 bathymetric grid surrounded by 10 m DEM topography (USGS, 2001).



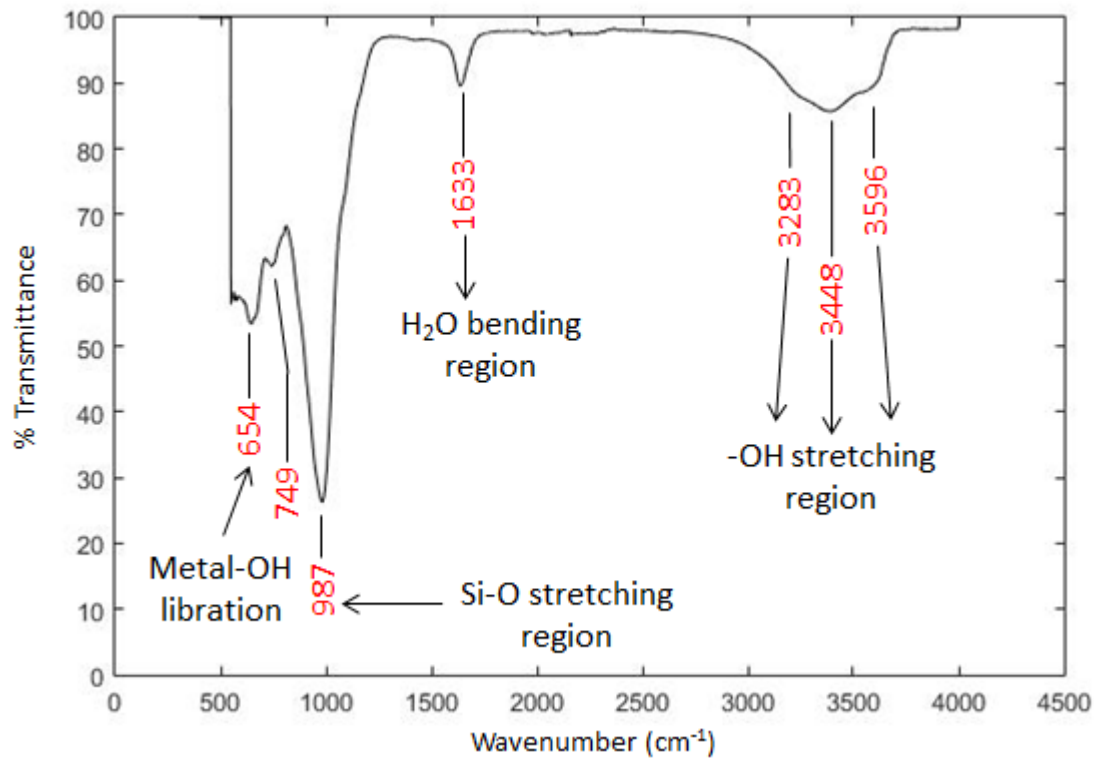


Figure 18. FTIR spectrum of chlorite found at the top of the EL1-A clay layer from core 6A-1K.

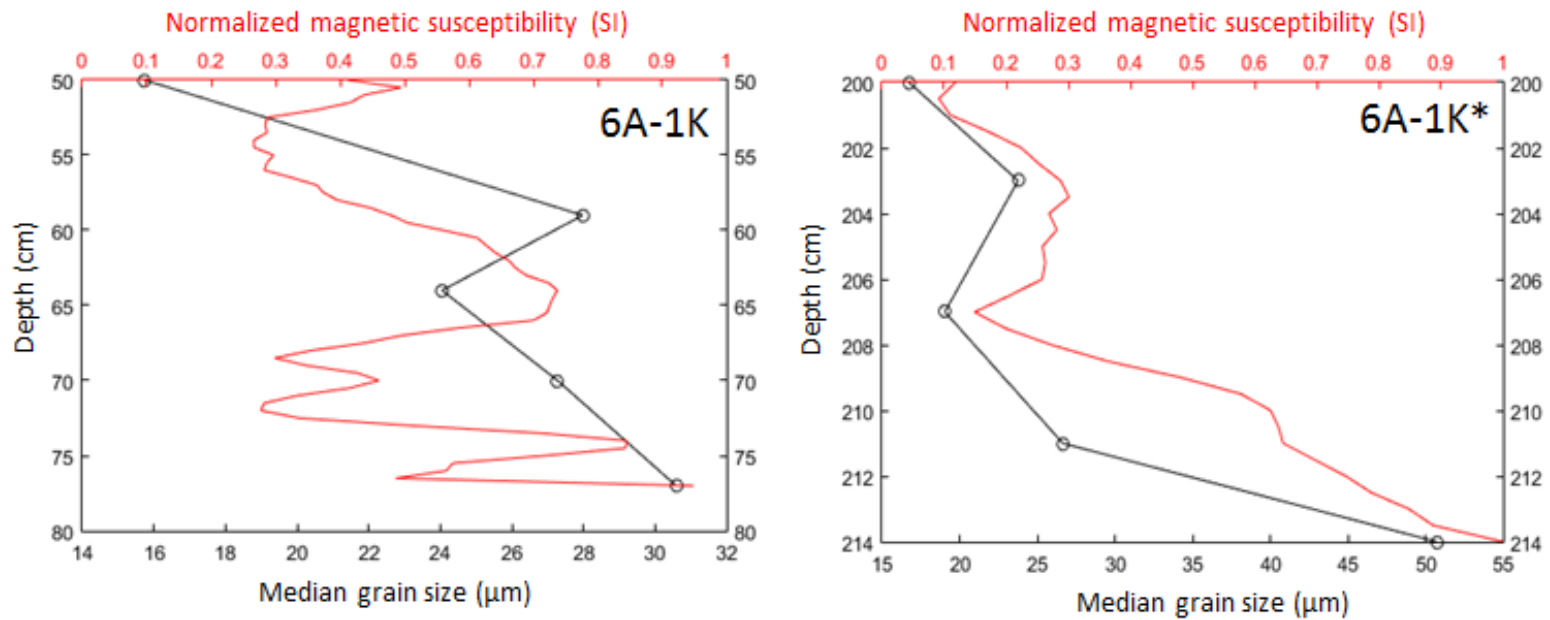


Figure 19. Down-core median particle size (μm) and normalized magnetic susceptibility (SI) profiles for two EL2 layers identified in core 6A-1K. The left profile (6A-1K) is from the interval 50-77 cm. The right profile (6A-1K*) is from the interval 200-214 cm.

Figure 20. Six core images of the EL1-A layer arranged from west to east across the lake. The EL1-A deposit consists of an erosively based, normally graded basaltic sand layer overlain in turn by massive, homogenous silt with dispersed plant debris and a clay cap interstratified with chloritic clay and basaltic sand laminations except in core 9A-1K, which lacks the laminations.

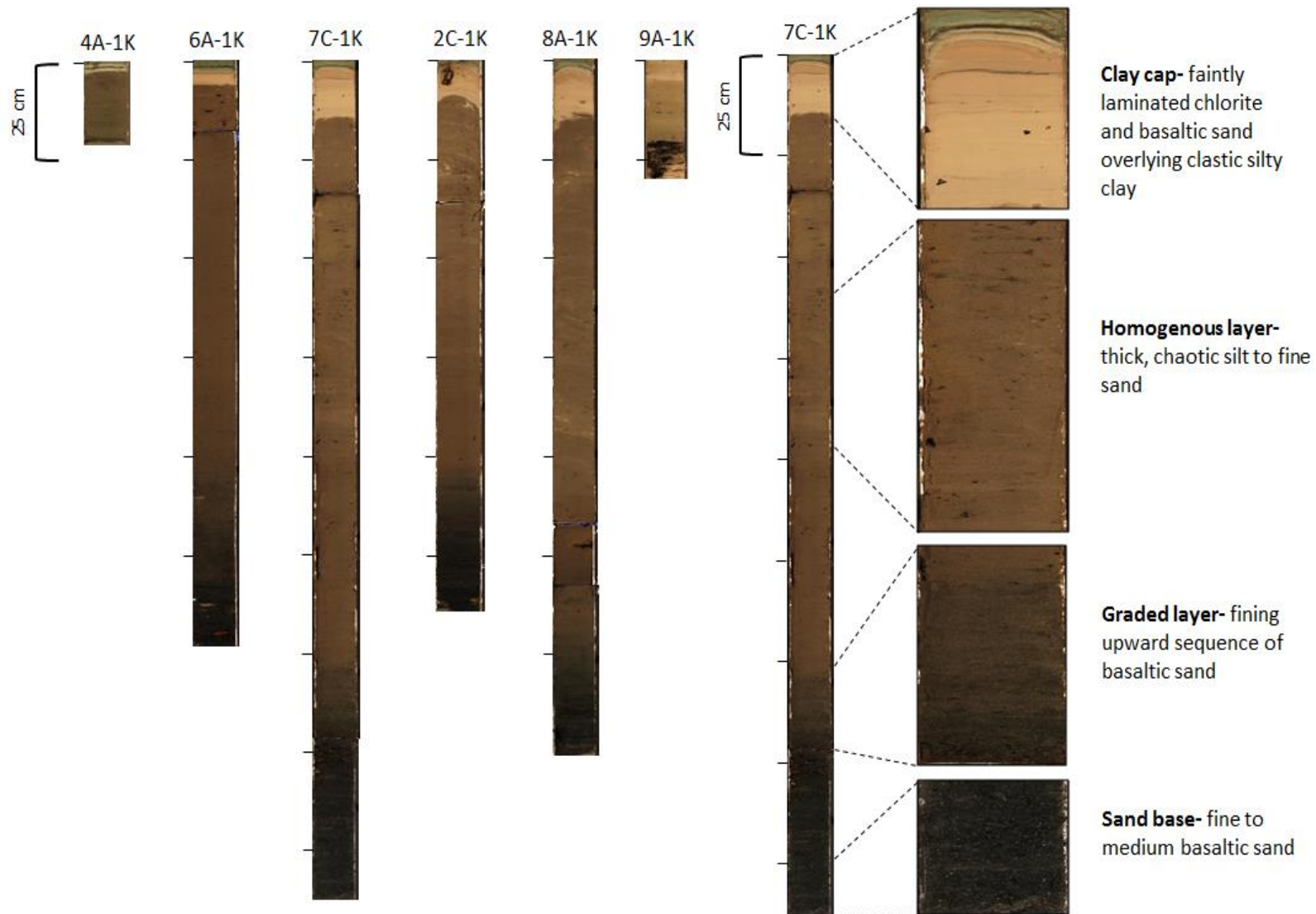


Figure 21. Three core images of the EL1-B layer arranged from west to east across the lake.

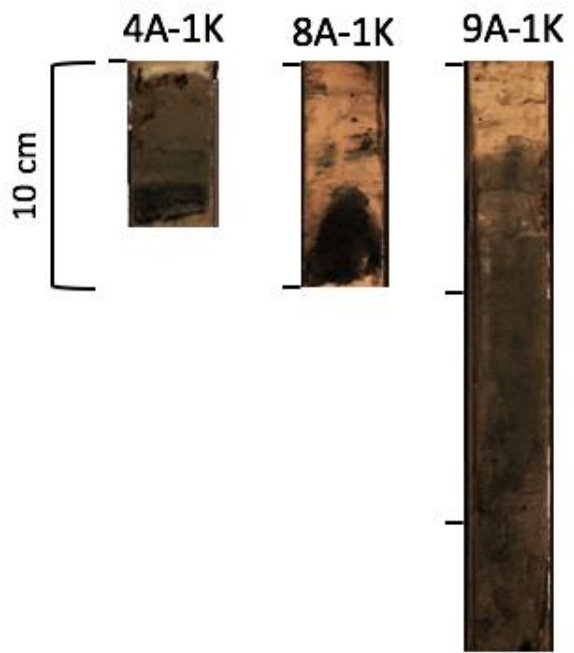
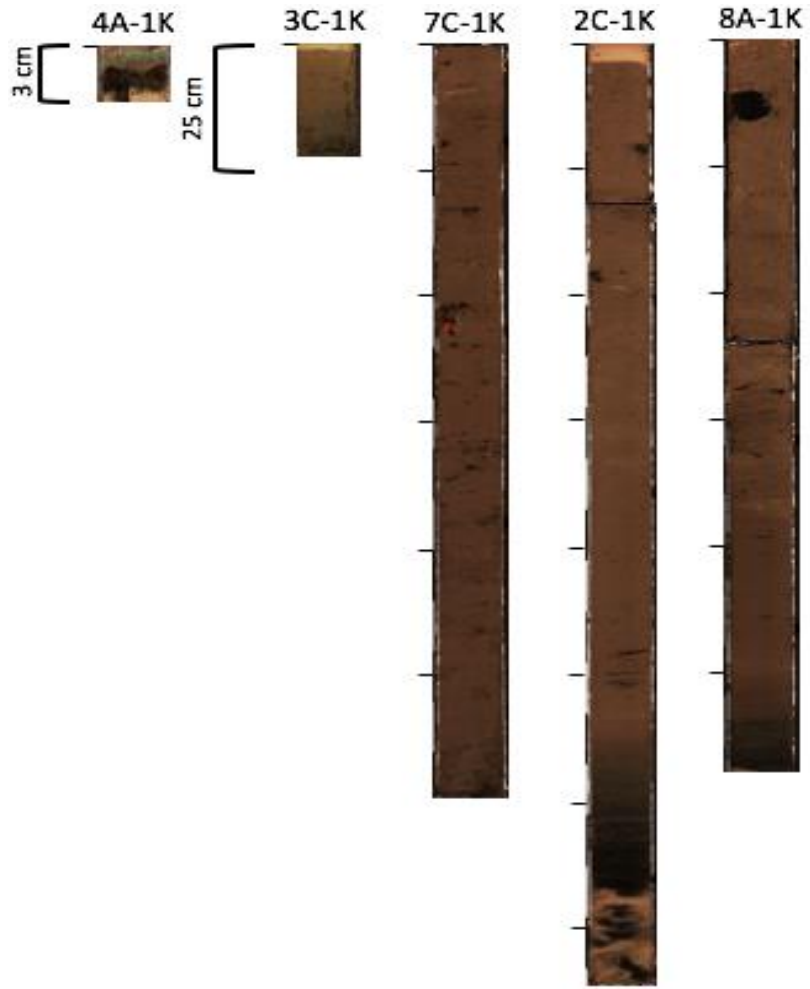


Figure 22. Five core images of the EL1-C layer arranged from west to east across the lake.



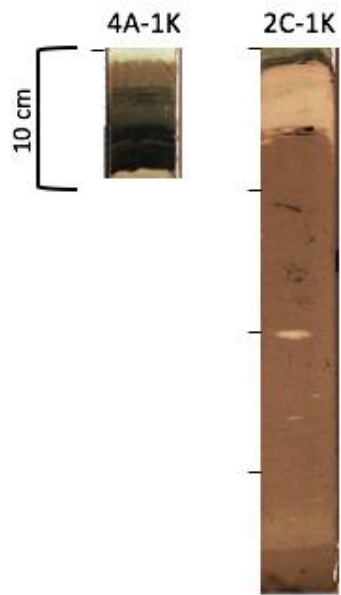


Figure 23. Two core images of EL1-D layer arranged from west to east across the lake. The deposit in core 2C-1K is only partially recovered.

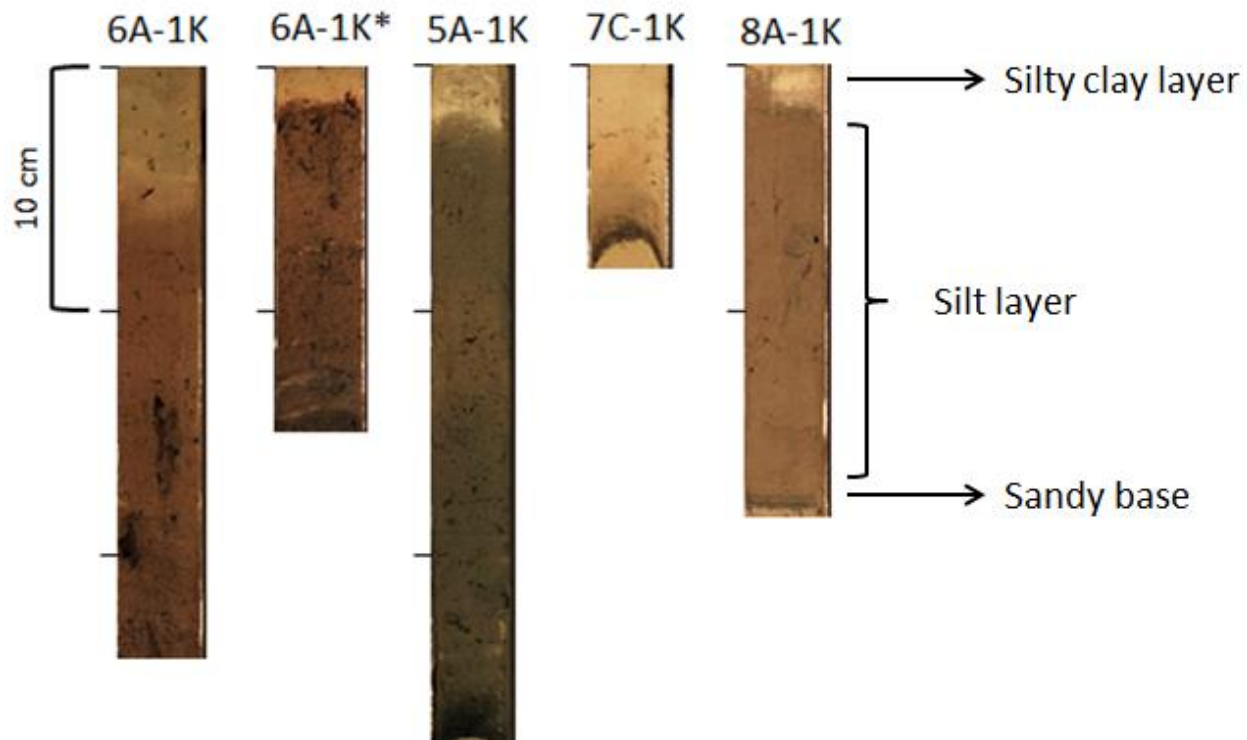
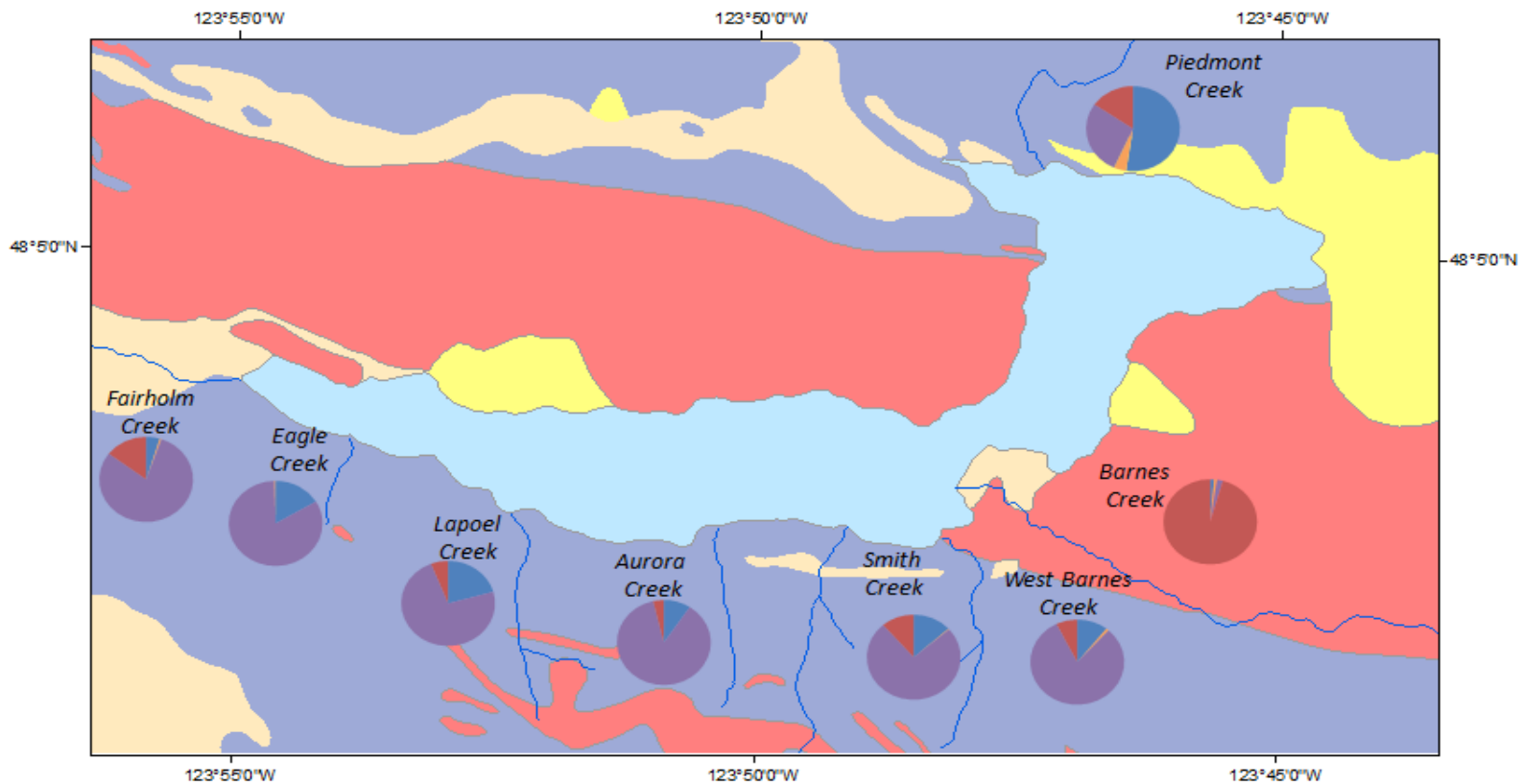


Figure 24. Five core images of EL2 deposits found in cores from the south (cores 5A-1K and 6A-1K) and north (cores 7C-1K and 8A-1K) basins. The EL2 deposits are characterized by a ≤ 4 cm thick sharp, erosive base of medium-grained basaltic sand and interspersed organic material that fines upward to a layer of homogenous dark brown to dark gray silt that is sometimes overlain by ≤ 4 cm thick light brown silty clay.

Figure 25. Simplified geologic map of the Lake Crescent area adapted from Schasse (2003) combined with petrologic results of stream “end member” sands.



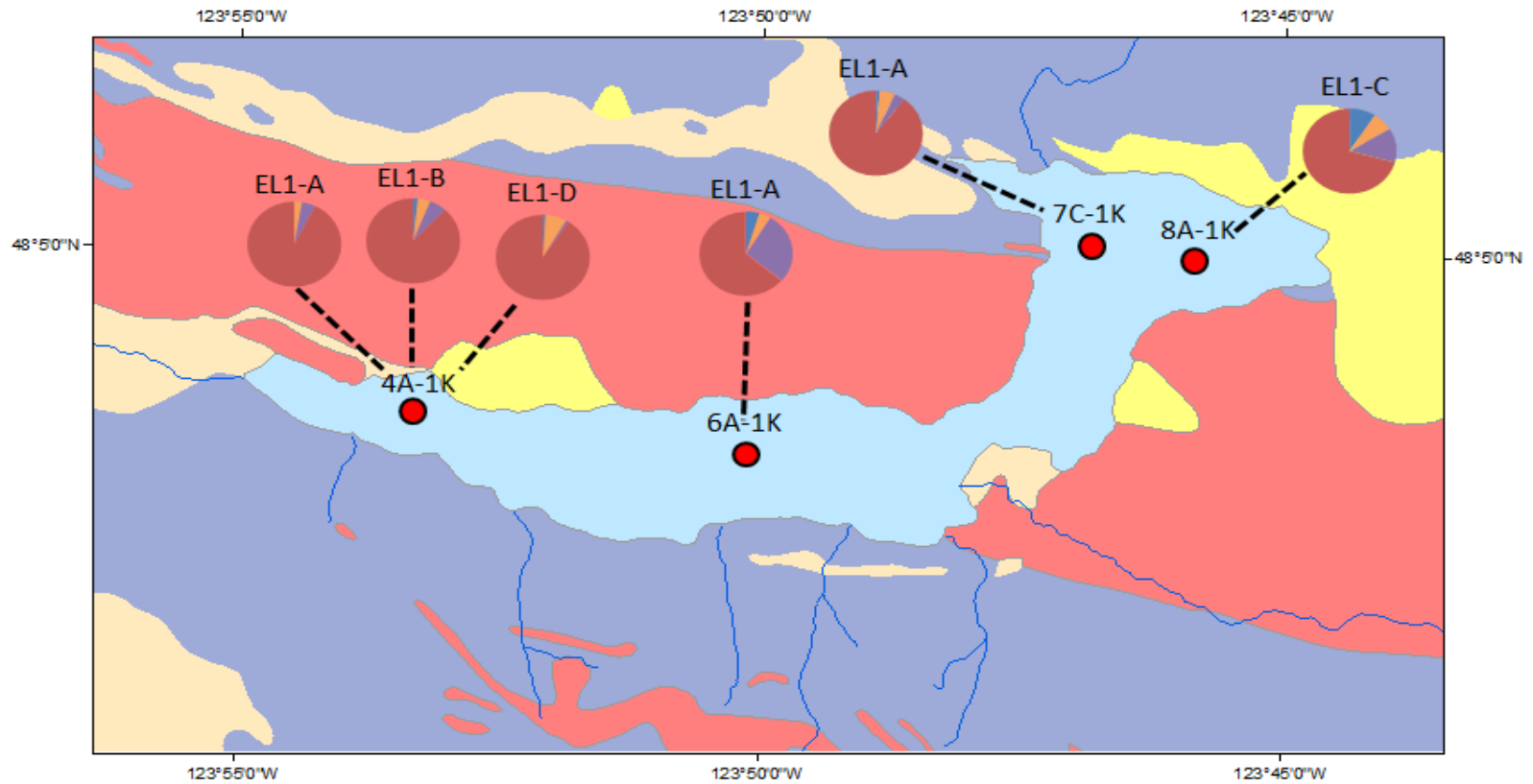
Sand Petrology Chart Legend

- Sedimentary Fragments
- Volcanic Fragments and Minerals
- Quartz
- Feldspar

Lithology Legend

- Sedimentary Rocks
- Volcanic Rocks
- Unconsolidated sediment
- Landslide Debris

Figure 26. Simplified geologic map of the Lake Crescent area adapted from Schasse (2003) combined with petrologic results of EL1 layer sands.



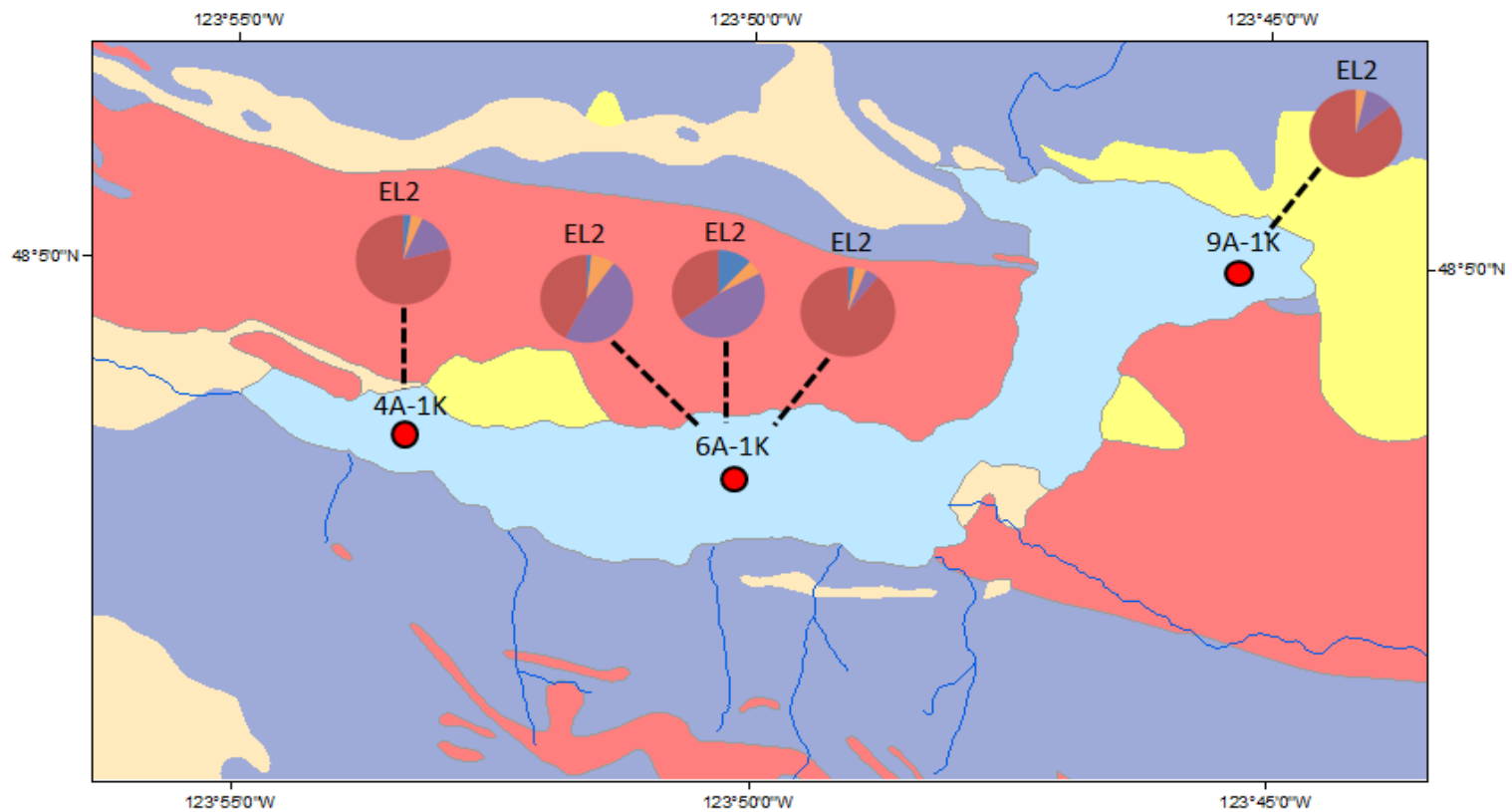
Sand Petrology Chart Legend

- Sedimentary Fragments
- Volcanic Fragments and Minerals
- Quartz
- Feldspar

Lithology Legend

- Sedimentary Rocks
- Volcanic Rocks
- Unconsolidated sediment
- Landslide Debris

Figure 27. Simplified geologic map of the Lake Crescent area adapted from Schasse (2003) combined with petrologic results of EL2 layer sands.



Sand Petrology Chart Legend

- Sedimentary Fragments
- Volcanic Fragments and Minerals
- Quartz
- Feldspar

Lithology Legend

- Sedimentary Rocks
- Volcanic Rocks
- Unconsolidated sediment
- Landslide Debris

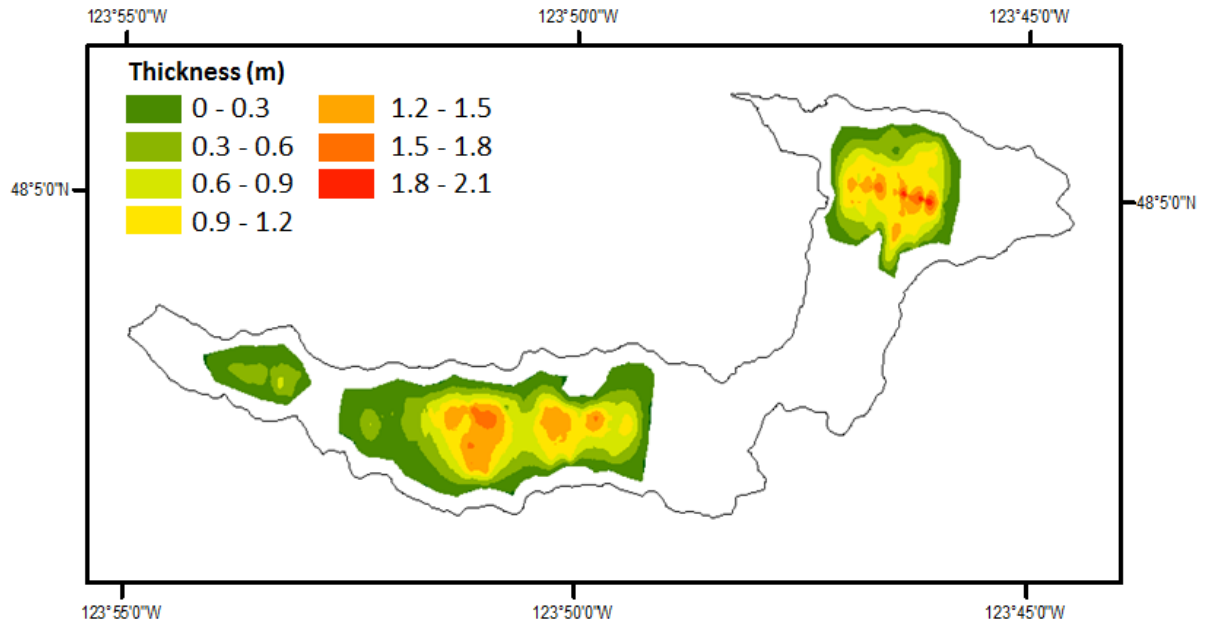


Figure 28a. Isopach map of the EL1-A sediment thickness in the north basin, south basin, and smaller south basin. The deposit is thickest in the north basin but occupies a larger area in the south basin.

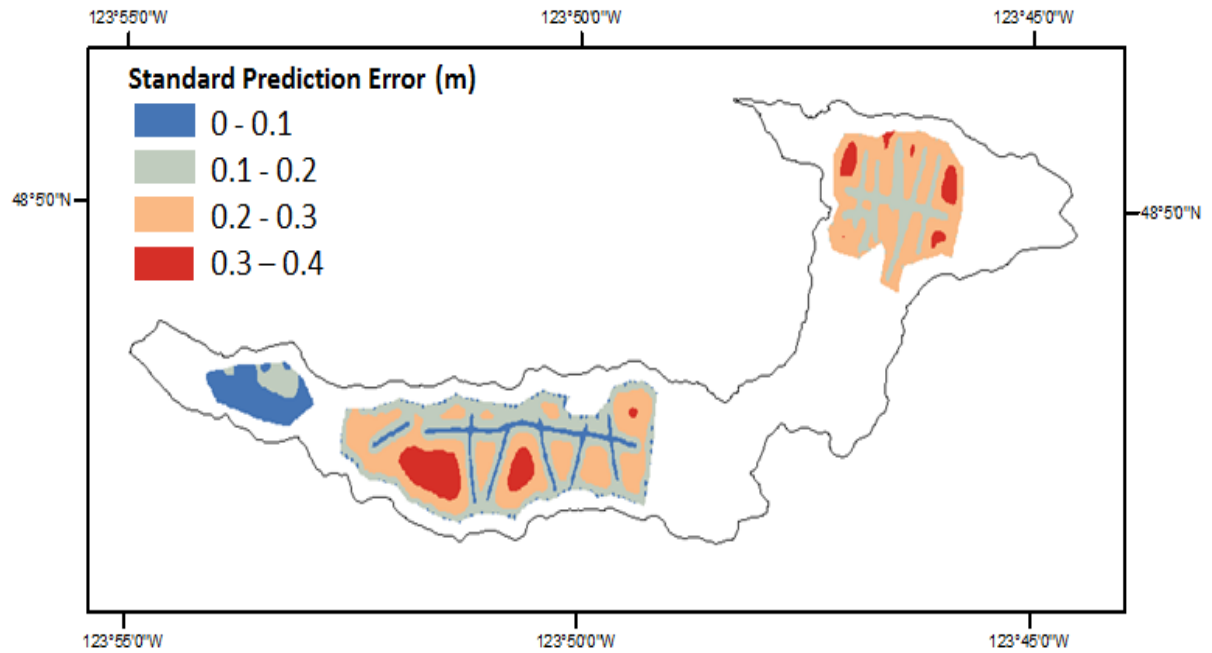
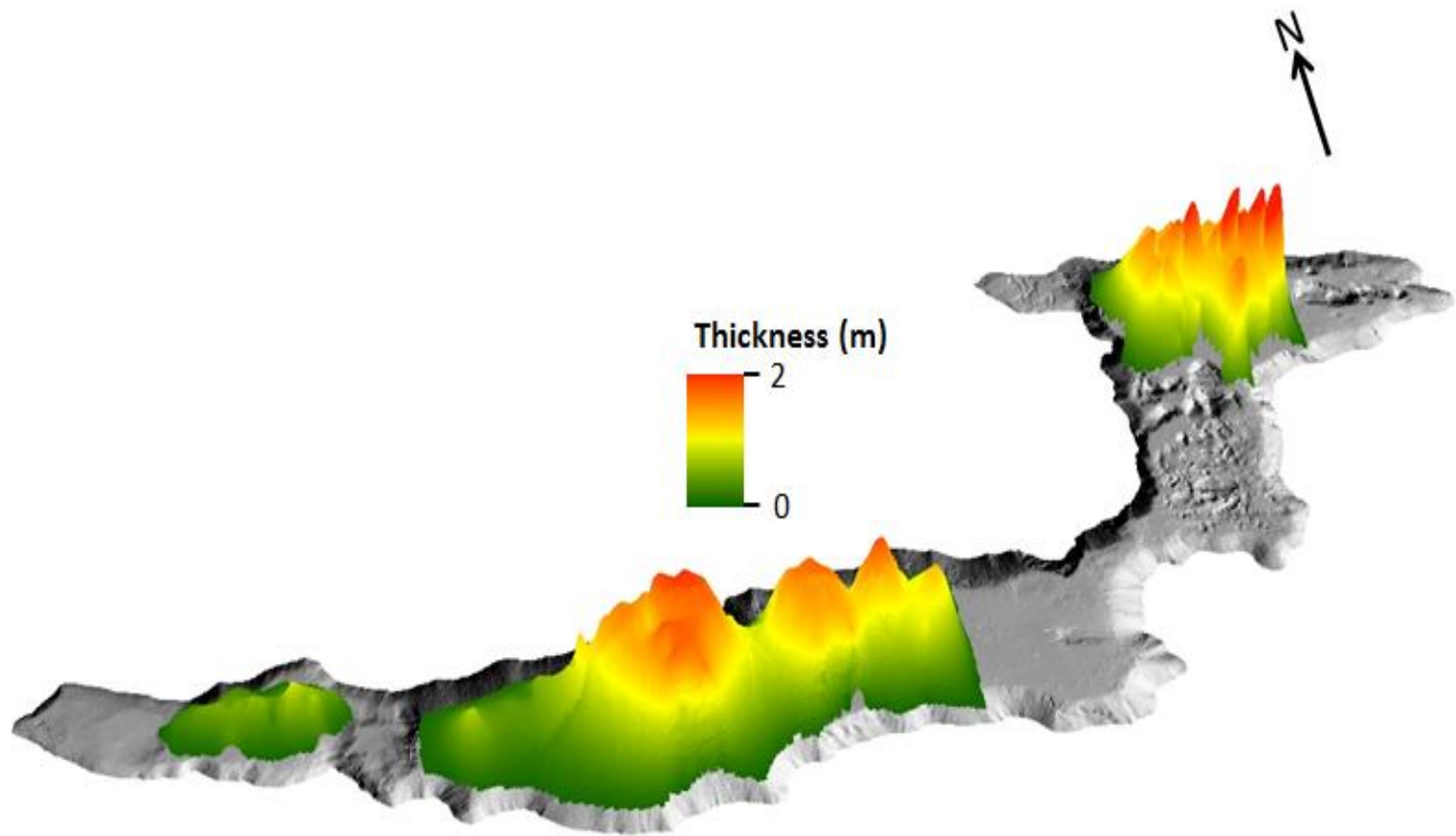


Figure 28b. Standard prediction error map associated with the interpolated sediment thickness of the EL1-A deposit. The error is lowest where the data is abundant.

Figure 29. 3-dimensional visualization of the EL1-A sediment thickness overlying the hillshade 2.5 resolution bathymetric grid. The deposit is thickest in the north basin but occupies a larger area in the south basin.



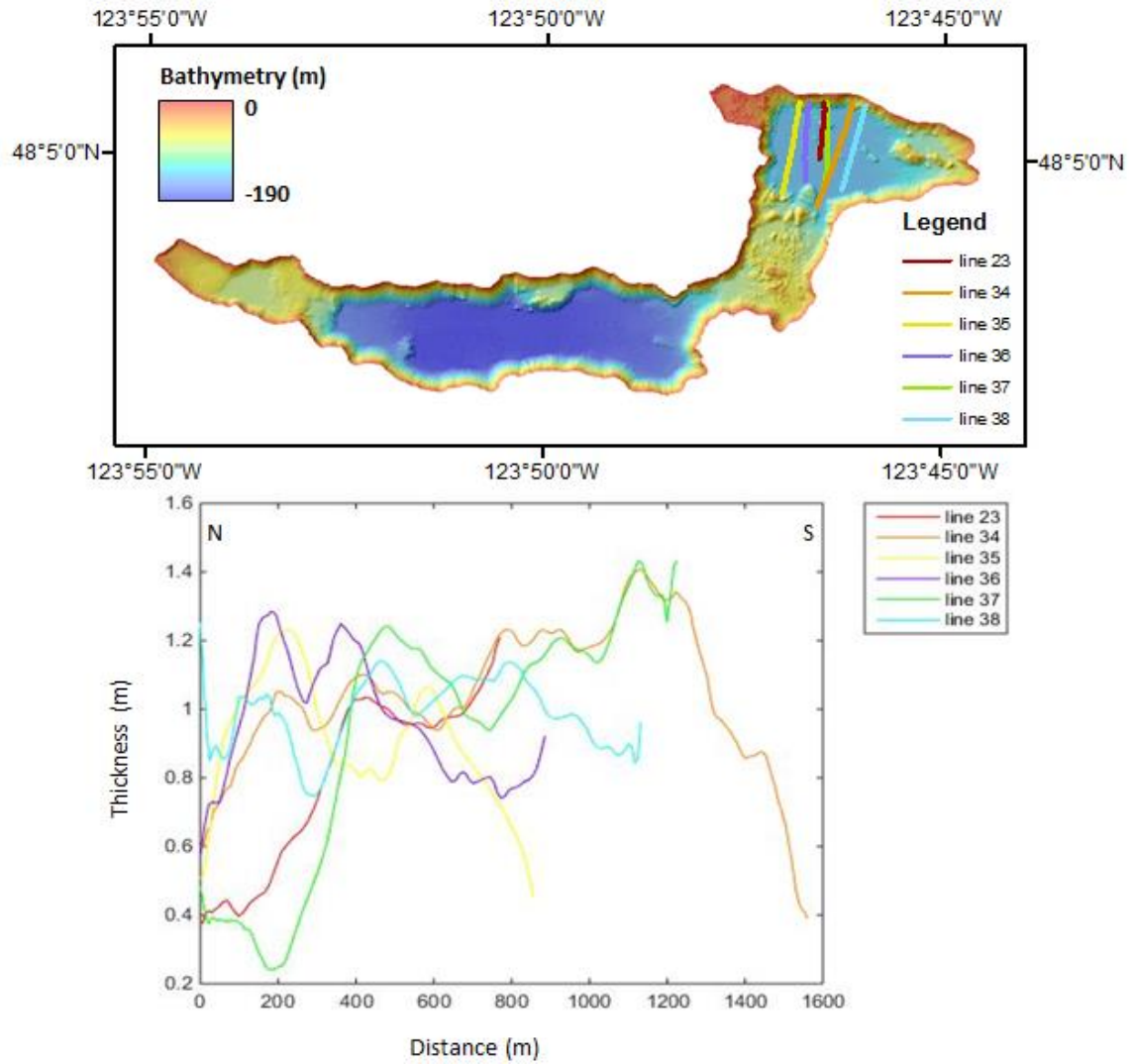


Figure 30. EL1-A sediment thickness profile generated from the interpolation of the layer thickness after it was digitized in seismic profiles. The sediment thickness profile demonstrates the sporadic concave upward shape of the EL1-A deposit in the north basin.

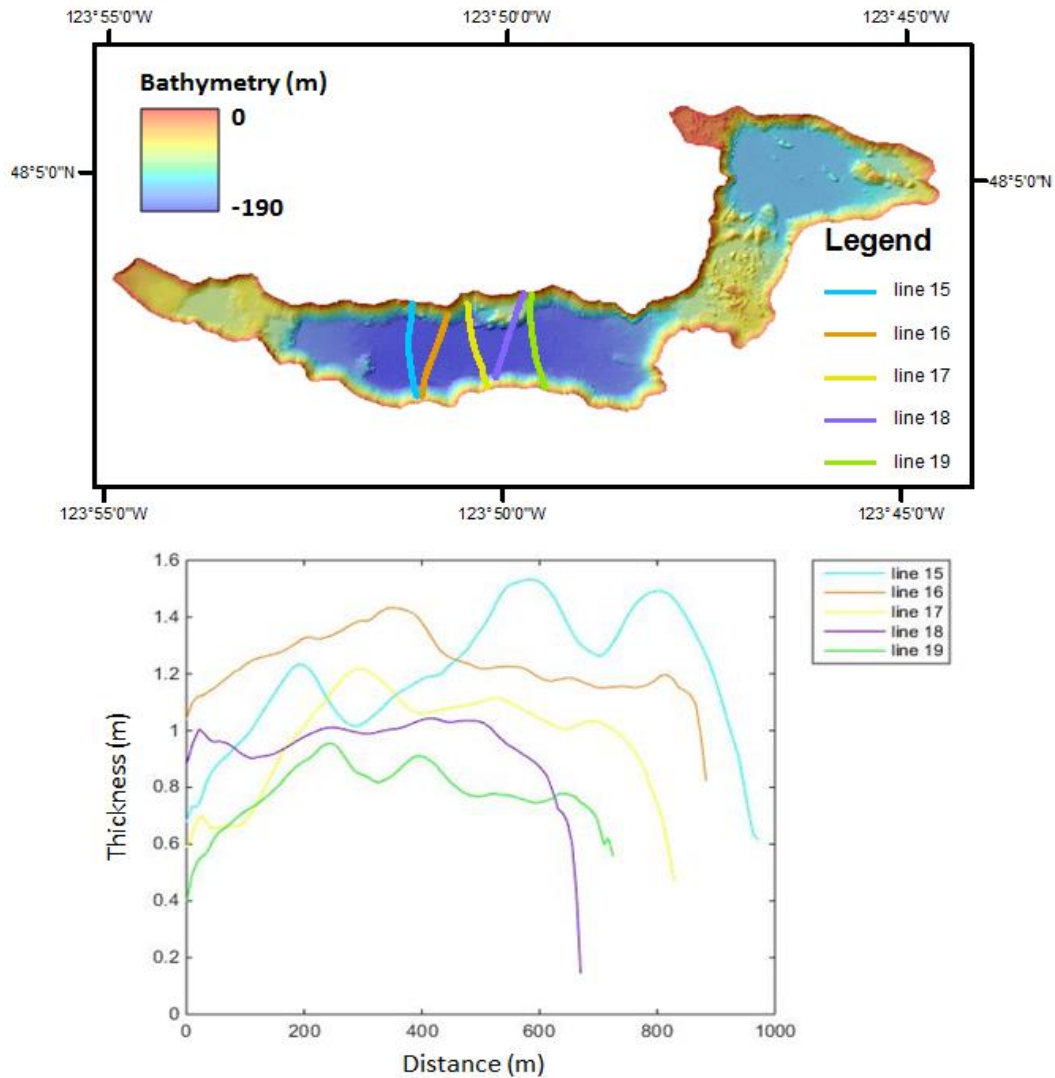


Figure 31. EL1-A sediment thickness profile generated from the interpolation of the layer thickness after it was digitized in seismic profiles. The sediment thickness profile demonstrates the smoother concave upward shape of the EL1-A deposit in the south basin.

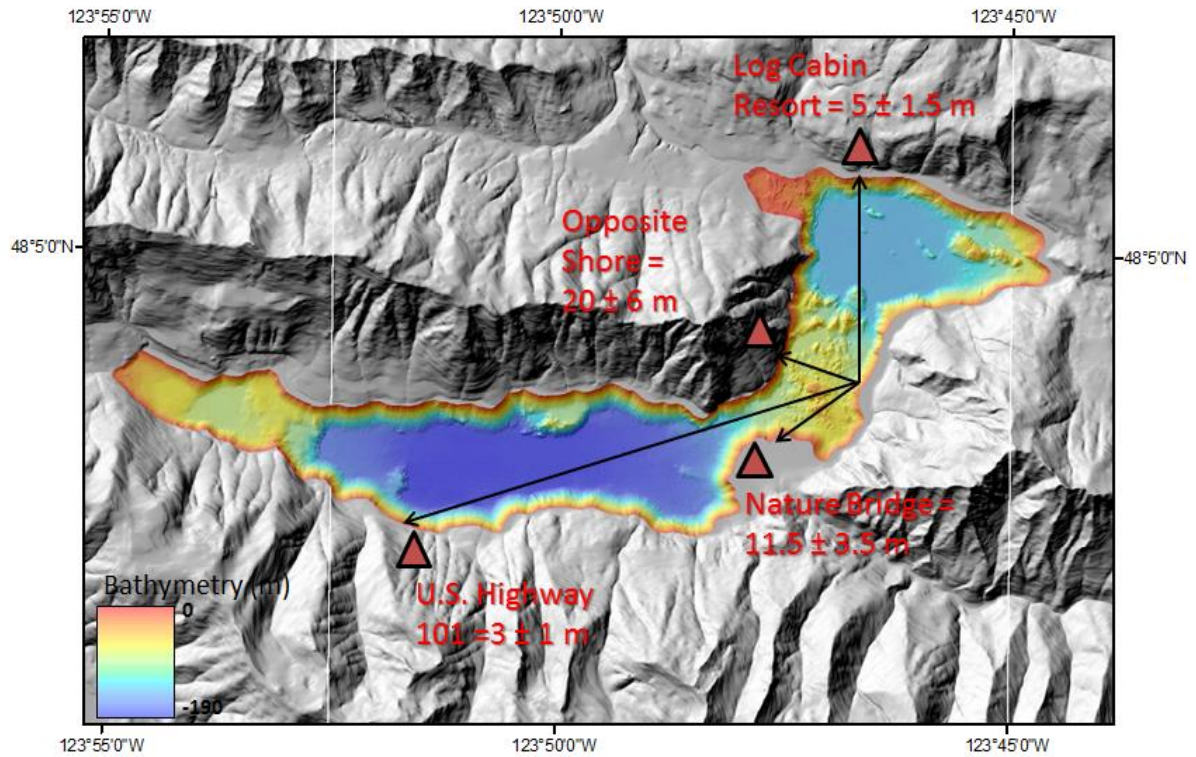


Figure 32. Straight line propagation distances (black arrows) of the displacement wave from where it enters the water to the shore at four locations (red triangles). Wave heights at each location are reported in red. Bathymetric grid has a resolution of 2.5 m, while the terrestrial DEM has a 10 m resolution (USGS, 2001).

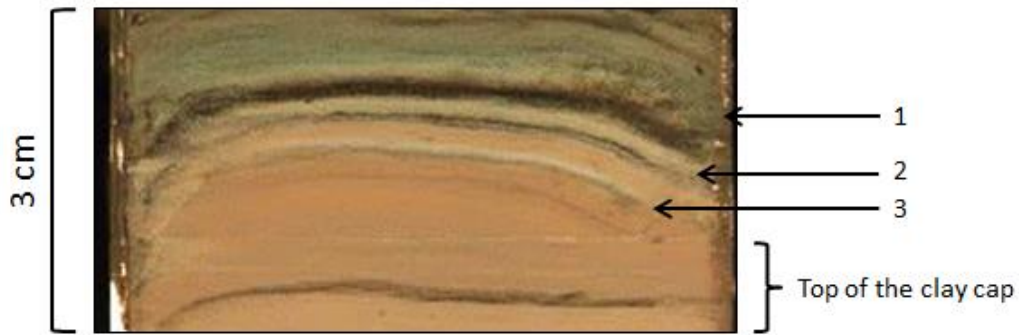


Figure 33. Three sequences of chloritic and basaltic laminations (1-3) superimposed on the clay cap in core 7C-1K. The interstratified laminations are only found at the tops of megaturbidites which are interpreted to be the mobilization of sediment from the subaerial portion of the exposed rockslide scarp during precipitation events in the years after the mass wasting event

Figure 34. Sediment core to seismic line correlation of core 2C-1K in the north basin (see map inset). EL1 deposits are annotated in red and outlined in orange. The approximate location of core 2C-1K is shown by the blue line. The purple arrow points to the irregular scour surface of EL1-A in the seismic line and core. The homogenous silt layer of the core correlates to the chaotic to transparent facies on the seismic line.

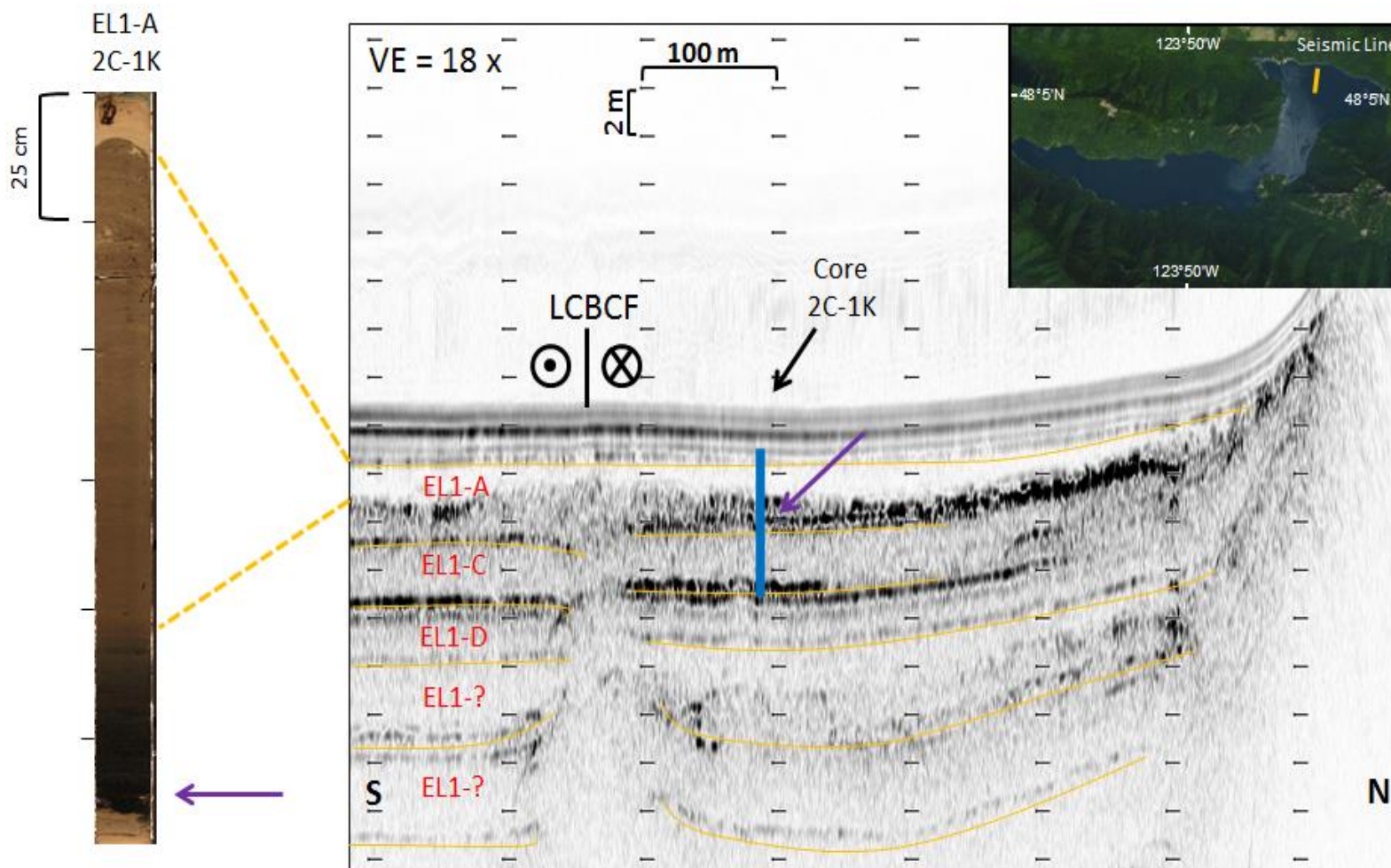
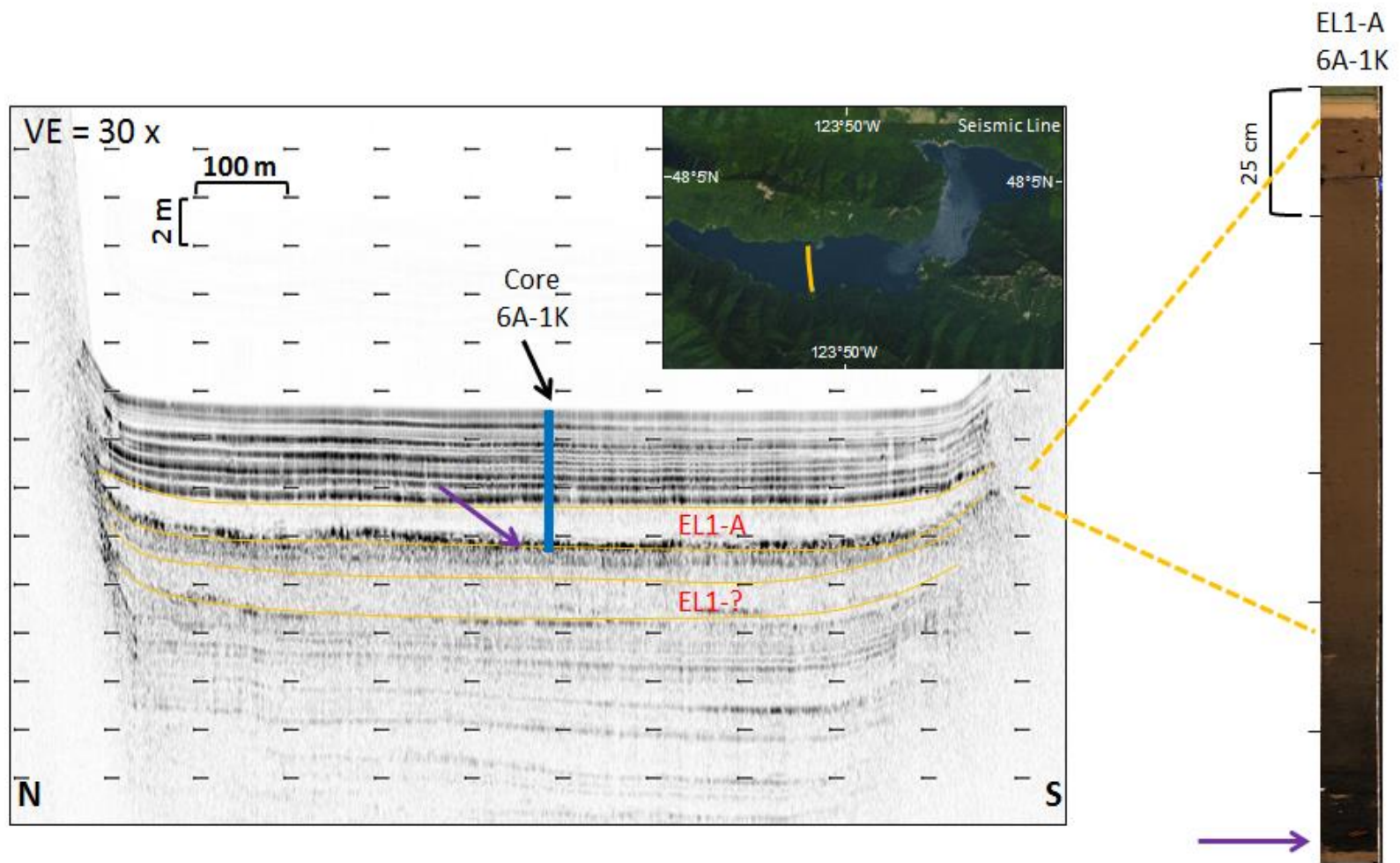


Figure 35. Sediment core to seismic line correlation of core 6A-1K in the south basin (see map inset). EL1 deposits are annotated in red and outlined in orange. The approximate location of core 6A-1K is shown by the blue line. The purple arrow points to the smoother scour surface of EL1-A in the seismic line and core. The homogenous silt layer of the core correlates to the chaotic to transparent facies on the seismic line.



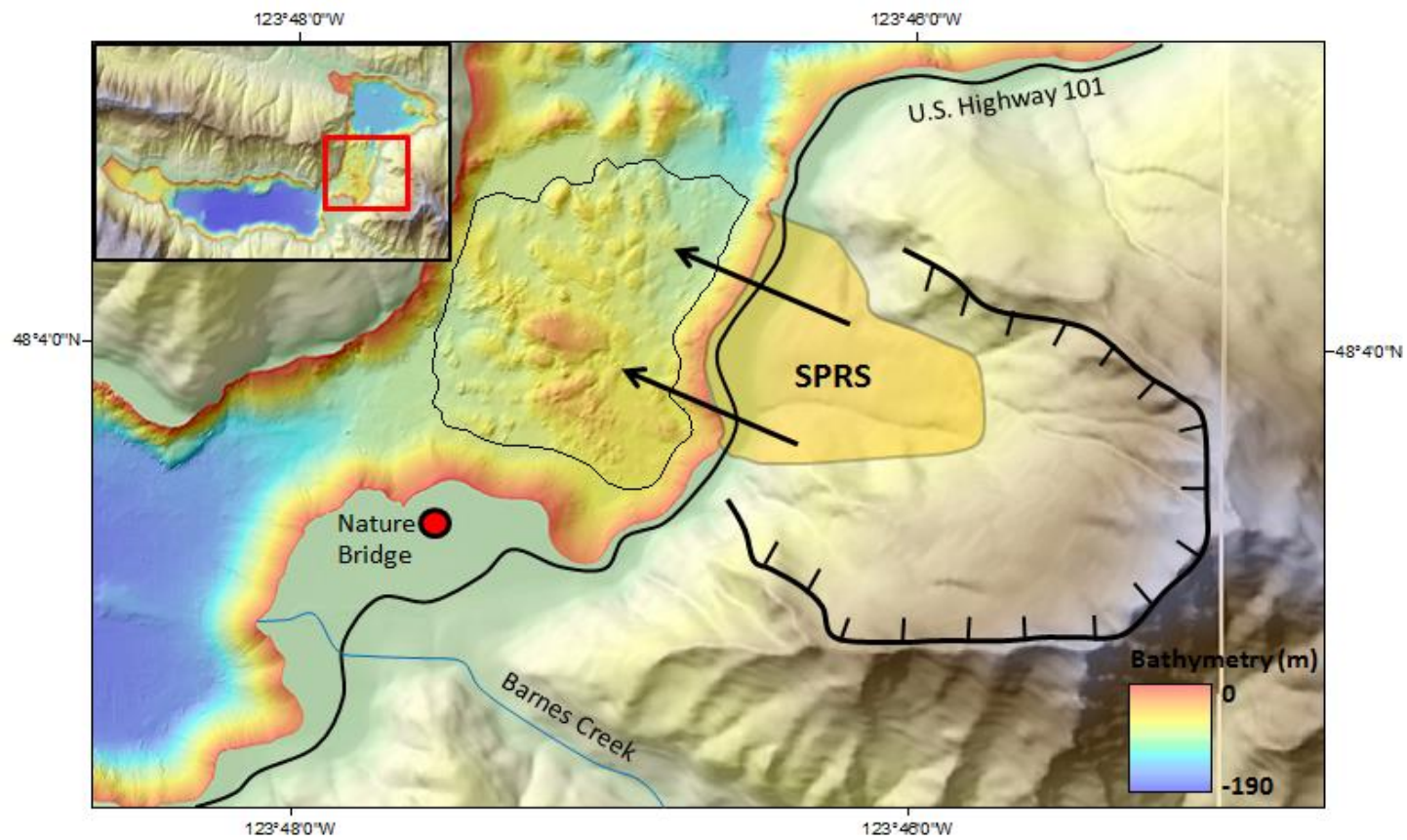


Figure 36. The onshore Sledgehammer Point rockslide (SPRS) is shaded yellow and the subaqueous portion is outlined in black. The hachures point down scarp. The arrows indicate the direction of movement. Bathymetric grid has a resolution of 2.5 m, while the terrestrial DEM has a 10 m resolution (USGS, 2001).

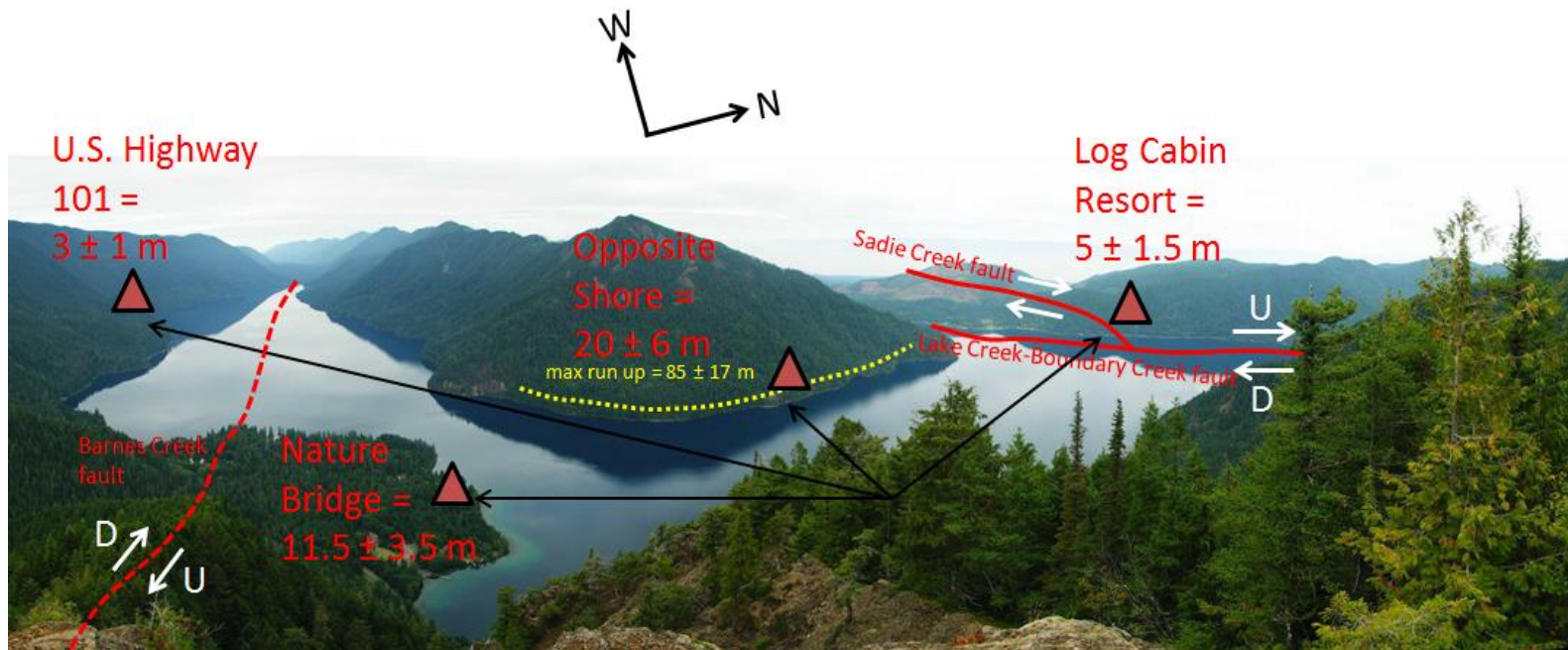


Figure 37. Photograph (Hiller, 2008) take from Mt. Storm King (opposite shore to Pyramid Peak) that shows the straight line propagation distances (black arrows) of the displacement wave from where it enters the water to the shore at four locations (red triangles). Wave heights at each location are reported in red. The maximum wave run up on the opposite shore is outlined in yellow. The Sadie Creek, Lake Creek-Boundary Creek, and Barnes Creek faults are drawn in red. Right lateral motion is indicated by the white arrows. Vertical motion is indicated by U (up) and D (down).

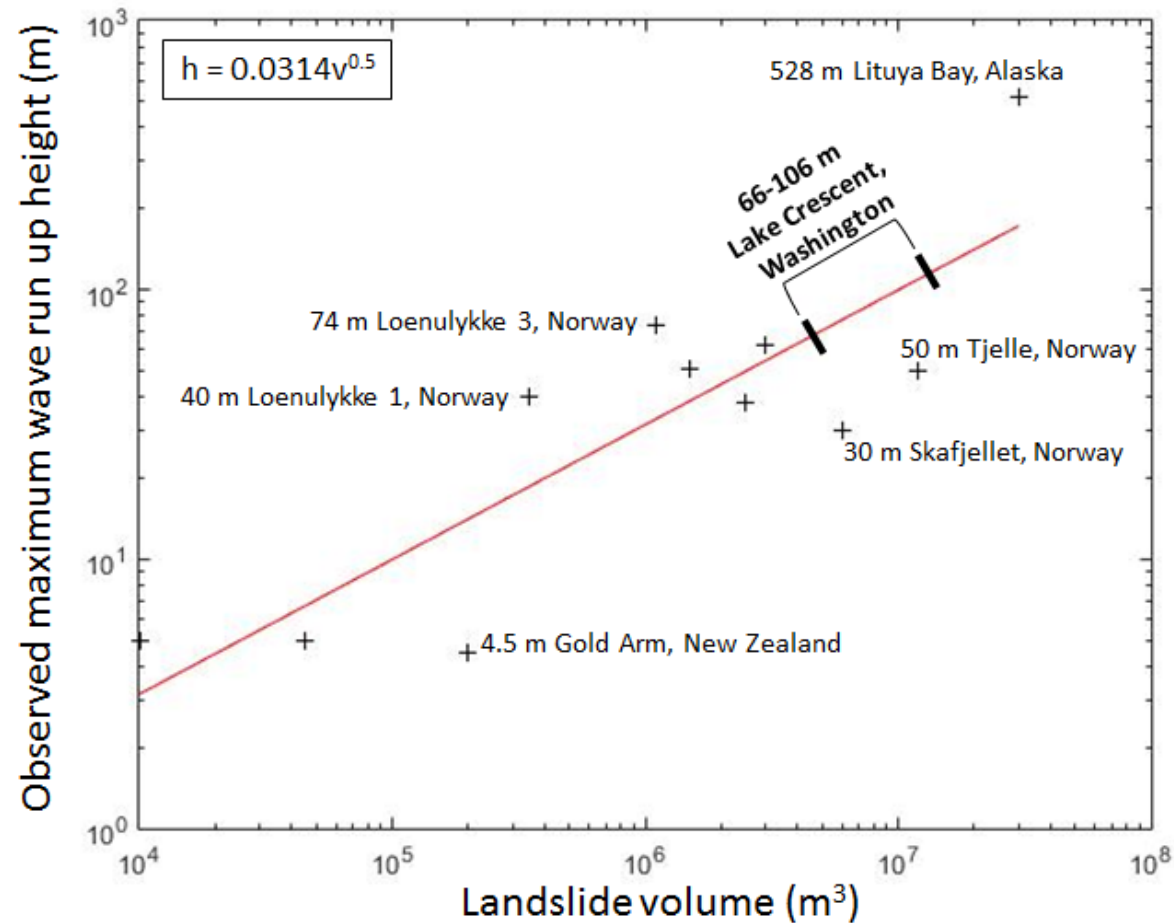


Figure 38. Maximum wave run up height versus landslide volume graph adapted from Clark et al. 2015 showing historical landslide generated displacement wave run up (see Table 14 for data) used to derive possible run up during the Sledgehammer Point rockslide (range highlighted by black brackets). The correlation coefficient for the maximum wave run up height and landslide volume is $R = 0.84$.

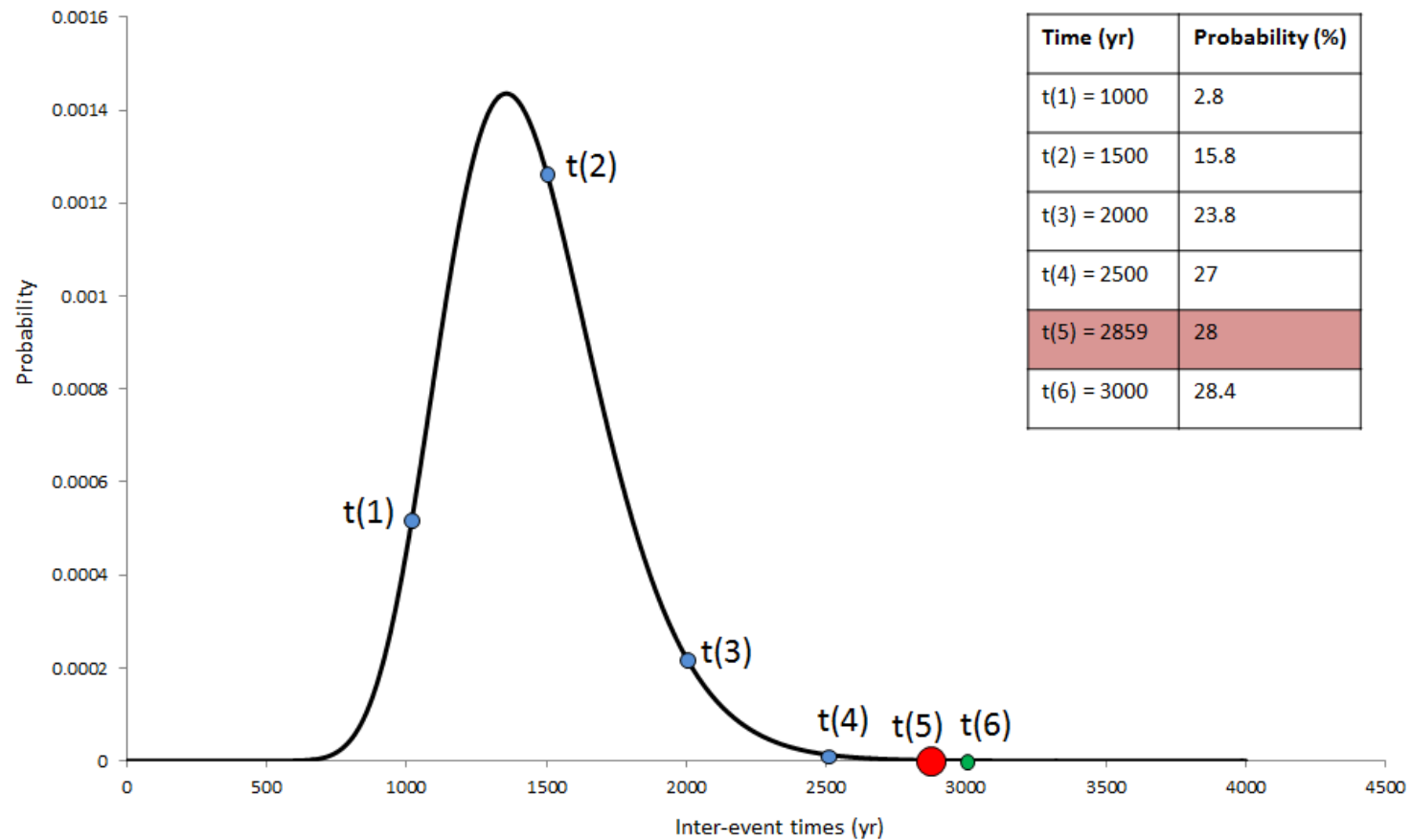


Figure 39. Lognormal probability density distribution of earthquake recurrence on the Lake Creek-Boundary Creek fault. The blue circles of t(1-4) indicate time that has already passed for demonstrative purposes. The red circle of t(5) is the time since the last earthquake (the age of megaturbidite EL1-A). The green circle of t(6) indicates future time. Probability of an earthquake occurring at each time is listed in the adjacent table. The current probability of an earthquake occurring on the Lake Creek-Boundary Creek fault is shaded in red.

REFERENCES

- Atwater, B.F., 1987, Evidence for great Holocene earthquakes along the outer coast of Washington state: *Science*, v. 236, p. 942-944.
- Atwater, B.F. and Hemphill-Haley, E., 1997, Recurrence intervals for great earthquakes of the past 3,500 years at northeastern Willapa Bay, Washington: U.S. Geological Survey Professional Paper 1576, 108 p.
- Atwater, B.F. and Moore, A.L., 1992, A tsunami about 1000 years old in the Puget Sound, Washington: *Science*, v. 258, p. 1614-1617.
- Atwater, B.F. and Yamaguchi, D.K., 1991, Sudden, probably coseismic submergence of Holocene trees and grass in coastal Washington state: *Geology*, v. 19, p. 706-709.
- Babcock, R.S., Suczek, C.A., and Engebretson, D.C., 1994, The Crescent "Terrane", Olympic Peninsula and Southern Vancouver Island: Washington Division of Geology and Earth Resources Bulletin 80, p. 141-157.
- Beck, C., 2009, "Late Quaternary lacustrine paleo-seismic archives in north-western Alps: Examples of earthquake-origin assessment of sedimentary disturbances: *Earth-Science Reviews*, v. 96, p. 327-344.
- Blikra, L.H., Longva, O., Harbitz, C. and Lovhølt, F., 2005, Quantification of rock-avalanche and tsunami hazard in Storfjorden, western Norway. In: Senneset, K., Flaate, K. and Larsen, J.O. (Editors), *Landslides and Avalanches: ICFL 2005 Norway*. Taylor & Francis Group, London, p. 57-63.
- Bouma, A.H., 1987, Megaturbidite- an acceptable term: *Geology Marine Letters*, v. 7, p. 63-67.
- Brandon, M.T. and Calderwood, A.R., 1990, High-pressure metamorphism and uplift of the Olympic subduction complex: *Geology*, v.18, 1252-1255.
- Brandon, M.T., Roden-Tice, M.K., and Garver, J.I., 1998, Late Cenozoic exhumation of the Cascadia accretionary wedge in the Olympic Mountains, northwest Washington State: *Geological Society of America Bulletin* 110, p. 985-1009.
- Brenkman, S.J., Duda, J.J., Kennedy, P.R., and Baker, B.M., 2014, A legacy of divergent fishery management regimes and the resilience of rainbow and cutthroat trout populations in Lake Crescent, Olympic National Park, Washington: *Northwest Science*, v. 88, p. 280-304.
- Chapron, E., Beck, C., Pourchet, M., and Deconinck, J.F., 1999, 1822 earthquake-triggered homogenite in Lake Le Bourget (NW Alps): *Terra Nova*, v. 11, p. 86-92.

Cita, M.B. and Alosi, G., 2000, Deep-sea tsunami deposits triggered by the explosion of Santorini (3500y BP), eastern Mediterranean: *Sedimentary Geology*, v. 135, p. 181-203.

Clallam County, Washington, 2016, Map Data Streams:
<http://www.clallam.net/Maps/mapdata.html> (accessed June 2016).

Clark, E.A., 1953, *Indian Legends of the Pacific Northwest*. Berkley and Los Angeles, California: University of California Press, 225 p.

Clark, K.J., Upton, P., Carey, J., Rosser, B., and Strong, D., 2015, *Tsunami and Seiche Hazard Scoping Study for Lakes Tekapo, Pukaki, Ohau, Alexandrina and Ruataniwha*: Environment Canterbury Regional Council Report No. R15/39, 69 p.

Clowes, R.M., Baird, D.J., and Dehler, S.A., 1997, Crustal structure of the Cascadia subduction zone, southwestern British Columbia, from potential field and seismic studies: *Canadian Journal of Earth Science*, v. 34, p. 317-335.

Cysat, R., 1601, *Collectanea Chronica und denkwürdige Sachen pro Chronica Lucernensi et Helvetiae*, in Schmid, J., *Quellen und Forschungen zur Kulturgeschichte von Luzern und der Innerschweiz*, Volume 1: Luzern, Diebold Schilling Verlag, p. 882-888.

Dadson, S.J., Hovius, N., Chen, H., Dade, W.B., Lin, J.C., Hsu, M.L., Lin, C.W., Horng, M.J., Chen, T.C., Milliman, J., and Stark, C.P., 2004, Earthquake-triggered increase in sediment delivery from an active mountain belt: *Geology*, v. 32, no. 8, p. 733-736.

Dethier, D., Pessl, F., Keuler, R., Balzarini, M., and Pevear, D., 1995, Late Wisconsinan glaciomarine deposition and isostatic rebound, northern Puget Lowland, Washington: *Geological Society of America Bulletin* 107, p. 1288-1303.

Dickinson, W., 1970, Interpreting detrital modes of graywacke and arkose: *Journal of Sedimentary Petrology*, v. 40, p. 695-707.

Dietrich, W.E., 1982, Settling Velocity of Natural Particles: *Water Resources Research*, v. 18, p. 1615-1626.

Dragovich, J.D., Logan, R.L., Schasse, H.W., Walsh, T.J., Lingley, W.S., Jr., Norman, D.K., Gerstel, W.J., Lapen, T.J., Schuster, J.E., and Meyers, K.D., 2002, *Geologic map of Washington—Northwest quadrant*: Washington Division of Geology and Earth Resources Geologic Map GM-50, 72 pp. pamphlet, 3 sheets, scale 1:250,000.

Engbretson, D.C., Cox, A., and Gordon, R.G., 1985, Relative motion between oceanic and continental plates in the Pacific basin: *Geological Society of America Special Paper*, v. 206, 59 pp.

Evans, S.G., 1989, The 1946 Mount Colonel Foster rock avalanche and associated displacement wave, Vancouver Island, British Columbia: *Canadian Geotechnical Journal*, v. 26, no. 3, p. 447-452.

Evers, F.M., Hager, W.H., 2016, Spatial Impulse Waves: wave height decay experiments at laboratory scale. *Landslides*, doi:10.1007/s10346-016-0719-1.

Fanetti, D., Anselmetti, F.S., Chapron, E., Sturm, M., and Vezzoli, L., 2008, Megaturbidite deposits in the Holocene basin fill of Lake Como (Southern Alps, Italy): *Palaeogeography Palaeoclimatology Palaeoecology*, v. 259, p. 323-340.

Gavin, D.G., 2001, Estimation of inbuilt age in radiocarbon ages of soil charcoal for fire history studies: *Radiocarbon*, v. 43, no. 1, p. 27-44.

Girardclos, S., Schmidt, O.T., Sturm, M., Ariztegui, D., Pugin, A., and Anselmetti, F.S., 2007, The 1996 AD delta collapse and large turbidite in Lake Brienz: *Marine Geology*, v. 241, p. 137-154.

Goldfinger, C. Nelson, C.H., Morey, A., Johnson, J.E., and Gutierrez-Pastor, J., 2012, Turbidite event history: Methods and implications for Holocene paleoseismicity of the Cascadia Subduction Zone: *USGS Professional Paper*, U.S. Geological Survey, Reston, 178 p.

Goldfinger, C., Hans Nelson, C., and Johnson, J.E., 2003, Holocene earthquake records from the Cascadia Subduction Zone and northern San Andreas Fault based on precise dating of offshore turbidites: *Annual Review of Earth and Planetary Science*, v. 31, p. 555-577.

Gomberg, J., and Sherrod, B., and 2014, Crustal earthquake triggering by pre-historic great earthquakes on subduction zone thrusts: *Journal of Geophysical Research Solid Earth*, v. 119, no. 2, p. 1235-1250.

Gopal, N.O., Narasimhulu, K.V., and Rao Lakshmana, J., 2004, Optical absorption, EPR, infrared and Raman spectral studies of clinocllore mineral: *Journal of Physics and Chemistry of Solids*, v. 65, p. 1887-1893.

Hallet, D.J., Hills, L.V., and Clague, J.J., 1997, New accelerator mass spectrometry radiocarbon ages for the Mazama tephra layer from Kootenay National Park, British Columbia, Canada: *Canadian Journal of Earth Science*, v. 34, p. 1202-1209.

Hancox, G.T., Cox, S.C., Turnbull, I.M., and Crozier, M.J., 2003, Reconnaissance studies of landslides and other ground damage caused by the MW7.2 Fiordland earthquake of 22 August 2003: *Institute of Geological & Nuclear Sciences science report 2003/30*, 32 p.

Haugerud, R., 2002, Lidar evidence for Holocene surface rupture on the Little River fault near Port Angeles, Washington [abstract]: *Seismological Research Letters*, 249 p.

Haughton, P., Davis, C., McCaffrey, W. and Barker, S., 2009, Hybrid sediment gravity flow deposits – classification, origin and significance: *Marine and Petroleum Geology*, v. 26, p. 1900-1918.

Heller, V., Hager W.H., and Minor, E-H., 2009, Landslide generated impulse waves in reservoirs: basics and computation: In: Minor H-E (ed) VAW-Mitteilung 211. ETH Zurich, Zurich.

Heller, V., and Spinneken, J., 2015, On the effect of the water body geometry on landslide tsunamis: physical insight from laboratory tests and 2D to 3D wave parameter transformation: *Coastal Engineering*, v. 104, p. 113-134.

Henderson, J.A., Peter, D.H., Leshner, R.D., and Shaw, D.C., 1989, Forested plant associations of the Olympic National Forest: U.S. Department of Agriculture, Forest Service: Pacific Northwest Region, publication R6-ECOL-TP-001-88, 501 p.

Heusser, C.J., 1973, Environmental sequence following the Fraser advance of the Juan de Fuca lobe, Washington: *Quaternary Research*, v. 3, no. 2, p. 284-306.

Highland, L.M., 2003, An Account of Preliminary Landslide Damage and Losses Resulting from the February 28, 2001 Nisqually, Washington, Earthquake: U.S. Geological Survey Open File Report 03-211. <http://pubs.usgs.gov/of/2003/ofr-03-211/>.

Hilbe, M., and Anselmetti, F.S., 2014, Signatures of slope failures and river-delta collapses in a perialpine lake (Lake Lucerne, Switzerland): *Sedimentology*, v. 61, p. 1883-1907.

Hiller, Michael. Lake Crescent from Mount Storm King (Olympic NP), 2008, <http://cs.stanford.edu/people/hillerm/Pictures/PanoramaPics/indexVacation2008.html>. (accessed September 2016).

Howarth, J.D., Fitzsimons, S.J., Norris, R.J., and Jacobsen, G.E., 2012, Lake sediments record cycles of sediment flux drive by large earthquakes on the Alpine fault, New Zealand: *Geology*, v. 40, no. 12, p. 1091-1094.

Ichinose, G.A., Anderson, J.G., Satake, K., Schweickert R.A., and Lahren, M.M., 2000, The potential hazard from tsunami and seiche waves generated by large earthquakes within Lake Tahoe, California-Nevada: *Geophysical Research Letters*, v. 27, p. 1207-1210.

Inouchi, Y., Kinugasa, Y., Kumon, F., Nakano, S., Yasumatsu, S., and Shiki, T., 1996, Turbidites as records of intense palaeoearthquakes in Lake Biwa, Japan: *Sedimentary Geology*, v. 104, no. 1-4, 117-125.

Iverson, R.M., George, D.L., Allstadt, K., Reid, M.E., Collins, B.D., Vallance, J.W., Schilling, S.P., Godt, J.W., Cannon, C.M., Magirl, C.S., Baum, R.L., Coe, J.A., Schulz,

W.H., and Bower, J.B., 2015, Landslide mobility and hazards: implications of the 2014 Oso disaster: *Earth and Planetary Science Letters*, v. 412, p. 197-208.

Jensen, F.B., Kuperman, W.A., Michael, M.B., and Schmidt, H., 2001, *Computational Ocean Acoustics: Second Edition*, Springer, New York, 794 p.

Johnson, S.Y., Potter, C.J., and Armentrout, J.M., 1994, Origin and evolution of the Seattle fault and Seattle basin Washington: *Geology*, v. 22, p. 71-74, 1 insert.

Jørstad, F. A., 1968, Waves generated by landslides in Norwegian fjords and lakes: *Norwegian Geotechnical Institute Publication*, v. 79, p. 13-32.

Kanamori, H., 1995, The Kobe (Hyogo-ken Nanbu) earthquake of January 16, 1995: *Seismological Research Letters*, v. 66, p. 6-10.

Karlin, R.E. and Abella, S.E.B., 1992, Paleoearthquakes in the Puget Sound region recorded in sediments from Lake Washington, U.S.A.: *Science*, v. 258, p. 1617-1620.

Kelsey, H.M, Nelson, A.R., and Hemphill-Haley, E., 2005, Tsunami history of an Oregon coastal lake reveals a 4600 yr record of great earthquakes on the Cascadia subduction zone: *Geological Society of America Bulletin*, v. 117, p. 1009-1032.

Kelts, K., Briegel, U., Ghilardi, K., and Hsu, K.J., 1986, The limnogeology-ETH coring system: *Schweiz. Z. Hydrol.*, v. 48, p. 104-115.

Kremer, K., Hilbe, M., Simpson, G., Decrouy, L., Wildi, W., and Girardclos, S., 2015, Reconstructing 4000 years of mass movement and tsunami history in a deep peri-alpine lake (Lake Geneva, France-Switzerland): *Sedimentology*, v. 62, p. 1305-1327.

Larsen, I.J., Montgomery, D.R., and Korup, O., 2010, Landslide erosion controlled by hillslope material: *Nature Geoscience*, v. 3, p. 247-251.

Lidke, D.J., compiler., 2003, Fault number 557, Unnamed fault along Barnes Creek, in *Quaternary fault and fold database of the United States: U.S. Geological Survey*, <http://earthquakes.usgs.gov/hazards/qfaults>. (accessed July 2016).

Ludwin, R.S., Dennis, R., Carver, D., McMillan, A.D., Losey, R., Clague, J., Jonientz-Trisler, C., Bowechop, J., Wray, J., and James, K., 2005, Dating the 1700 Cascadia earthquake: Great coastal earthquakes in native stories: *Seismological Research Letters*, v. 76, p. 140-148.

Ludwin, R.S., Smits, G.J., Carver, D., James, K., Jonientz-Trisler, C., McMillan, A., Losey, R., Dennis, R., Rasmussen, J., and De Los Angeles, A., 2007, *Folklore and earthquakes:*

Native American oral traditions from Cascadia compared with written traditions from Japan: Geological Society, London, Special Publications, v. 273, p. 67-94.

Mazzotti, S., Dragert, H., Hyndman, R.D., Miller, M.M., and Henton, J.A., 2002, GPS deformation in a region of high crustal seismicity: N. Cascadia forearc: *Earth and Planetary Science Letters*, v. 198, no. 1, p. 41-48.

McCaffrey, R., 1994, Global variability in subduction thrust zone- forearc systems: *Pure and Applied Geophysics*, v. 142, no. 1, p. 173-224.

McCaffrey, R., Qamar, A.I., King, R.W., Wells, R., Khazaradze, G., Williams, C.A., Stevens, C.W., Vollick, J.J., and Zwick, P.C., 2007, Fault locking, block rotation and crustal deformation in the Pacific Northwest: *Geophysical Journal International*, v. 169, no. 3, p. 1315-1340.

McCalpin, J., 1996, *Paleoseismology*: San Diego, Academic Press, 583 p.

McHugh, C.M., Seeber, L., Braudy, N., Cormier, M.-H., Davis, M.B., Diebold, J.B., Dieudonne, N., Douilly, R., Gulick, S.P.S., Hornbach, M.J., Johnson, H.E., III, Ryan Mishkin, K., Sorlien, C.C., Steckler, M.S., Smithe, S.J., and Templeton, J., 2011, Offshore sedimentary effects of the 12 January 2010 Haiti earthquake: *Geology*, v. 39, p. 723-726.

Miller, D.J., 1960, The Alaska earthquake of July 10, 1958: Giant wave in Lituya Bay: *Bulletin of the Seismological Society of America*, v. 50, no. 2, p. 253-266.

Moernaut, J., Van Daele, M.V., Heirman, K., Fontijn, K., Strasser, M., Pino, M., Urrutia, R., and De Batist, M., 2014, Lacustrine turbidites as a tool for quantitative earthquake reconstruction: New evidence for a variable rupture mode in south central Chile: *Journal of Geophysical Research Solid Earth*, v. 119, p. 1607-1633.

Moran, P.W., Cox, S.E., Embrey, S.S., Huffman, R.L., Olsen, T.D., and Fradkin, S.C., 2013, Sources and sinks of nitrogen and phosphorus in a deep, oligotrophic lake, Lake Crescent, Olympic National Park, Washington: U.S. Geological Survey Report 5107, 56 p.

Mulder, T. and Alexander, J., 2001, The physical character of subaqueous sedimentary density flows and their deposits: *Sedimentology*, v. 48, p. 269-299.

Mulder, T., Zaragosi, S., Razin, P., Grelaud, C., Lanfumey, V., and Bavoil, F., 2009, A new conceptual model for the deposition process of homogenite: Application to a cretaceous megaturbidite of the western Pyrenees (Basque region, SW France): *Sedimentary Geology*, v. 222, no. 3-4, p. 263-273.

Nakajima, T. and Kanai, Y., 2000, Sedimentary features of seismoturbidites triggered by the 1983 and older historical earthquakes in the eastern margin of the Japan Sea: *Sedimentary Geology*, v. 135, p. 1-19.

National Park Service., 2016, Olympic National Park Mountains: National Park Service: <https://www.nps.gov/olym/learn/nature/mountains.htm> (accessed June 2016).

National Park Service., 2016, Visiting Lake Crescent: National Park Service: <http://www.nps.gov/olym/planyourvisit/visiting-lake-crescent.htm> (accessed June 2016).

Nelson, A.R., Personius, S.F., Buck, J., Bradley, L.-A., Wells, R.E., and Schermer, E.R., 2007, Field and Laboratory Data from an Earthquake History Study of Scarps of the Lake Creek-Boundary Creek Fault, Between the Elwha River and Siebert Creek, Clallam County, Washington: U.S. Geological Survey Scientific Investigations Map 2961, 2 sheets.

NVE (Norwegian Water Resources and Energy Directorate), 2016, Avalanche Online: NVE: <https://www.nve.no/flaum-og-skred/skrednett/> (accessed September 2016).

Olsson, I., 1986, Radiometric methods, In: Berglund, B. (ed.), Handbook of Holocene Paleocology and Palaeohydrology: John Wiley & Sons, Chichester, p. 273-312.

Pierce, B.E., 1984, The trouts of Lake Crescent, Washington [M.S. Thesis]: Colorado State University, 252 p.

Polenz, M., Wegmann, K.W., and Schasse, H.W., 2004, Geologic map of the Elwha and Angeles Point 7.5 minute quadrangles, Clallam County, Washington: Washington Division of Geology and Earth Resources Open File Report, scale 1:24,000 (Clallam County, Washington), 1 Sheet.

Pollen, A.F., 2016, The Sedimentary Record of Past Earthquakes Identified in Holocene Sediments of Lake Crescent, Washington [M.S. Thesis]: North Carolina State University, 79 p.

Pringle, P., Wegmann, K., Pontbriand, D., and Walker, W.W., 2010, Some recent discoveries pertaining to subfossil forests in the Pacific Northwest—Examples from Lake Crescent and Lower Dry Beds Lakes, Olympic Mountains, Washington: Northwest Scientific Association, Annual Meeting, v. 82, p. 77-78.

PRISM Climate Group., 2012, United States average monthly and annual precipitation, 1981–2010. Oregon State University, Corvallis, OR <http://prism.oregonstate.edu> (accessed June 2016).

Puget Sound LiDAR Consortium., 2015, Northwestern Olympic Peninsula, WA: Terrapoint. Seattle, WA. <http://pugetsoundlidar.ess.washington.edu/index.htm> (accessed June 2016).

Reimer, P.J., Bard, E., Bayliss, A., Beck, J.W., Blackwell, P.G., Bronk, Ramsey C., Buck, C.E., Cheng, H., Edwards, R.L., Friedrich, M., Grootes, P.M., Guilderson, T.P., Hafliadason, H., Hajdas, I., Hatté, C., Heaton, T.J., Hoffmann, D.L., Hogg, A.G., Hughen, K.A., Kaiser, K.F., Kromer, B., Manning, S.W., Niu, M., Reimer, R.W., Richards, D.A., Scott, E.M.,

Southon, J.R., Staff, R.A., Turney, C.S.M., and van der Plicht, J., 2013, IntCal13 and Marine13 radiocarbon age calibration curves 0–50,000 years cal BP: *Radiocarbon*, v. 55, no. 4, p. 1869–1887.

Roberts, N.J., McKillop, R.J., Lawrence, M.S., Psutka, J.F., Clague, J.J., Brideau, M., and Ward, B.C., 2013, Impacts of the 2007 Landslide-Generated Tsunami in Chehalis Lake, Canada: *Landslide Science and Practice*, v. 6, p. 133-140.

Rogers, A.M., Walsh, T.J., Kockelman, W.J., and Priest, G.R., 1996, Earthquake hazards in the Pacific Northwest- An overview, in Rogers, A.M., Walsh, T.J., Kockelman, W.J., and Priest, G.R., eds., *Assessing earthquake hazards and reducing risk in the Pacific Northwest: U.S. Geological Survey Professional Paper 1560*, 67 p.

Rouse, H., 1946, *Elementary Mechanics of Fluids*: Wiley, New York, 172 p.

Sassa, K., and Canuti, P. (eds), 2009, *Landslides-Disaster Risk Edition*. Berlin Heidelberg, Germany: Springer, 648 p.

Satake, K., Shimozaki, K., Tsuji, Y., and Ueda, K., 1996, Time and size of a giant earthquake in Cascadia inferred from Japanese tsunami records of January 1700: *Nature*, v. 379, p. 246-249.

Schasse, H.W., 2003, Geologic map of the Washington portion of the Port Angeles 1:100,000 quadrangle: Washington Division of Geology and Earth Resources Open File Report 2003-6. http://file.dnr.wa.gov/publications/ger_ofr2003-6_geol_map_portangeles_100k.pdf (accessed May 2016).

Schasse, H.W., and Wegmann, K.W., 2000, Geologic map of the Carlsborg 7.5-minute quadrangle, Clallam County, Washington.

Schasse, H.W., Wegmann, K.W., and Polenz, M., 2004, Geologic map of the Port Angeles and Ediz Hook 7.5-minute quadrangles, Clallam County, Washington: Washington Division of Geology and Earth Resource Open File Report 2004-13, 1 sheet, scale 1:24,000.

Schnellmann, M., Anselmetti, F.S., Giardini, D., and McKenzie, J.A., 2005, Mass movement-induced fold-and-thrust belt structures in unconsolidated sediments in Lake Lucerne (Switzerland): *Sedimentology*, v. 52, no. 2, p. 271-289.

Schnellmann, M., Anselmetti, F.S., Giardini, D., and McKenzie, J.A., 2006, 15,000 years of mass-movement history in Lake Lucerne: Implications for seismic and tsunami hazards: *Eclogae Geologicae Helvetiae*, v. 99, p. 409-428.

Schnellmann, M., Anselmetti, F.S., Giardini, D., McKenzie, J.A., and Ward, S.N., 2002, Prehistoric earthquake history revealed by lacustrine slump deposits: *Geology*, v. 30, no. 12, p. 1131-1134.

- Shennan, I., Long, A.J., Rutherford, M.M., Green, F.M., Innes, J.B., Lloyd, J.M., Yong, Z., and Walker, K.J., 1996, Tidal marsh stratigraphy, sea-level change and large earthquakes, I: A 5000 year record in Washington, USA: *Quaternary Science Reviews*, v. 15, p. 1032-1059.
- Siegenthaler, C., Finger, W., Kelts, K., and Wang, S., 1987, Earthquake and seiche deposits in Lake Lucerne, Switzerland: *Eclogae Geologicae Helvetiae*, v. 80, p. 241-260.
- Smoot, J.P., Litwin, R.J., Bischoff, J.L., and Lund, S.J., 2000, Sedimentary record of the 1872 earthquake and “Tsunami” at Owens Lake, southeast California: *Sedimentary Geology*, v. 135, p. 241-254.
- Strasser, M., Monecke, K., Schnellmann, M., and Anselmetti, F.S., 2013, Lake sediments as natural seismographs: A compiled record of Late Quaternary earthquakes in Central Switzerland and its implication for Alpine deformation: *Sedimentology*, v. 60, p. 319-341.
- Stuiver, M., and Reimer, P. J., 1986, A computer program for radiocarbon age calibration: *Radiocarbon*, v. 28, p. 1022-1030.
- Tabor, R.W., 1975, *Guide to the geology of Olympic National Park*: Seattle, University of Washington, 144 p.
- Tabor, R.W. and Cady, W.M., 1978a, The structure of the Olympic Mountains, Washington – Analysis of a subduction zone: U.S. Geological Survey Professional Paper 1033, 38 p.
- Tabor, R.W. and Cady, W.M., 1978b, Geologic Map of the Olympic Peninsula: U.S. Geological Survey Miscellaneous Investigations Map I-994, 2 sheets, scale 1:125,000.
- Talling, P.J., 2014, On the triggers, resulting flow types and frequencies of subaqueous sediment density flows in different settings: *Marine Geology*, v. 352, p. 155-182.
- Taylor, Jeff. *Lake Crescent*, 2008, https://en.wikipedia.org/wiki/Lake_Crescent#/media/File:Lake_Crescent_from_Pyramid_Peak.JPG (accessed September 2016).
- U.S. Geological Survey, 2001, Clallam County: Mount Muller, Lake Crescent, Lake Sutherland <http://gis.ess.washington.edu/data/raster/tenmeter/byquad/index.html> (accessed June 2016).
- U.S. Geological Survey, 2009, Shakemap Scenario: usLakeCreek6.8_se: Earthquake Hazards Program: http://earthquake.usgs.gov/earthquakes/shakemap/global/shake/LakeCreek6.8_se/ (accessed July 2016).
- U.S. Geological Survey, 2011, Shakemap Scenario: usSeattleM7.2_se: Earthquake Hazards Program: http://earthquake.usgs.gov/earthquakes/shakemap/global/shake/SeattleM7.2_se/ (accessed July 2016).

U.S. Geological Survey, 2016, Earthquake Hazards Program: Washington Earthquake History: <http://earthquake.usgs.gov/earthquakes/states/washington/history.php> (accessed June 2016).

U.S. Geological Survey, 2016, Quaternary Fault and Fold Database of the United States: Holocene to Latest Pleistocene: <http://earthquake.usgs.gov/hazards/qfaults/kml.php> (accessed October 2016).

U.S. Geological Survey, 2016, Shakemap Scenario: uscasc9.0_expanded_peak_se: Earthquake Hazards Program: http://earthquake.usgs.gov/earthquakes/shakemap/global/shake/casc9.0_expanded_peak_se/ (accessed July 2016).

Van Daele, M., Moernaut, J., Doom, L., Boes, E., Fontijn, K., Heirman, K., Vandoorne, W., Hebbeln, D., Pino, M., and Urrutia, R., 2015, A comparison of the sedimentary records of the 1960 and 2010 great Chilean earthquakes in 17 lakes: Implications for quantitative lacustrine palaeoseismology: *Sedimentology*, v. 62, p. 1466-1496.

WA State DNR., 2010, Geology GIS Data and Databases: Surface Geology 1:100,000 scale. <http://www.dnr.wa.gov/programs-and-services/geology/publications-and-data/gis-data-and-databases> (accessed June 2016).

WA State DNR, 2012, Earthquakes and Faults: Modeling a Magnitude 6.8 Earthquake on the Lake Creek-Boundary Creek Fault Zone in Clallam County: http://file.dnr.wa.gov/publications/ger_seismic_scenario_lake_creek.pdf (assessed October 2016).

WA State DNR., 2016, Geology and Earth Resources. <http://www.dnr.wa.gov/geology#geologic-hazards> (accessed October 2016).

Wells, R.E., and McCaffrey, R., 2013, Steady rotation of the Cascade arc: *Geology*, v. 41, no. 9, p. 1027-1030.

Wells, R.E., Weaver, C.S., and Blakely, R.J., 1998, Fore-arc migration in Cascadia and its neotectonic significance: *Geology*, v. 26, no. 8, p. 759-762.

Willett, S.D., and Brandon, M.T., 2002, On steady states in mountain belts: *Geology*, v. 30, p. 75-178.

Yamaguchi, D.K., Atwater, B.F., Bunker, D.E., Benson, B.E., and Reid, M., 1997, Tree-ring dating the 1700 Cascadia earthquake: *Nature*, v. 389, p. 922-923.

APPENDICES

Appendix A. Photographs of radiocarbon dated organic samples extracted from sediment cores.

2C-1K-5 interval: 44.5-45.5



Wood fragment (Pollen, 2016)

3C-1K-1 interval: 70-75 cm



Woody stick and leaf fragments

8A-1K-4 interval: 92-94 cm



Wood and bark fragments (Pollen, 2016)

9A-1K-2 interval: 41-50 cm



Twigs and woody fragments

9A-1K-2 interval: 98-100 cm



Woody fragments

Appendix B. MATLAB script for Gaussian peakfitting of FTIR spectra.

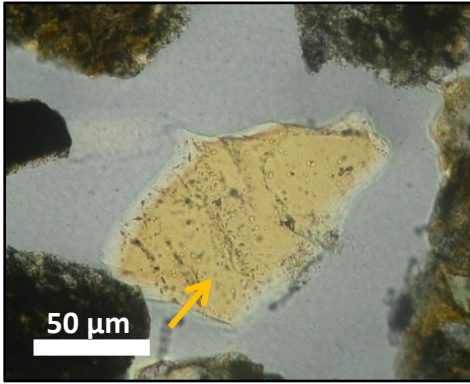
```
%Author: Dr. Christopher Tacker, 2015
%This script reads in a csv. file then performs the background
subtraction to zero the baseline of the whole spectrum. A linear
background correction is then added. The data is passed to the cftool, for
interactive data fitting.
[fileins,FilePathin,Flterind] = uigetfile('green_clay_ABS.csv');
fileToRead=fullfile(FilePathin,fileins);
tone = readtable(fileToRead);
tone.Properties.VariableNames{1} = 'waveno';
tone.Properties.VariableNames{2} = 'abs';
%Begin on the carbonate data reduction.
[longpt,shortpart,exter]= fileparts(fileToRead);
%Find the minimum for the array. Set to zero.
findmin=table2array(tone);
CO3min=min(min(findmin));
tone.abs=tone.abs-CO3min;
%Plot fit with data.
%Isolate the section of interest by clicking upper and lower bounds.
figure('Name',shortpart);
plot(tone.waveno,tone.abs,'*');
xlabel ('wavenumber');
ylabel ('absorbance');
title ('Left click on limits to region of interest.');
```

```
[x,y] = ginput(2);
close (shortpart);
bkgspec1=tone (tone.waveno>=x(1),:);
bkgspec2=bkgspec1(bkgspec1.waveno<=x(2),:);
%Pick the endpoints for a linear background correction.
figure('Name',shortpart);
plot(bkgspec2.waveno,bkgspec2.abs,'*');
xlabel ('wavenumber');
ylabel ('absorbance');
title ('Left click on endpoints for linear background.');
```

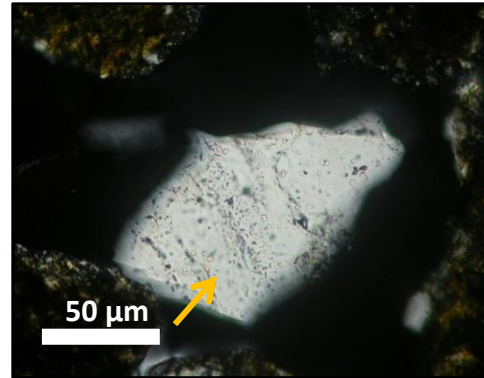
```
[x,y] = ginput(2);
close (shortpart);
%Equation for a straight line.
bkgslope=(y(2)-y(1))/(x(2)-x(1));
bkgintercept=y(1)-(bkgslope*x(1));
%Subtract the linear background.
bkgspec2.abs=bkgspec2.abs-(bkgspec2.waveno*bkgslope+bkgintercept);
figure('Name',shortpart);
plot(bkgspec2.waveno,bkgspec2.abs,'*');
xlabel ('wavenumber');
ylabel ('absorbance');
title ('Press any key when inspection is finished.');
```

```
pause;
close (shortpart);
%Fit model to data.
pause off;
cftool (bkgspec2.waveno,bkgspec2.abs);
```

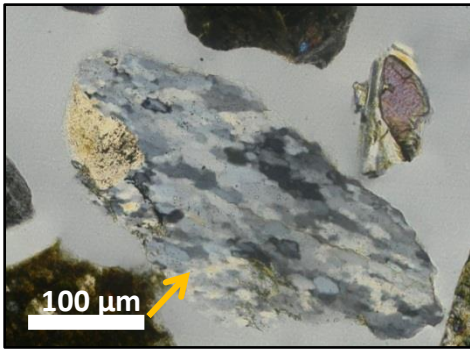
Appendix C. Photographs of representative sand grain types of the petrologic study in plane polarized light (PPL) and cross polarized light (XPL). The sand grains are denoted by the orange arrow.



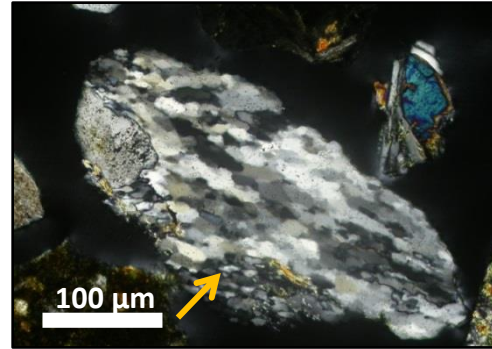
Monocrystalline quartz (PPL)



Monocrystalline quartz (XPL)



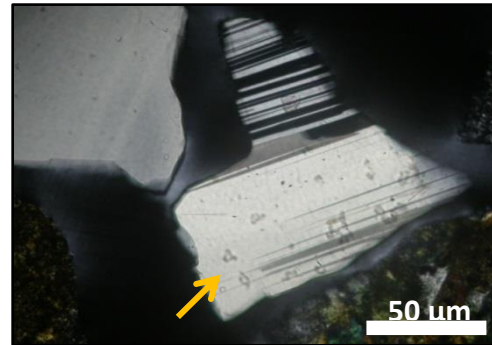
Polycrystalline quartz (PPL)



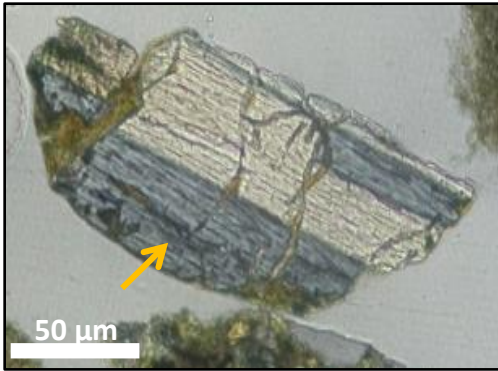
Polycrystalline quartz (XPL)



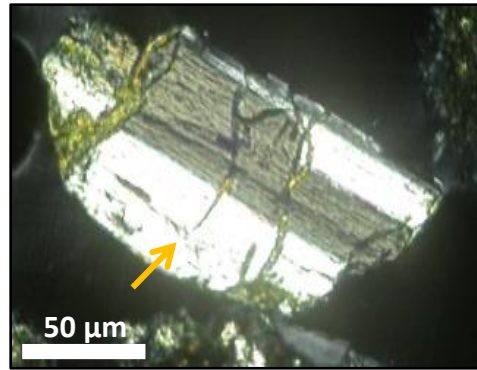
Plagioclase feldspar (PPL)



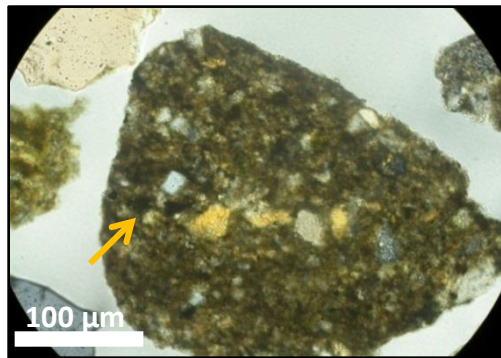
Plagioclase feldspar (XPL)



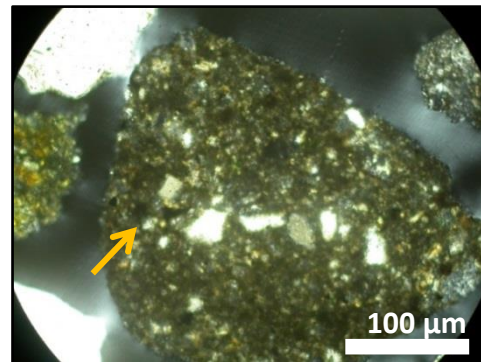
Potassium feldspar (PPL)



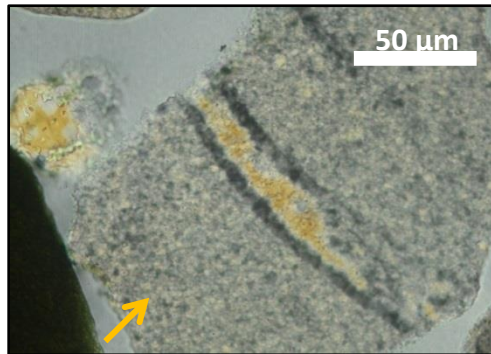
Potassium feldspar (XPL)



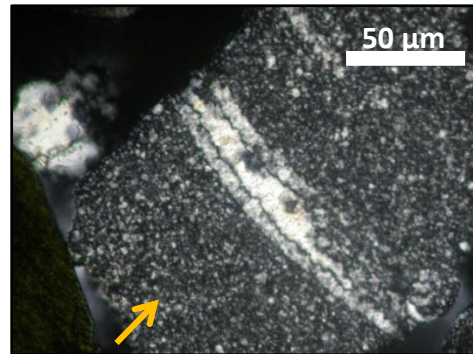
Sedimentary fragment (PPL)



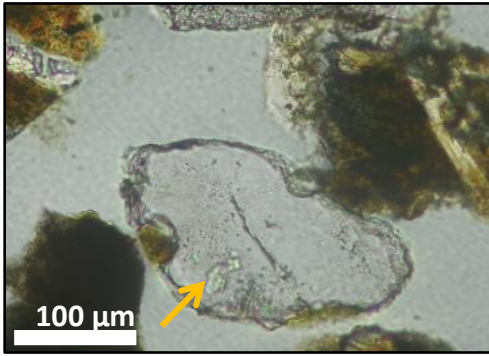
Sedimentary fragment (XPL)



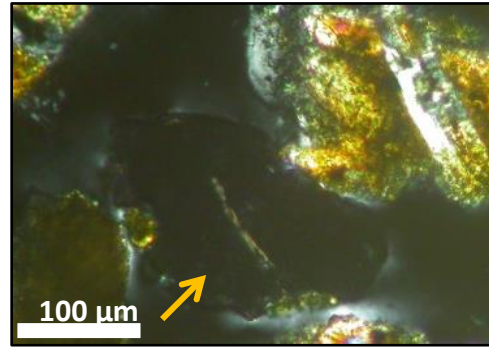
Chert (PPL)



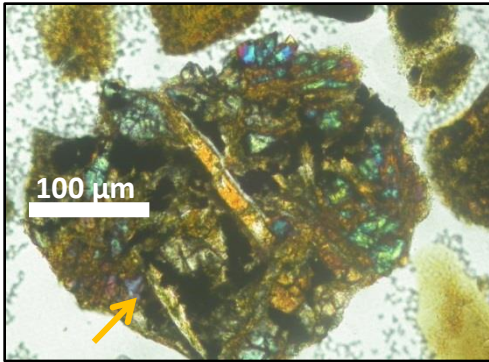
Chert (XPL)



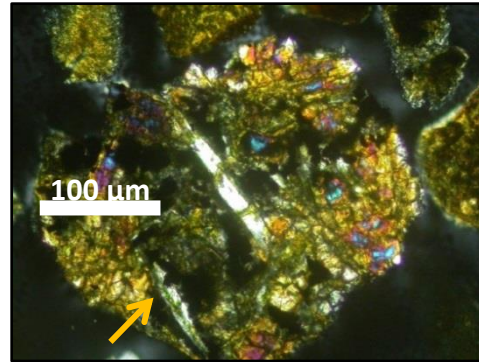
Volcanic glass (PPL)



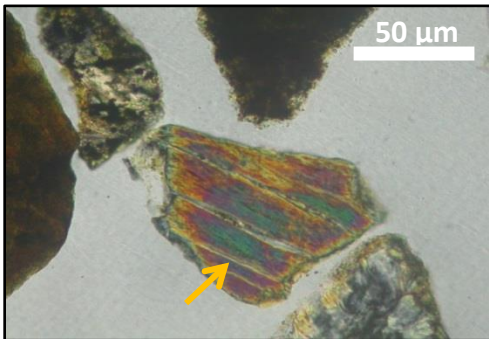
Volcanic glass (XPL)



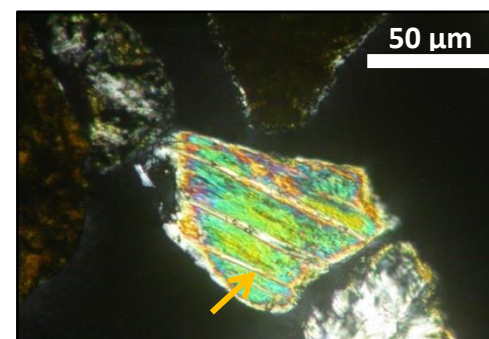
Volcanic fragment (PPL)



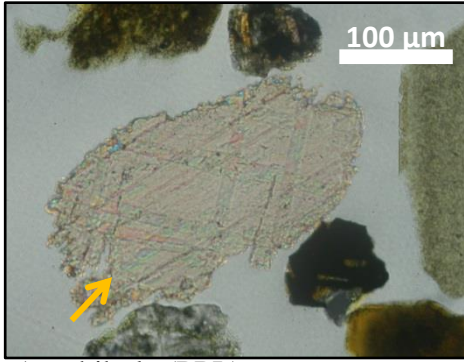
Volcanic fragment (XPL)



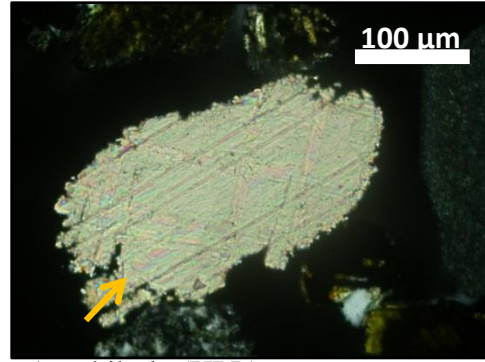
Pyroxene (PPL)



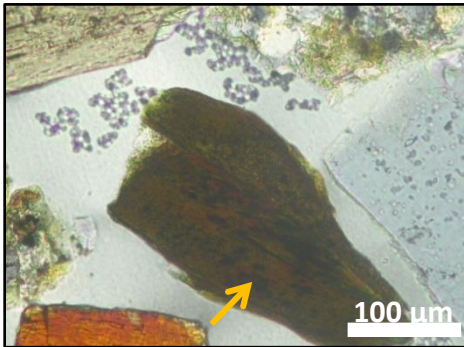
Pyroxene (XPL)



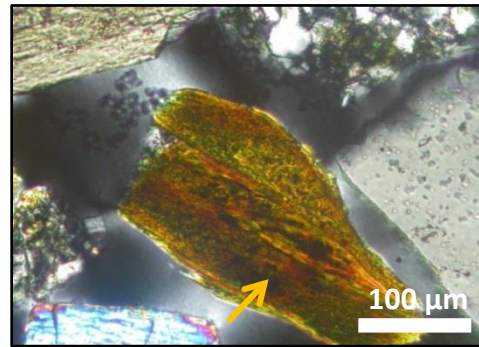
Amphibole (PPL)



Amphibole (XPL)



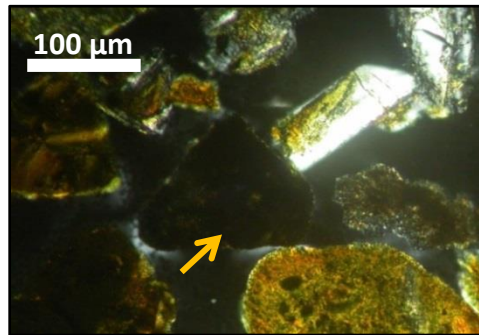
Mica (PPL)



Mica (XPL)



Opaque mineral (PPL)



Opaque mineral (XPL)

Appendix D. MATLAB script for interpolation of the thickness of the EL1-A layer between the manually digitized points.

```
top=load('line11_IMB_ASCII.reflector1.xyz'); %megaturbidite top reflector
bot=load('line11_IMB_ASCII.reflector3.xyz'); %megaturbidite bottom
reflector

[LAT,LON]=utm211(top(:,1),top(:,2),10); %generates LAT, LON of reflector 1
(top of megaturbidite)
[LAT1,LON1]=utm211(bot(:,1),bot(:,2),10);

newx=horzcat(LAT,LON,top(:,3),top(:,4)); %horizontally concatenates
LAT,LON,DEPTH,THICKNESS matrices
newy=horzcat(LAT1,LON1,bot(:,3),bot(:,4));

[LATp,LONp]=interp(LAT1,LON1,0.0001); %densify LAT LON sampling in lines

d=distance(LATp(1),LONp(1),LATp,LONp,referenceEllipsoid('wgs84','m'));
%finds distance between the first LATp,LONp and every point in the
matrices LATp and LONp

dist1=distance(LAT(1),LON(1),LAT,LON,referenceEllipsoid('wgs84','m'));
dist2=distance(LAT1(1),LON1(1),LAT1,LON1,referenceEllipsoid('wgs84','m'));

pred1=interp1(dist1,top(:,3),d); %x(:,3)=depth of reflector 1
pred2=interp1(dist2,bot(:,3),d); %y(:,3)=depth of reflector 3

a=smooth(pred1,11) %applies 11 point moving average to smooth the data
b=smooth(pred2,11) %applies 11 point moving average to smooth the data

thickness=b-a %difference in depths of reflectors
figure; plot(d,b-a) %plots thickness vs distance
xlabel('distance (m)')
ylabel('thickness of megaturbidite (m)')

newdata=horzcat(LATp,LONp,thickness) %matrix of new data

filename='line11.csv'; % CHANGE THIS FILENAME FOR EACH LINE
dlmwrite(filename,newdata,'Precision','%10g')
```

Appendix E. Volume and mass calculations of megaturbidite EL1-A. Calculations were made assuming 40% sediment porosity.

Basin Name	Wet volume (m ³)	Density (g/cm ³)	Conversion	Wet mass (T)
North	1.88 x 10 ⁶ *	2.0 *	$\frac{100^3 \text{ cm}^3}{\text{m}^3} * \frac{1 \text{ kg}}{1000 \text{ g}} * \frac{1 \text{ T}}{1000 \text{ kg}} =$	3.76 x 10 ⁶
South	2.91 x 10 ⁶ *	2.0 *	$\frac{100^3 \text{ cm}^3}{\text{m}^3} * \frac{1 \text{ kg}}{1000 \text{ g}} * \frac{1 \text{ T}}{1000 \text{ kg}} =$	5.82 x 10 ⁶

Basin Name	Wet volume (m ³)	Proportion of dry material	Dry volume (m ³)
North	1.88 x 10 ⁶ *	0.6 (60%) =	1.13 x 10 ⁶
South	2.91 x 10 ⁶ *	0.6 (60%) =	1.75 x 10 ⁶

Basin Name	Wet mass (m ³)	Proportion of dry material	Dry mass (T)
North	3.76 x 10 ⁶ *	0.6 (60%) =	2.26 x 10 ⁶
South	5.82 x 10 ⁶ *	0.6 (60%) =	3.49 x 10 ⁶

Appendix F. Volume error calculations of megaturbidite EL1-A. Refer to figure 27b. Calculations were made assuming 40% sediment porosity.

General equation = number of pixels within error range in raster * raster cell resolution * median value of error range

	Amount of pixels *	Cell resolution (m ²) *	Median error value (m)	Wet sediment volume error
Dark blue pixels	27107	6.138 x 6.138	0.05	51063 m ³
Light blue pixels	75927	6.138 x 6.138	0.15	429082 m ³
Peach pixels	91671	6.138 x 6.138	0.25	863427 m ³
Red pixels	18328	6.138 x 6.138	0.35	242389 m ³
				Total: 1.58 x 10 ⁶ m ³

$$\text{Wet sediment volume error} = 1.58 \times 10^6 \text{ m}^3$$

$$\text{Dry sediment volume error} = 1.58 \times 10^6 \text{ m}^3 * 0.6 = 0.94 \times 10^6 \text{ m}^3$$

$$\text{Dry sediment mass volume error} = 1.58 \times 10^6 \text{ m}^3 * \frac{2 \text{ g}}{\text{cm}^3} * \frac{100^3 \text{ cm}^3}{\text{m}^3} * \frac{1 \text{ kg}}{1000 \text{ g}} * \frac{1 \text{ T}}{1000 \text{ kg}} = 3.16 \times 10^6 \text{ m}^3 * 0.6 = 1.89 \times 10^6 \text{ T}$$

Appendix G. Calculation of the dry volume of annual normal sedimentation. Assume porosity of 40%.

Average event free sedimentation rate (m/yr)	Area of EL1-A (m ²)	Wet volume of normal sedimentation for EL1-A area (m ³)	Proportion of dry material	Dry volume of normal sedimentation for EL1-A area (m ³)
0.00079 *	9.84 x10 ⁶ =	7773 *	0.6 =	4664

$$\frac{2.87 \times 10^6 \text{ m}^3 \text{ (dry volume of EL1A)}}{1 \text{ year}} = \frac{4664 \text{ m}^3 y}{1 \text{ year}}$$

$$2.87 \times 10^6 \text{ m}^3 = 4664 \text{ m}^3 y$$

y = 615 (number of years of normal sedimentation equal to one event year)

Appendix H. MATLAB script for the bootstrap sampling of the power law coefficients given for Figure 38.

```

%% plot the data
filename='btstrp.csv';
M=csvread(filename);
x=M(:,1);
y=M(:,2);
%% bootstrap sampling
p2=bootstrp(5000,@polyfit,log10(x),log10(y),1); %5000 bootstrap
coefficients (with replacement)
D=(p2(:,1))
Dstd=(p2(:,1))
a=(p2(:,2))
astd=(p2(:,2))
Dmean=mean(D) %new coefficient where  $y = a \cdot x^D$ 
amean=mean(a)
amean=10^amean
Rmin=10.^a.*6471000.^D; %minimum slide volume (10% error)
Rmax=10.^a.*7909000.^D; %maximum slide volume (10% error)
Rminmean=mean(Rmin) %mean run up value based on min slide volume
Rmaxmean=mean(Rmax) %mean run up value based on max slide volume
figure; %hist of 5000 run up values based on min slide volume
[n,x] = hist(Rmin);
h = bar(x,n);
set(h,'facecolor','none','edgecolor','r')
xlabel('bins')
ylabel('number of samples')
title('histogram of wave run up values based on slide volume')
hold on; %hist of 5000 run up values based on max slide volume
[n,x] = hist(Rmax);
h = bar(x,n);
set(h,'facecolor','none','edgecolor','g')
legend('min','max')
R=cat(1,Rmin,Rmax); %1x1 matrix of possible wave run up values based
on 10000 total bootstrap samples
CI=quantile(R,[0.025,0.975]);
meanR=mean(R);
figure; loglog(x,y,'+k',x,amean*x.^Dmean,'r')

```

Appendix I. MATLAB script for the lognormal probability distribution of earthquake recurrence on the Lake Creek-Boundary Creek fault.

```
%% input the event times below
t=[2859, 4015, 5736, 7097]; % event times
to= 2859 % time since last event
twindow = 50; %Time window to consider moving forward (years)

%% estimate the PDF for the lognormal distribution.
df=length(t)-2; % degrees freedom
s=sqrt(sum((log(diff(t)./mean(diff(t))).^2)/df); % log of std =
skewness factor for lognormal distribution
x=1:1:8000 % time interval range to consider in one year bins
y = lognpdf(x,log(mean(diff(t))),s); % plot the PDF

p = (sum(y(x >= to))-sum(y(x >= to + twindow )))/sum(y(x > to)) %
probability in next twindow
p=p*100
%% plotting stuff
figure; plot(x,y,'k'); % plot the PDF
hold on; plot(to,y(x==to),'or'); ylabel('probability');
xlabel('inter-event times')
title(['Lognormal with mean ' num2str(mean(diff(t))) ' and skewness '
num2str(s) ''])
text(to+0.02*max(x),y(x==to),'time since last event')
```

Appendix J. Magnetic susceptibility and median particle size data for EL1-A in core 2C-1K

Depth in core (cm)	Magnetic Susceptibility (SI)	Depth in core (cm)	Magnetic Susceptibility (SI)	Depth in core (cm)	Magnetic Susceptibility (SI)
97	279	114.5	542	132.5	692
97.5	303	115	567	133	663
98	248	115.5	575	133.5	598
98.5	309	116	594	134	588
99	266	116.5	601	134.5	442
99.5	244	117	606	135	285
100	224	117.5	610	135.5	547
100.5	81	118	568	136	420
101	48	118.5	555	136.5	89
101.5	43	119	524	138	274
102	62	119.5	507	138.5	515
102.5	46	120	533	139	576
103	40	120.5	549	139.5	531
103.5	36	121	550	140	561
104	36	121.5	575	140.5	613
104.5	39	122	572	141	635
105	40	122.5	563	141.5	637
105.5	43	123	562	142	642
106	42	123.5	548	142.5	642
106.5	95	124	528	143	577
107	181	124.5	564	143.5	610
107.5	132	125	575	144	611
108	133	125.5	592	144.5	652
108.5	307	126	598	145	640
109	570	126.5	535	145.5	618
109.5	573	127	461	146	633
110	578	127.5	549	146.5	614
110.5	603	128.5	560	147	609
111	597	129	547	147.5	587
111.5	602	129.5	501	148	547
112	613	130	586	148.5	569
112.5	611	130.5	605	149	620
113	592	131	608	149.5	626
113.5	585	131.5	662	150	611
114	545	132	681	150.5	627

Depth in core (cm)	Magnetic Susceptibility (SI)	Depth in core (cm)	Magnetic Susceptibility (SI)	Depth in core (cm)	Magnetic Susceptibility (SI)
151	618	168.5	598	186	745
151.5	624	169	651	186.5	778
152	652	169.5	668	187	770
152.5	634	170	677	187.5	789
153	586	170.5	651	188	780
153.5	608	171	645	188.5	756
154	607	171.5	647	189	783
154.5	595	172	646	189.5	788
155	599	172.5	651	190	750
155.5	613	173	663	190.5	748
156	610	173.5	659	191	727
156.5	591	174	666	191.5	781
157	618	174.5	663	192	791
157.5	628	175	663	192.5	784
158	595	175.5	660	193	798
158.5	604	176	691	193.5	795
159	605	176.5	645	194	753
159.5	546	177	652	194.5	775
160	569	177.5	685	195	781
160.5	612	178	680	195.5	772
161	619	178.5	654	196	710
161.5	587	179	655	196.5	731
162	594	179.5	618	197	752
162.5	608	180	564	197.5	738
163	608	180.5	669	198	731
163.5	612	181	700	198.5	762
164	605	181.5	690	199	785
164.5	581	182	704	199.5	784
165	614	182.5	677	200	788
165.5	639	183	660	200.5	762
166	642	183.5	696	201	705
166.5	623	184	712	201.5	694
167	635	184.5	724	202	726
167.5	624	185	620	202.5	752
168	621	185.5	707	203	765

Depth in core (cm)	Magnetic Susceptibility (SI)	Depth in core (cm)	Magnetic Susceptibility (SI)	Depth in core (cm)	Magnetic Susceptibility (SI)
203.5	706	222	1504	239.5	1700
204	693	222.5	1454	240	1754
204.5	696	223	1528	240.5	1800
205	695	223.5	1557	241	1877
205.5	709	224	1428	241.5	1540
206	681	224.5	1558	242	1638
206.5	684	225	1549	242.5	1675
207	733	225.5	1459	243	1256
207.5	698	226	1329	243.5	1226
208	684	226.5	1265	244	1472
208.5	708	227	1315	244.5	2444
209	738	227.5	1067	245	2794
209.5	723	228	1343		
210	768	228.5	1282		
210.5	830	229	1493		
211	872	229.5	1543		
211.5	940	230	1529		
212	1015	230.5	1369		
212.5	1055	231	1346		
213	1058	231.5	1287		
213.5	1009	232	1487		
214	1074	232.5	1499		
214.5	1138	233	1509		
215	1164	233.5	1489		
215.5	1189	234	1832		
216	1290	234.5	1602		
216.5	1272	235	1482		
217	1250	235.5	1302		
217.5	1217	236	1360		
218	1210	236.5	1928		
218.5	1250	237	1806		
219	1310	237.5	2008		
219.5	1340	238	2002		
221	1400	238.5	1553		
221.5	1424	239	2007		

Depth in core (cm)	Median particle size (µm)
97	7.115
100	5.443
104	0.992
106	1.22
108	2.032
113	9.04
118	8.3
122	7.406
128	6.872
133	12.92
135	12.88
142	11.45
148	11.88
153	10.9
158	10.34
163	10.41
173	14.06
183	12.43
193	13.64
203	13.07
213	23.74
218	73.95
223	68.4
228	137.5
233	183.2
238	247.1
243	276.4
245	258

Appendix K. Magnetic susceptibility and median particle size data for EL1-A in core 6A-1K

Depth in core (cm)	Magnetic Susceptibility (SI)	Depth in core (cm)	Magnetic Susceptibility (SI)	Depth in core (cm)	Magnetic Susceptibility (SI)
365	278	382.5	291	400	457
365.5	298	383	297	400.5	465
366	369	383.5	274	401	481
366.5	353	384	289	401.5	458
367	383	384.5	302	402	505
367.5	439	385	229	402.5	490
368	401	385.5	355	403	500
368.5	388	386	355	403.5	526
369	620	386.5	254	404	493
369.5	437	387	39	404.5	489
370	260	387.5	170	405	521
370.5	126	388	291	405.5	502
371	258	388.5	431	406	475
371.5	65	389	377	406.5	472
372	52	389.5	324	407	473
372.5	75	390	305	407.5	468
373	107	390.5	320	408	498
373.5	154	391	318	408.5	495
374	212	391.5	340	409	480
374.5	364	392	370	409.5	465
375	405	392.5	441	410	454
375.5	388	393	510	410.5	483
376	419	393.5	480	411	479
376.5	420	394	518	411.5	459
377	409	394.5	525	412	458
377.5	406	395	486	412.5	492
378	387	395.5	451	413	511
378.5	358	396	467	413.5	522
379	328	396.5	481	414	510
379.5	346	397	491	414.5	503
380	377	397.5	472	415	522
380.5	402	398	475	415.5	545
381	433	398.5	477	416	546
381.5	362	399	485	416.5	550
382	293	399.5	457	417	542

Depth in core (cm)	Magnetic Susceptibility (SI)	Depth in core (cm)	Magnetic Susceptibility (SI)	Depth in core (cm)	Magnetic Susceptibility (SI)
417.5	542	435	539	452.5	604
418	569	435.5	545	453	572
418.5	561	436	568	453.5	598
419	566	436.5	585	454	600
419.5	555	437	614	454.5	602
420	547	437.5	628	455	617
420.5	548	438	625	455.5	643
421	539	438.5	609	456	627
421.5	537	439	580	456.5	639
422	532	439.5	565	457	642
422.5	556	440	547	457.5	612
423	558	440.5	537	458	613
423.5	578	441	544	458.5	644
424	578	441.5	541	459	670
424.5	540	442	538	459.5	691
425	552	442.5	561	460	692
425.5	605	443	581	460.5	688
426	589	443.5	591	461	637
426.5	569	444	560	461.5	652
427	543	444.5	547	462	648
427.5	527	445	581	462.5	591
428	534	445.5	578	463	571
428.5	548	446	574	463.5	679
429	559	446.5	584	464	700
429.5	570	447	607	464.5	667
430	562	447.5	564	465	659
430.5	555	448	562	465.5	700
431	502	448.5	574	466	692
431.5	533	449	596	466.5	658
432	559	449.5	584	467	676
432.5	568	450	595	467.5	684
433	572	450.5	583	468	682
433.5	572	451	608	468.5	721
434	555	451.5	612	469	715
434.5	527	452	621	469.5	698

Depth in core (cm)	Magnetic Susceptibility (SI)	Depth in core (cm)	Magnetic Susceptibility (SI)	Depth in core (cm)	Magnetic Susceptibility (SI)
470	719	487.5	789	505	886
470.5	741	488	786	505.5	807
471	730	488.5	780	506	782
471.5	726	489	783	506.5	810
472	751	489.5	703	507	869
472.5	711	490	657	507.5	852
473	708	490.5	607	508	821
473.5	705	491	636	508.5	734
474	704	491.5	671	509	621
474.5	736	492	655	509.5	519
475	729	492.5	634	510	753
475.5	764	493	611	510.5	905
476	753	493.5	631	511	712
476.5	751	494	658	511.5	439
477	741	494.5	629	512	379
477.5	684	495	589	512.5	369
478	693	495.5	646	513	877
478.5	739	496	646	513.5	946
479	739	496.5	620	514	991
479.5	749	497	645	514.5	1043
480	783	497.5	687	515	847
480.5	777	498	658	515.5	385
481	771	498.5	588	516	148
481.5	661	499	725	516.5	107
482	667	499.5	879	517	163
482.5	752	500	775	517.5	243
483	736	500.5	668	518	297
483.5	754	501	678	518.5	307
484	768	501.5	790	519	803
484.5	761	502	960	519.5	1058
485	766	502.5	884	520	542
485.5	815	503	863	520.5	689
486	798	503.5	831	521	797
486.5	775	504	895	521.5	430
487	761	504.5	910	522	834

Depth in core (cm)	Magnetic Susceptibility (SI)
522.5	1545
523	1483
523.5	1068
524	793
524.5	277
525	118
525.5	157
526	219
526.5	477
527	795
527.5	770
528	1309
528.5	1676
529	1380
529.5	554
530	105
530.5	43

Depth in core (cm)	Median particle size (μm)
365	8.278
368	6.43
372	2.119
379	10.87
385	11.6
390	14.66
400	12.53
410	14.01
420	17.72
430	13.45
440	19.59
450	19.97
460	19.5
470	15.81
480	19.7
490	31.27
500	73.3
505	83.93
510	90.76
515	200
520	165.4
525	170.6
530	13.93
531	14.4

Appendix L. Magnetic susceptibility and median particle size data for EL1-A in core 8A-1K

Depth in core (cm)	Magnetic Susceptibility (SI)	Depth in core (cm)	Magnetic Susceptibility (SI)	Depth in core (cm)	Magnetic Susceptibility (SI)
153	534	170.5	584	188	597
153.5	547	171	551	188.5	566
154	554	171.5	557	189	594
154.5	562	172	490	189.5	617
155	544	172.5	474	190	624
155.5	581	173	470	190.5	627
156	559	173.5	491	191	578
156.5	589	174	551	191.5	581
157	601	174.5	573	192	583
157.5	608	175	586	192.5	600
158	596	175.5	580	193	591
158.5	595	176	606	193.5	579
159	619	176.5	616	194	592
159.5	644	177	597	194.5	603
160	640	177.5	576	195	624
160.5	578	178	555	195.5	657
161	627	178.5	565	196	606
161.5	636	179	583	196.5	610
162	598	179.5	586	197	592
162.5	578	180	543	197.5	581
163	606	180.5	613	198	590
163.5	605	181	599	198.5	584
164	598	181.5	601	199	579
164.5	568	182	584	199.5	556
165	516	182.5	562	200	560
165.5	571	183	550	200.5	571
166	596	183.5	573	201	591
166.5	622	184	592	201.5	585
167	601	184.5	599	202	619
167.5	634	185	604	202.5	586
168	627	185.5	600	203	561
168.5	589	186	583	203.5	592
169	595	186.5	597	204	593
169.5	587	187	598	204.5	600
170	592	187.5	633	205	605

Depth in core (cm)	Magnetic Susceptibility (SI)	Depth in core (cm)	Magnetic Susceptibility (SI)	Depth in core (cm)	Magnetic Susceptibility (SI)
205.5	593	223	599	240.5	308
206	609	223.5	584	241	374
206.5	600	224	549	241.5	120
207	635	224.5	550	242	10
207.5	592	225	540	243	2
208	568	225.5	533	243.5	3
208.5	585	226	554	244	11
209	591	226.5	566	244.5	80
209.5	603	227	582	245	554
210	594	227.5	586	245.5	839
210.5	598	228	594	246	849
211	583	228.5	592	246.5	846
211.5	572	229	587	247	787
212	570	229.5	627	247.5	775
212.5	583	230	631	248	791
213	575	230.5	634	248.5	788
213.5	526	231	632	249	753
214	534	231.5	607	249.5	681
214.5	556	232	614	250	641
215	544	232.5	631	250.5	594
215.5	550	233	642	251	787
216	549	233.5	648	251.5	814
216.5	537	234	650	252	839
217	562	234.5	716	252.5	829
217.5	537	235	707	253	840
218	515	235.5	642	253.5	848
218.5	584	236	609	254	857
219	540	236.5	676	254.5	861
219.5	526	237	688	255	865
220	590	237.5	580	255.5	849
220.5	546	238	427	256	853
221	574	238.5	401	256.5	888
221.5	588	239	340	257	890
222	608	239.5	541	257.5	871
222.5	615	240	475	258	862

Depth in core (cm)	Magnetic Susceptibility (SI)	Depth in core (cm)	Magnetic Susceptibility (SI)	Depth in core (cm)	Magnetic Susceptibility (SI)
258.5	877	276.5	1049	294	856
259	866	277	1094	294.5	679
259.5	882	277.5	1212	295	812
260	889	278	1175	295.5	1605
260.5	938	278.5	1143	296	2224
261.5	19	279	1148	296.5	2033
262	23	279.5	1130	297	2404
262.5	36	280	1135	297.5	2340
263	320	280.5	1089	298	2425
263.5	407	281	1098		
264	623	281.5	949		
264.5	811	282	1128		
265	943	282.5	1413		
265.5	926	283	1500		
266	873	283.5	1433		
266.5	815	284	1559		
267	840	284.5	1614		
267.5	899	285	1638		
268	875	285.5	1598		
268.5	831	286	1528		
269	831	286.5	1493		
269.5	845	287	1534		
270	874	287.5	1648		
270.5	846	288	1864		
271	873	288.5	1580		
271.5	877	289	1271		
272	870	289.5	1414		
272.5	913	290	1368		
273	937	290.5	1656		
273.5	994	291	1668		
274	1036	291.5	1252		
274.5	1027	292	1418		
275	976	292.5	1480		
275.5	1020	293	1593		
276	1021	293.5	1303		

Depth in core (cm)	Median particle size (μm)
153	10.6
163	14.43
173	13.94
183	11.09
193	12.2
203	14.05
213	11.28
223	11.79
233	2.75
250	16.59
260	29.6
265	33.5
279	92.63
285	104.2
286	119.1
287	105.7
288	100.9
289	117.6
290	169.3
291	166.7
292	210.7
293	201.2
294	269.3
295	180.1
296	123.2
297	352.7
298	300.3

Appendix M. Magnetic susceptibility data for EL1-A in core 4A-1K

Depth in core (cm)	Magnetic Susceptibility (SI)	Depth in core (cm)	Magnetic Susceptibility (SI)
100	166	117.5	460
100.5	142	118	443
101	170	118.5	456
101.5	149	119	452
102	297	119.5	480
102.5	343	120	586
103	344	120.5	722
103.5	362	121	597
104	354		
104.5	341		
105	343		
105.5	364		
106	355		
106.5	350		
107	326		
107.5	355		
108	370		
108.5	378		
109	387		
109.5	387		
110	382		
110.5	394		
111	403		
111.5	407		
112	409		
112.5	405		
113	401		
113.5	409		
114	436		
114.5	436		
115	443		
115.5	442		
116	446		
116.5	450		
117	466		

Appendix N. Magnetic susceptibility data for EL1-A in core 7C-1K

Depth in core (cm)	Magnetic Susceptibility (SI)	Depth in core (cm)	Magnetic Susceptibility (SI)	Depth in core (cm)	Magnetic Susceptibility (SI)
261	273	278.5	546	296	136
261.5	331	279	550	296.5	284
262	171	279.5	552	297	292
262.5	224	280	552	297.5	375
263	134	280.5	534	298	372
263.5	64	281	545	298.5	361
264	34	281.5	530	299	416
264.5	36	282	481	299.5	525
265	76	282.5	499	300	522
265.5	110	283	541	300.5	524
266	99	283.5	551	301	544
266.5	26	284	552	301.5	563
267	25	284.5	560	302	584
267.5	33	285	554	302.5	551
268	36	285.5	532	303	546
268.5	48	286	550	303.5	556
269	34	286.5	536	304	566
269.5	35	287	508	304.5	435
270	40	287.5	523	305	266
270.5	46	288	527	305.5	432
271	51	288.5	561	306	556
271.5	51	289	529	306.5	574
272	56	289.5	527	307	578
272.5	57	290	521	307.5	582
273	67	290.5	539	308	584
273.5	75	291	544	308.5	564
274	87	291.5	568	309	533
274.5	94	292	543	309.5	403
275	109	292.5	562	310	418
275.5	255	293	561	310.5	453
276	468	293.5	523	311	653
276.5	504	294	178	311.5	636
277	517	294.5	206	312	470
277.5	513	295	185	312.5	364
278	519	295.5	21	313	419

Depth in core (cm)	Magnetic Susceptibility (SI)	Depth in core (cm)	Magnetic Susceptibility (SI)	Depth in core (cm)	Magnetic Susceptibility (SI)
313.5	431	332	474	350	529
314	421	332.5	435	350.5	561
314.5	423	333	458	351	562
315	468	333.5	461	351.5	552
315.5	515	334	426	352	591
316	567	334.5	395	352.5	405
316.5	619	335	386	353	440
317	607	336	377	353.5	654
317.5	594	336.5	384	354	681
318	594	337	399	354.5	672
318.5	606	337.5	399	355	669
319	587	338	389	355.5	665
319.5	555	338.5	405	356	625
320	552	339	387	357	588
320.5	576	339.5	436	357.5	588
321	580	340	424	358	618
321.5	564	340.5	412	358.5	602
322	577	341	423	359	610
322.5	565	341.5	414	363	631
323.5	621	342	415	363.5	541
324	605	342.5	415	364	417
324.5	623	343	413	364.5	428
325.5	591	343.5	430	365	626
326	571	344	412	365.5	580
326.5	524	344.5	428	366	558
327	485	345	414	366.5	546
327.5	467	345.5	401	367	600
328	493	346	431	367.5	578
328.5	542	346.5	462	368	574
329	645	347	462	368.5	632
329.5	557	347.5	433	369	508
330	545	348	492	369.5	487
330.5	565	348.5	507	370	502
331	552	349	513	370.5	529
331.5	526	349.5	525	371	532

Depth in core (cm)	Magnetic Susceptibility (SI)	Depth in core (cm)	Magnetic Susceptibility (SI)
371.5	568	388	575
372	512	388.5	596
372.5	451	388	575
373	455	388.5	596
373.5	494	388	575
374	571	388.5	596
374.5	264	388	575
375	247	388.5	596
375.5	456	388	575
376	554	388.5	596
376.5	484	388	575
377	515	388.5	596
377.5	500	388	575
378	503	388.5	596
378.5	453	388	575
379	442	388.5	596
379.5	454	388	575
380	472	388.5	596
380.5	475	388	575
381	538	388.5	596
381.5	380	388	575
382	409	388.5	596
382.5	521	388	575
383	605		
383.5	613		
384	526		
384.5	478		
385	466		
385.5	468		
386	600		
386.5	638		
387	622		
387.5	582		
388	575		
388.5	596		

Appendix O. Magnetic susceptibility data for EL1-A in core 9A-1K

Depth in core (cm)	Magnetic Susceptibility (SI)	Depth in core (cm)	Magnetic Susceptibility (SI)
22	124	39.5	315
22.5	133		
23	127		
23.5	108		
24	146		
24.5	175		
25	176		
25.5	180		
26	180		
26.5	160		
27	171		
27.5	179		
28	187		
28.5	192		
29	202		
29.5	217		
30	229		
30.5	232		
31	240		
31.5	215		
32	186		
32.5	236		
33	234		
33.5	237		
34	238		
34.5	221		
35	209		
35.5	243		
36	273		
36.5	276		
37	278		
37.5	273		
38	284		
38.5	287		
39	291		

Appendix P. Magnetic susceptibility and median particle size data for EL2 interval 50-77 cm in core 6A-1K (denoted as 6A-1K in Fig. 18)

Depth in core (cm)	Magnetic Susceptibility (SI)	Depth in core (cm)	Magnetic Susceptibility (SI)
50	196	68	147
50.5	221	68.5	192
51	229	69	181
51.5	190	69.5	194
52	173	70	192
52.5	172	70.5	239
53	158	71	230
53.5	141	71.5	128
54	187	72	100
54.5	176	72.5	132
55	148	73	233
55.5	159	73.5	300
56	176	74	331
56.5	175	74.5	333
57	171	75	288
57.5	198	75.5	230
58	204	76	153
58.5	188	76.5	166
59	201	77	321
59.5	229		
60	236		
60.5	234		
61	252		
61.5	263		
62	245		
62.5	253		
63	258		
63.5	264		
64	283		
64.5	285		
65	269		
65.5	250		
66	258		
66.5	278		
67	260		
67.5	134		

Depth in core (cm)	Median particle size (μm)
50	15.74
59	27.98
64	24.05
70	27.28
77	30.59

Appendix Q. Magnetic susceptibility and median particle size data for EL2 interval 200-214 cm in core 6A-1K (denoted as 6A-1K* in Fig. 18)

Depth in core (cm)	Magnetic Susceptibility (SI)
200	224
200.5	197
201	228
201.5	212
202	247
202.5	311
203	274
203.5	270
204	261
204.5	266
205	265
205.5	292
206	237
206.5	267
207	259
207.5	190
208	211
208.5	309
209	372
209.5	389
210	361
210.5	349
211	377
211.5	390
212	400
212.5	433
213	422
213.5	435
214	477

Depth in core (cm)	Median particle size (μm)
200	16.73
203	23.77
207	19.05
211	26.65
214	50.72